# Spin Decoherence of Electrons and Holes in Semiconductor Quantum Dots

Inauguraldissertation

zur

Erlangung der Würde eines Doktors der Philosophie

vorgelegt der

Philosophisch-Naturwissenschaftlichen Fakultät

der Universität Basel

von

Jan Fischer

aus Freiburg i. Br., Deutschland

Basel, 2010

creative commons

**Namensnennung-Keine kommerzielle Nutzung-Keine Bearbeitung 2.5 Schweiz**

---

## Sie dürfen:

das Werk vervielfältigen, verbreiten und öffentlich zugänglich machen

## Zu den folgenden Bedingungen:

**Namensnennung**. Sie müssen den Namen des Autors/Rechteinhabers in der von ihm festgelegten Weise nennen (wodurch aber nicht der Eindruck entstehen darf, Sie oder die Nutzung des Werkes durch Sie würden entlohnt).

**Keine kommerzielle Nutzung**. Dieses Werk darf nicht für kommerzielle Zwecke verwendet werden.

**Keine Bearbeitung**. Dieses Werk darf nicht bearbeitet oder in anderer Weise verändert werden.

- Im Falle einer Verbreitung müssen Sie anderen die Lizenzbedingungen, unter welche dieses Werk fällt, mitteilen. Am Einfachsten ist es, einen Link auf diese Seite einzubinden.
- Jede der vorgenannten Bedingungen kann aufgehoben werden, sofern Sie die Einwilligung des Rechteinhabers dazu erhalten.
- Diese Lizenz lässt die Urheberpersönlichkeitsrechte unberührt.



Quelle: http://creativecommons.org/licenses/by-nc-nd/2.5/ch/ Datum: 3.4.2009

Genehmigt von der Philosophisch-Naturwissenschaftlichen Fakultät auf Antrag von

Prof. Dr. Daniel Loss

Prof. Dr. Herbert Schoeller

Basel, den 22. Juni 2010

Prof. Dr. M. Spiess
Dekan

# Summary

The computer industry has seen an immense development in the last decades. Personal computers have become available for everybody living in industrialized countries with rapidly increasing performance in terms of speed and storage capacities. However, the performance of nowadays' computers is fundamentally limited by the laws of classical physics: a classical bit can only take on either of the two distinct values '0' or '1'. In contrast, a quantum computer could, in principle, make direct use of quantum phenomena, such as state superpositions – a quantum bit can be in both states '0' and '1' simultaneously –, to perform complex computational tasks much faster than any classical computer.

The idea of building computers that work according to the laws of quantum physics has opened various fields of research, one of which is the search for the best physical system to use as a quantum bit (qubit). One important criterion for determining the optimal qubit system is the lifetime of state superpositions. Typically, once initialized, such superpositions are destroyed on remarkably short timescales due to interactions with the environment – a process which is referred to as *decoherence* –, posing the question which physical qubit candidate system might show a high-enough robustness against the influence of the 'outside world' to allow for viable quantum computation.

In this thesis, we will consider three particular realizations of one specific and very promising type of qubit candidate system: an electron (or hole) confined to a quantum dot – a nanoscale structure within a (typically semiconducting) material –, where the spin states '↓' and '↑' of our electron (or hole) encode the logical states '0' and '1'. Our task will be to study the decay of spin-state superpositions in such quantum-dot systems. The main objective of this thesis is to understand the most important physical processes that lead to spin decoherence and to show ways to suppress this undesirable effect. It turns out that at low temperatures, the main source of decoherence is the coupling of the electron (hole) to the surrounding nuclear spins.

This thesis is divided into three logical parts, corresponding to the three qubit candidate systems under consideration. First we will study electron-spin qubits in III-V semiconductor quantum dots, where the electron spin interacts with the nuclear spins of the semiconducting host material via the isotropic Fermi contact hyperfine interaction. Second we consider quantum-dot-confined heavy holes and the decoherence of their (pseudo-)spin states due to anisotropic interactions with the nuclear spins. Third and last, we study electron-spin qubits made from carbon-nanotube and graphene quantum dots. Quantum dots made of carbon have the advantage of a low abundance of spin-carrying nuclear isotopes, therefore reducing decoherence effects significantly.

For each of the systems under consideration, we will carry out analytical calculations on the nuclear-spin interactions and the spin dynamics of the qubit. Although one main goal of this thesis is to show ways to extend spin decoherence times, we will also focus on physically more fundamental questions. Not only the timescale of the decay is relevant for the system's applicability as a qubit, but also the form of the decay which can vary significantly from system to system. For example, the decay of spin-state superpositions can follow an exponential, super-exponential or power-law decay, and can even pass through various stages. This is not only of academic interest, but also important for practical purposes, such as the implementation of quantum error-correction schemes in a potential quantum computer.

# Contents

Chapter 1

# Preface: Dealing with Decoherence

The dream of building computers that work according to the rules of quantum mechanics has strongly driven research over the last decade, theoretically and experimentally, and in many fields of basic and applied sciences including physics, chemistry, and computer science. About ten years ago, Grover (1997) and Shor (1997) presented novel algorithms, making direct use of quantum phenomena such as interference and entanglement to crucially speed up data searching and prime factorization of large numbers used, e.g., for data encryption. In order to turn quantum computers into a reality, however, many important and unsolved problems need to be addressed, not only in engineering but also (and especially) in basic physics.

One issue of central importance is the physical implementation of the quantum bit (short: qubit) – the quantum analog of the bit processed by today's digital computers. While classical bits can assume any one of the distinct states 0 or 1, qubits can also be in a *coherent superposition* of these two states: *both 0 and 1*. This is where the huge speedup potential of the quantum computer lies: every qubit can be initialized in a superposition of states and therefore many computational operations can be carried out in parallel rather than one by one. In principle, any quantum-mechanical system with two distinct states could be used to encode quantum information, and it comes thus as no surprise that a large variety of candidate qubit systems in many subfields of physics and chemistry have been proposed over the years. Examples are nuclear spins, cold atoms, trapped ions, quantum optical systems, Josepshon junctions, excitons in semiconductors, electrons or holes in quantum dots, impurities, molecular magnets, NV-centers in diamond, and many more.

Throughout this thesis, we will focus on one particular solid state implementation: spin qubits in quantum dots. However, the fundamental challenges described below are shared by essentially all physical implementations.

One of the major problems towards building a quantum computers is the limited *decoherence time*: the qubit is not isolated from its environment, and the unavoidable coupling between the two causes a fast decay of the qubit-state superpositions – see Fig. 1.1(a). This process is called *decoherence*, and the associated decoherence times are rather short, typically in the nano- to microsecond range for solid state systems. However, they can easily vary over many orders of magnitude when changing physical parameters such as temperature, gate potentials,

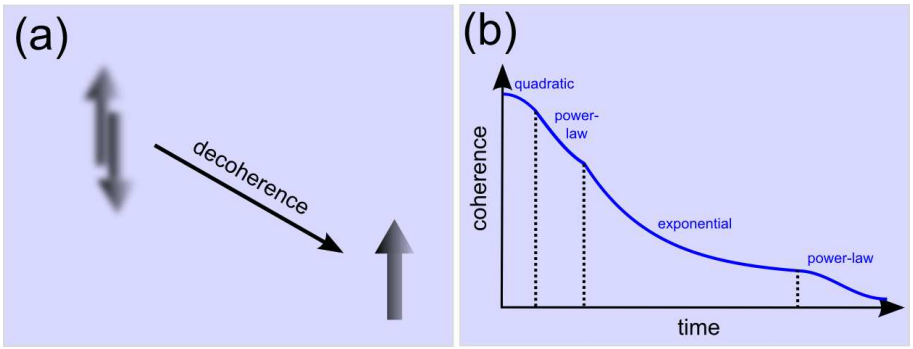


Figure 1.1: (a) Decoherence manifests itself in the decay of spin-state superpositions: the state '↑ and ↓' becomes '↑ or ↓'. (b) The decoherence process typically passes through various stages. For example, an electron spin interacting with a 'narrowed' nuclear spin bath shows an initial quadratic and power-law decay of coherent superpositions, followed by an exponential decay at intermediate times and a long-time power-law tail.

magnetic fields, material or isotope composition, confinement geometry, etc.

Building a quantum computer is thus not simply an engineering problem with planable progress. Instead, one quickly faces a complex non-equilibrium problem involving many unwanted interactions with the outside world – especially in solid state systems, where everything starts to interact with everything at some fine enough level – raising the principal question if these interactions will ever allow sufficient coherence on a larger scale. Moreover, realistic decoherence is not of some 'generic type', but rather system-specific. Thus, the devil is in the detail, and only understanding those details can reveal strategies to deal with decoherence, and to eventually find the best qubit. For instance, quantum error-correction schemes, which are essential for scalable quantum computation, almost exclusively assume a Markovian decoherence model, characterized by a single exponential decay in time. However, this is typically oversimplified, and we understand now that there can be an entire 'zoo of decoherence laws', even in one and the same system, with a time decay that proceeds through several different stages. An illustrative example of this dynamics is given in Fig. 1.1 (b) for spins in quantum dots, from today's point of view one of the most promising qubit candidates. It is this fundamental aspect which has added to the fascination and the strive for detailed knowledge of decoherence and which has opened up a completely new field of research over the past few years.

The qubit in a quantum dot – a small region within a semiconductor – consists of a single electron whose spin states ↓ and ↑ represent the logical states 0 and 1 (Loss and DiVincenzo, 1998; Hanson et al., 2007). Such quantum-dot electrons can be initialized in any spin state, the state can be read out, and two neighboring spins can be coupled and decoupled. Thus, all basic prerequisites for universal quantum computation are fulfilled (Cerletti et al., 2005). An attractive feature of this qubit system is that it can be operated in an all-electrical way, despite the fact that the quantum information is stored in the magnetic moment of the electron spin. This allows the use of standard gate technologies which are flexible, fast, and inherently scal-

able. The desired size would be a 'quantum chip' that contains about 10,000 qubits. Currently, only two spin qubits have been implemented, but many more seem feasible.

Research so far has mainly focused on GaAs (and also InAs) semiconductors mostly because of the advanced nanofabrication techniques available for them (Hanson et al., 2007). The quantum dots come in various forms such as gate-defined, strain-induced, self-assembled, in nanowires, etc. In these materials, the cause of decoherence at milli-Kelvin temperatures are nuclear spins: typically a million of them reside inside a quantum dot and they all couple to the single electron spin via the hyperfine interaction (Coish and Loss, 2004). They create a random magnetic field which leads to fluctuations in the electron spin precession – a random 'staggering' – and thus to decoherence. This happens fast, typically within tens of nanoseconds. In stark contrast to this, the mere flip of the electron spin, i.e., a transition from $\uparrow$ to $\downarrow$ (typically due to lattice vibrations), can be extremely slow, even exceeding seconds (Amasha et al., 2008). For quantum computation to be viable, the coherence of a single qubit must be preserved during roughly 10,000 qubit operations. Although two-qubit operations to generate entanglement have already been demonstrated on a remarkably short timescale of only about 0.2 nanoseconds (Petta et al., 2005), the decoherence time compared to this is still not long enough. From today's point of view, a minimum decoherence time of several microseconds would be desirable. However, the situation is not hopeless, and several strategies have been proposed – and some implemented successfully – to deal with the problem of short decoherence times, and some of them will be discussed throughout this thesis.

A standard method to extend coherence, borrowed from nuclear magnetic resonance, is to apply magnetic field pulses (spin-echo sequences), which partly reverse the electron spin dynamics, thereby prolonging its coherence, even up to microseconds (Koppens et al., 2008).

Another idea is to prepare the nuclear spin bath in some less noisy state with a narrowed distribution width (Coish and Loss, 2004). Such state preparations have already been successfully implemented in gated and self-assembled quantum dots (Greilich et al., 2007; Reilly et al., 2008). The dynamics of an electron spin interacting with a narrowed nuclear-spin bath vary drastically from the non-narrowed situation, as we will show in Chapters 3 and 4 of this thesis.

Another strategy is to polarize the nuclear spins dynamically by spin-blockaded transport (Ono and Tarucha, 2004), or by cooling to ultra-low temperatures (milli-Kelvin or below) with the goal to freeze out the nuclear spins in a high magnetic field. Furthermore, as recently proposed (Braunecker et al., 2009a,b), it is also possible to induce a magnetic phase transition in the nuclear spin system, with a transition temperature that is strongly enhanced from the micro- to the milli-Kelvin regime by correlations effects present in one- or two-dimensional electron gases. For the polarization method to be effective, a polarization of close to 100% would be necessary. As for now, however, no more than 60% polarization have been achieved experimentally (Bracker et al., 2005).

Very recently, proposals have been made to use the spin of a confined hole as a quantum bit, rather than that of an electron, due to surprisingly long spin relaxation times recently predicted and observed (Heiss et al., 2007). A hole is simply a vacancy in the valence band of a semiconductor – a 'non-existing electron' – which behaves like a real particle. It has been shown theoretically (Fischer et al., 2008) that the hole couples to the nuclear environment in

a qualitatively different way – 'Ising-like' –, and that hole-spin decoherence times easily reach several tens of microseconds, even without manipulations on the nuclear spins (see Chapter 5) In addition, nuclear state preparations might be more efficient than for electrons, potentially prolonging the decoherence time even further. The possibility to initialize and read out single hole spins in flat dots has already been demonstrated (Gerardot et al., 2008), and first hole-spin decoherence-time measurements have been carried out (Brunner et al., 2009), confirming the theoretically predicted timescales.

The presence of nuclear spins is not only a nuisance, but can also be exploited to one's advantage. Manipulating the nuclear spins allows for control over the electron spin, and the necessary coupling between two qubits can even be mediated by nuclear spins (Petta et al., 2005). Moreover, the nuclear-spin system itself is considered suitable for information storage, as it is known to be more robust against perturbations from the environment due its much weaker magnetic coupling.

There also remains the possibility of exploring new materials. Quantum dots in carbon-based materials such as nanotubes, graphene or diamond, or in type-IV semiconductors (especially Si/Ge nanowires) have been investigated recently with a view towards spin qubits. These materials have the advantage of low abundances of spin-carrying nuclear isotopes, thus exhibiting significantly weaker nuclear-spin interactions of the confined electron. For instance, natural carbon consist of 99 percent nuclei with zero spin, and only of one percent nuclei with non-zero spin. Coherent dynamics of single spins in diamond have already been reported (Hanson et al., 2008), and decoherence times of order microseconds have been measured (Jelezko et al., 2004). For quantum dots in graphene (a single atomic layer of graphite) and carbon nanotubes, theory predicts a rather weak coupling of the confined electron to the nuclear spins (Fischer et al., 2009), as shown in Chapter 7 of this thesis. First experiments, however, have seen a fast spin decoherence in carbon nanotubes (Churchill et al., 2009a,b), and it is a subject of ongoing research to resolve this discrepancy.

Finally, many proposals for hybrid systems have been made recently, suggesting the coupling of, e.g., spins to long-wavelength photons in stripline cavities. This opens up the possibility to store the quantum information in one qubit type and process the information in another one, combining so-to-speak the best of all worlds.

No doubt, there is still a long way to go before a practical quantum computer will be a reality – and in order to achieve this goal basic research on decoherence will be crucial. For instance, the question of scalability will have to be addressed: for a useful quantum computer, tens of thousands of qubits would be required, all coupled in some controllable way. Nevertheless, the slow but steady progress over the last decade is encouraging, and many workers in the field are cautiously optimistic that the goal will be reached eventually.

Chapter 2

# Introduction: Nuclear-Spin Interactions in Semiconductor Quantum Dots

## 2.1 Open systems and quantum master equations

Throughout this thesis, we will be confronted with having to deal with systems with an enormously large number of degrees of freedom. For instance, the Hilbert space of $N$ spin-$\frac{1}{2}$ particles has a dimension of $2^N$, where $N$ is typically on the order of $10^4$ to $10^6$. Solving an equation of motion for such a large system is virtually impossible, even numerically. Fortunately, it is often possible to divide the total system into some part whose dynamics we would like to study and some other part whose time evolution may be irrelevant to us. So instead of solving the equations of motion for the total system, we can tackle the technically much easier task of studying the dynamics of the small relevant part (the 'open system' $S$) which interacts with the large irrelevant part (the 'bath' or 'environment' $E$) – see also Fig. 2.1. In this section we will introduce the concept of an open quantum system and derive a closed equation of motion ('master equation') which we will use in the rest of this thesis to describe the dynamics of open systems. Our derivation closely follows the one given by Breuer and Petruccione (2002).

Let us assume that the state of the total system $S + E$ is described by a density matrix $\rho$, while the states of system and environment are described by $\rho_S$ and $\rho_E$, respectively, such that

$$\rho_{S(E)} = \mathrm{tr}_{E(S)}\rho, \tag{2.1}$$

where $\mathrm{tr}_{S(E)}$ denotes the partial trace over the system (environment) degrees of freedom. Suppose the Hamiltonian of the total system can be written as

$$H = H_0 + V, \tag{2.2}$$

where $H_0$ denotes the unperturbed part of the Hamiltonian, which can include both system and environment degrees of freedom and which can be solved exactly, and where $V$ denotes a perturbation.

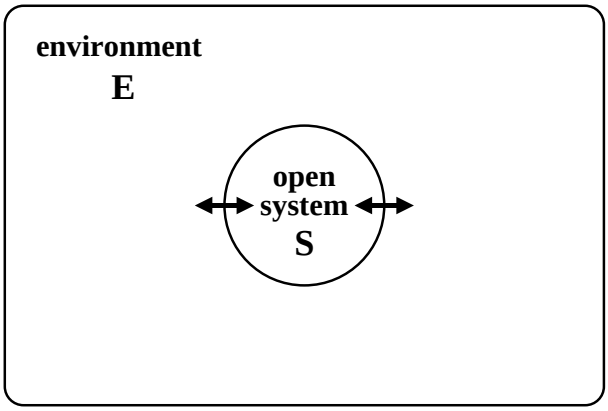


Figure 2.1: Open quantum system $S$ interacting with an environment $E$.

In order to derive a closed equation of motion for the reduced density matrix $\rho_S$, it is convenient to introduce a projection superoperator $\mathsf{P}$, which projects the total density matrix $\rho$ onto some relevant part $\mathsf{P}\rho$. In principle $\mathsf{P}$ can have any form that obeys the following conditions: *(i)* $\mathsf{P}^2 = \mathsf{P}$ ($\mathsf{P}$ is a projector) and *(ii)* $\mathrm{tr}_S\{\rho A_S\} = \mathrm{tr}_S\{\mathsf{P}\rho A_S\}$ ($\mathsf{P}$ does not change the expectation value of any system operator $A_S$). We also introduce the inverse projector $\mathsf{Q}$, whis is defined via $\mathsf{P} + \mathsf{Q} = 1$ and which projects the total density matrix onto its irrelevant part $\mathsf{Q}\rho = \rho - \mathsf{P}\rho$. The standard choice of the projector $\mathsf{P}$ is given by

$$\mathsf{P}\rho = (\mathrm{tr}_E\rho) \otimes \rho_E \equiv \rho_S \otimes \rho_E, \tag{2.3}$$

in analogy to Eq. (2.1). The standard projector (2.3) projects the total density matrix $\rho$ onto a product state of system and environment. In principle, other choices of $\mathsf{P}$ are possible which, e.g., project onto correlated system-bath states (Breuer et al., 2006; Breuer, 2007; Fischer and Breuer, 2007; Ferraro et al., 2008; Huang and Yi, 2008).

We start our derivation of a closed master equation for the relevant part $\mathsf{P}\rho$ from Liouville's equation for the total density matrix $\rho$,

$$\frac{d}{dt}\,\rho(t) = -i\,[H, \rho(t)] \equiv -i\,\mathsf{L}\,\rho(t), \tag{2.4}$$

where we have introduced the Liouvillian $\mathsf{L}$. Applying $\mathsf{P}$ and $\mathsf{Q}$ yields

$$\mathsf{P}\,\frac{d}{dt}\,\rho(t) = \frac{d}{dt}\,\mathsf{P}\rho(t) = -i\,\mathsf{PL}\,\rho(t), \tag{2.5}$$

$$\mathsf{Q}\,\frac{d}{dt}\,\rho(t) = \frac{d}{dt}\,\mathsf{Q}\rho(t) = -i\,\mathsf{QL}\,\rho(t), \tag{2.6}$$

since $\mathsf{P}$ and $\mathsf{Q}$ do not depend on time. Inserting $\mathsf{P} + \mathsf{Q} = 1$ into Eqs. (2.5) and (2.6) leads to

$$\frac{d}{dt}\,\mathsf{P}\rho(t) = -i\,\mathsf{PLP}\,\rho(t) - i\,\mathsf{PLQ}\,\rho(t), \tag{2.7}$$

$$\frac{d}{dt}\,\mathsf{Q}\rho(t) = -i\,\mathsf{QLP}\,\rho(t) - i\,\mathsf{QLQ}\,\rho(t). \tag{2.8}$$

A formal solution of (2.8) is given by

$$\mathsf{Q}\rho(t) = \mathcal{G}(t,t_0)\mathsf{Q}\rho(t_0) - i\int_{t_0}^{t} ds\, \mathcal{G}(t,s)\mathsf{QLP}\rho(s) \tag{2.9}$$

with the propagator

$$\mathcal{G}(t,s) = T_{\leftarrow}\exp\left\{-i\int_s^t ds'\, \mathsf{QL}(s')\right\}. \tag{2.10}$$

Here, we allow for a time-dependent Liouvillian $\mathsf{L}$, such that $T_{\leftarrow}$ denotes chronological time ordering. Inserting Eq. (2.9) into Eq. (2.7), we obtain the so-called Nakajima-Zwanzig master equation for the reduced density matrix $\mathsf{P}\rho$:

$$\frac{d}{dt}\mathsf{P}\rho(t) = -i\,\mathsf{PL}(t)\mathsf{P}\,\rho(t) - i\,\mathsf{PL}(t)\mathcal{G}(t,t_0)\mathsf{Q}\rho(t_0) - \int_{t_0}^{t} ds\,\mathsf{PL}(t)\mathcal{G}(t,s)\mathsf{QL}(s)\mathsf{P}\rho(s). \tag{2.11}$$

Eq. (2.11) is an exact equation describing the time evolution of the relevant part $\mathsf{P}\rho$. In general, it is, however, impossible to solve Eq. (2.11) direcly because of the complicated structure of the convolution integral. In most cases, it is therefore necessary to resort to some approximation scheme. It will be convenient to intruduce the memory kernel or self-energy

$$\Sigma(t,s) = -i\mathsf{PL}(t)\mathcal{G}(t,s)\mathsf{QL}(s)\mathsf{P}. \tag{2.12}$$

We now carry out some simplifications on Eq. (2.11) which will give us the basis to work with for the rest of this thesis.

1. If the initial system-bath state is a product state, i.e. if $\mathsf{P}\rho(t_0) = \rho(t_0)$, then $\mathsf{Q}\rho(t_0) = 0$ and the inhomogeneity (the second term on the right-hand side of Eq. (2.11)) vanishes.

2. If the Hamiltonian (2.2) does not depend explicitly on time, we have

$$\mathcal{G}(t,s) = e^{-i\mathsf{QL}(t-s)} = \mathcal{G}(t-s), \qquad \Sigma(t,s) = \Sigma(t-s). \tag{2.13}$$

3. Let us assume that in Eq. (2.2), the energy scales associated with $H_0$ are much larger than those associated with $V$. It is then possible to carry out a systematic expansion of the memory kernel in powers of the perturbation $V$ by writing $\mathsf{L} = \mathsf{L}_0 + \mathsf{L}_V$ and iterating Dyson's identity

$$e^{i\mathsf{Q}(\mathsf{L}_0+\mathsf{L}_V)t} = e^{i\mathsf{QL}_0 t} - i\int_0^t dt'\, e^{-i\mathsf{QL}_0(t-t')}\mathsf{QL}_V e^{-i\mathsf{QL}t'} \tag{2.14}$$

up to the desired order in $\mathsf{L}_V$. As we will see later on, it is often convenient to solve the Nakajima-Zwanzig equation (2.11) in Laplace space (up to some order in $\mathsf{L}_V$). The Dyson identity may then be written as

$$\frac{1}{s+i\mathsf{QL}} = \sum_{k=0}^{\infty}\frac{1}{s+i\mathsf{QL}_0}\left(-i\mathsf{QL}_v\frac{1}{s+i\mathsf{QL}_0}\right)^k, \tag{2.15}$$

where we have iterated the operator identity

$$\frac{1}{A+B} = \frac{1}{A}\left(1 - B\frac{1}{A+B}\right) \tag{2.16}$$

for $A = s + i\mathsf{QL}_0$ and $B = i\mathsf{QL}_V$.

## 2.2 Electron-nuclear spin interactions

In this section, we give a microscopic derivation of the nuclear-spin interactions that will be considered througout this thesis. The interaction of a relativistic electron with the electromagnetic field created by a nucleus is described by the Dirac Hamiltonian

$$H_D = \boldsymbol{\alpha} \cdot \boldsymbol{\pi} + \beta mc^2 + qV, \tag{2.17}$$

where $m$ is the electron rest mass, $q = -|e|$ is the electron charge, $\boldsymbol{\pi} = c(\mathbf{p} - q\mathbf{A})$, $c$ is the speed of light, $\mathbf{p}$ is the momentum, $V$ and $\mathbf{A}$ are the scalar and vector potential of the electromagnetic field induced by the nucleus, and

$$\boldsymbol{\alpha} = \begin{pmatrix} 0 & \boldsymbol{\sigma} \\ \boldsymbol{\sigma} & 0 \end{pmatrix}, \quad \boldsymbol{\beta} = \begin{pmatrix} \mathbf{1} & 0 \\ 0 & -\mathbf{1} \end{pmatrix} \tag{2.18}$$

are the $4 \times 4$ Dirac matrices with $\boldsymbol{\sigma}$ being the vector of Pauli matrices and $\mathbf{1}$ the $2 \times 2$ identity matrix.

The Dirac Hamiltonian (2.17) acts on a 4-spinor $\psi = (\chi_1, \chi_2)^t$, where $\chi_1$ and $\chi_2$ are 2-spinors describing the electron and the positron, respectively. Using this notation, the Dirac equation $H_D\psi = E\psi$, with $E = mc^2 + \epsilon$, may be written as a pair of coupled equations for the $\chi_j$:

$$(\epsilon - qV)\,\chi_1 - \boldsymbol{\sigma} \cdot \boldsymbol{\pi}\,\chi_2 = 0, \tag{2.19}$$

$$-\boldsymbol{\sigma} \cdot \boldsymbol{\pi}\,\chi_1 + (2mc^2 - qV + \epsilon)\,\chi_2 = 0. \tag{2.20}$$

Isolating $\chi_2$ in Eq. (2.20) and inserting into Eq. (2.19) yields the following eigenvalue equation for the electron:

$$\left(\boldsymbol{\sigma} \cdot \boldsymbol{\pi}\, \frac{1}{2mc^2 - qV + \epsilon}\, \boldsymbol{\sigma} \cdot \boldsymbol{\pi} + qV\right) \chi_1 = \epsilon\chi_1. \tag{2.21}$$

In the non-relativistic limit $(\epsilon - qV)/mc^2 \to 0$, $\chi_1$ and $\chi_2$ decouple and Eq. (2.21) reduces to the Pauli equation $H_P\chi_1 = \epsilon\chi_1$ with the Pauli Hamiltonian

$$H_P = \frac{1}{2m}\,(\mathbf{p} - q\mathbf{A})^2 - \frac{q\hbar}{2m}\,(\boldsymbol{\nabla} \times \mathbf{A}) \cdot \boldsymbol{\sigma} + qV. \tag{2.22}$$

In general, one has to take into account the relativistic effect of a coupling between the electron and positron 2-spinors. It is, however, possible to systematically decouple $\chi_1$ and $\chi_2$ in orders of $1/mc^2$ by successively applying unitary transformations to the Dirac Hamiltonian (2.17). This method takes into account relativistic corrections to the Pauli equation and is known as the *Foldy-Wouthuysen transformation*. In lowest order, this method leads to an eigenvalue equation $H_{\mathrm{FW}}\chi_1 = \epsilon\chi_1$ for the electron spinor, where $H_{\mathrm{FW}}$ contains the Pauli Hamiltonian and the first relativistic corrections:

$$H_{\mathrm{FW}} = H_P - \frac{q\hbar}{4m^2c^2}\,\left(\mathbf{E} \times \frac{\boldsymbol{\pi}}{c}\right) \cdot \boldsymbol{\sigma} - \frac{q\hbar^2}{8m^2c^2}\,\boldsymbol{\nabla} \cdot \mathbf{E}, \tag{2.23}$$

where we have introduced the electric field $\mathbf{E} = -\boldsymbol{\nabla}V$.

The terms of interest are those that couple the nucleus (giving rise to $\mathbf{E}$ and $\mathbf{A}$) through their charge and magnetic moment to the electron (with spin $\boldsymbol{\sigma}$ and momentum $\mathbf{p}$). These terms are

$$H_{\rm so} = -\frac{q\hbar}{4m^2c^2}\,(\mathbf{E}\times\mathbf{p})\cdot\boldsymbol{\sigma}, \tag{2.24}$$

$$H_{\rm ihf} = \frac{q^2\hbar}{4m^2c^2}\,(\mathbf{E}\times\mathbf{A})\cdot\boldsymbol{\sigma}, \tag{2.25}$$

$$H_{\rm ahf} = -\frac{q\hbar}{2m}\,(\boldsymbol{\nabla}\times\mathbf{A})\cdot\boldsymbol{\sigma}, \tag{2.26}$$

$$H_{\rm ang} = -\frac{q}{m}\,\mathbf{A}\cdot\mathbf{p}, \tag{2.27}$$

and are referred to as spin-orbit interaction, isotropic hyperfine interaction, anisotropic hyperfine interaction, and the coupling of electron orbital angular momentum to the nuclear spin, respectively.

The spin-orbit interaction manifests itself via a splitting of the electron spin states at $\mathbf{k}\neq 0$ (away from the center of the Brillouin zone), even at zero external magnetic field. This splitting can be due to the bulk inversion asymmetry (BIA) of the crystal, or due to structure inversion asymmetry (SIA) caused, e.g., by a confinement potential (Winkler, 2003). In III-V semiconductor quantum dots, both effects can be relevant: the zincblende-type crystal structure of III-V semiconductors lacks a center of inversion symmetry, causing BIA, while the strong two-dimensional confinement of the quantum dot leads to SIA. However, the spin-orbit interaction depends on temperature, as it is typically mediated by phonons. At low temperatures (typically lower than 1K for III-V semiconductor quantum dots) the spin-orbit contribution to the dephasing of the electron spin is typically much smaller than the effect of the nuclear-spin interactions. We will therefore neglect spin dephasing due to spin-orbit interactions in this thesis.

The importance of nuclear-spin interactions stongly depends on the system under consideration. For most quantum dots at low temperatures, the main mechanism leading to spin decoherence of electrons is the isotropic hyperfine interaction (2.25) – see Chaps. 3 and 4 –, while for holes the anisotropic hyperfine interaction (2.26) and the coupling to orbital angular momentum (2.27) are most relevant – see Chap. 5. It is convenient to replace the nuclear-spin interactions (2.25) - (2.27) by equivalent effective Hamiltonians of the form (Abragam, 1961; Stoneham, 1972)

$$H_{\rm ihf}^{\rm eff} = \frac{\mu_0}{4\pi}\,\frac{8\pi}{3}\,2\mu_B\gamma_N\delta(\mathbf{r})\mathbf{S}\cdot\mathbf{I}, \tag{2.28}$$

$$H_{\rm ahf}^{\rm eff} = \frac{\mu_0}{4\pi}\,2\mu_B\gamma_N\frac{3(\mathbf{n}\cdot\mathbf{S})(\mathbf{n}\cdot\mathbf{I})-\mathbf{S}\cdot\mathbf{I}}{r^3(1+d/r)}, \tag{2.29}$$

$$H_{\rm ang}^{\rm eff} = \frac{\mu_0}{4\pi}\,2\mu_B\gamma_N\frac{\mathbf{L}\cdot\mathbf{I}}{r^3(1+d/r)}. \tag{2.30}$$

Here, $\mu_0$ is the vacuum permeability, $\gamma_N = g_N\mu_N$ is the nuclear gyromagnetic ratio, $g_N$ is the nuclear g-factor, $\mu_B$ ($\mu_N$) is the Bohr (nuclear) magneton, $\mathbf{r}$ is the vector pointing from the nucleus to the electron, $r=|\mathbf{r}|$, $\mathbf{n}=\mathbf{r}/r$, $d\simeq Z\times 1.5\times 10^{-15}$ m is a length of nuclear dimension ($Z$ is the effective nuclear charge), $\mathbf{S}$ ($\mathbf{I}$) is the electron (nuclear) spin operator, and $\mathbf{L}$ is the

electron orbital angular momentum operator. Eqs. (2.28) - (2.30) will serve as a starting point for all considerations throughout this thesis.

## 2.3 Band structure of III-V semiconductors

In this section, we want to sketch how the bandstructure of a III-V semiconductor can in principle be derived from miscroscopic considerations. We will refrain from showing a complete derivation, since this is a subject of many excellent textbooks (see, e.g., Winkler (2003) or Yu and Cardona (2005)), but rather give an idea about which ingredients need to be taken into account.

Our starting point is the Schrödinger equation for a particle with rest mass $m_0$ in a periodic potential $V_0$:

$$\left(\frac{\mathbf{p}^2}{2m_0} + V_0(\mathbf{r})\right)\psi_{n\mathbf{k}}(\mathbf{r}) = E_n(\mathbf{k})\psi_{n\mathbf{k}}(\mathbf{r}), \tag{2.31}$$

where $\psi_{n\mathbf{k}}(\mathbf{r}) = e^{i\mathbf{k}\cdot\mathbf{r}}u_{n\mathbf{k}}(\mathbf{r})$ is the Bloch function of the particle. Applying $\mathbf{p}^2$ to the Bloch function, we can rewrite Eq. (2.31) as a function for the lattice-periodic Bloch amplitude $u_{n\mathbf{k}}(\mathbf{r})$ alone:

$$\left(\frac{\mathbf{p}^2}{2m_0} + V_0(\mathbf{r}) + \frac{\hbar^2k^2}{2m_0} + \frac{\hbar}{m_0}\,\mathbf{k}\cdot\mathbf{p}\right)u_{n\mathbf{k}}(\mathbf{r}) = E_n(\mathbf{k})u_{n\mathbf{k}}(\mathbf{r}). \tag{2.32}$$

For III-V semiconductors, the extrema of the relevant bands are at the Γ-point ($\mathbf{k} = \mathbf{0}$), where we have

$$\left(\frac{\mathbf{p}^2}{2m_0} + V_0(\mathbf{r})\right)u_{n\mathbf{0}}(\mathbf{r}) = E_{n\mathbf{0}}u_{n\mathbf{0}}(\mathbf{r}). \tag{2.33}$$

The solutions of Eq. (2.33) form a complete set of basis functions, and once $E_{n\mathbf{0}}$ and $u_{n\mathbf{0}}(\mathbf{r})$ are known, we can include the $\mathbf{k}$-dependent terms in Eq. (2.32) perturbatively.

Since spin-orbit coupling plays an important role concerning the bandstructure, we also need to take into account the Pauli spin-orbit term (2.24). In the basis $\{u_{n\mathbf{0}\sigma}\}$ (including spin $\sigma = \uparrow, \downarrow$) we can now express the Hamiltonian

$$H = \frac{\mathbf{p}^2}{2m_0} + V_0(\mathbf{r}) + \frac{\hbar^2k^2}{2m_0} + \frac{\hbar}{m_0}\,\mathbf{k}\cdot\mathbf{p} - \frac{q\hbar}{4m^2c^2}\,(\mathbf{E}\times\mathbf{P})\cdot\boldsymbol{\sigma}, \qquad \mathbf{P} = \mathbf{p} + \hbar\mathbf{k}, \tag{2.34}$$

as an infinite-dimensional matrix with elements $\langle u_{n\mathbf{0}}|H|u_{n'\mathbf{0}}\rangle$. For practical purposes, we will need restrict ourselves to some finite amount of energy bands (labelled by $n$) in the vicinity of the fundamental band gap. Typically, one takes into account the conduction band (CB) and the heavy-hole (HH), light-hole (LH) and split-off (SO) valence bands (see also Fig. 2.2), leading to an effective $8 \times 8$ Hamiltonian (four bands including spin).

The explicit form of the Bloch amplitides at the Γ-point depends on the periodicity of the potential $V_0$. For III-V semiconductors, $V_0$ has the symmetry of the zincblende lattice. Although it is not possible to derive an explicit form for the functions $u_{n\mathbf{0}}$ within the framework of the so-called $\mathbf{k}\cdot\mathbf{p}$ theory shown above, their behavior under symmetry operations can be determined via group theory (Dresselhaus et al., 2008). With this information, it is possible to write the Hamoltonian (2.34) up to second order in $\mathbf{k}$ in the basis

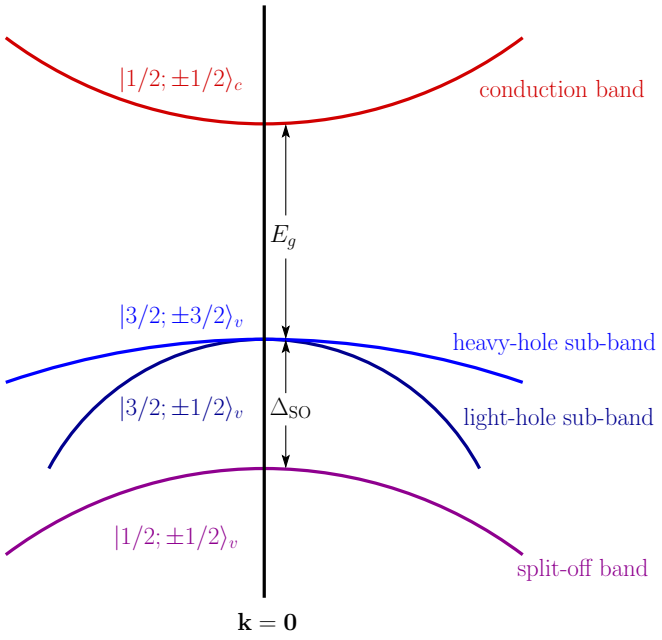


Figure 2.2: Band structure of bulk III-V semiconductors near the Γ-point.

$\{u_{\mathrm{CB}\mathbf{0}\uparrow}, u_{\mathrm{CB}\mathbf{0}\downarrow}, u_{\mathrm{HH}\mathbf{0}\uparrow}, u_{\mathrm{HH}\mathbf{0}\downarrow}, u_{\mathrm{LH}\mathbf{0}\uparrow}, u_{\mathrm{LH}\mathbf{0}\downarrow}, u_{\mathrm{SO}\mathbf{0}\uparrow}, u_{\mathrm{SO}\mathbf{0}\downarrow}\}$ as

$$H_K = \begin{pmatrix} H_{\mathrm{CB}} & V_1 & V_2 & V_3 \\ V_1^\dagger & H_{\mathrm{HH}} & V_4 & V_5 \\ V_2^\dagger & V_4^\dagger & H_{\mathrm{LH}} & V_6 \\ V_3^\dagger & V_5^\dagger & V_6^\dagger & H_{\mathrm{SO}} \end{pmatrix}, \tag{2.35}$$

with the $2\times2$ matrices $H_n$ and $V_m$. This is the so-called $8\times8$ Kane Hamiltonian and it can be interpreted as follows: The $2\times2$ Hamiltonians $H_n$ describe the unperturbed electron states in the band $n$, while the off-diagonal blocks $V_m$ couple the bands to each other. An explicit form of the $2\times2$ blocks is given in Appendix B.1 for the quasi-two-dimensional case of a quantum well (see, e.g., Winkler (2003) for the bulk case).

It is now possible to project the $8\times8$ Kane Hamiltonian onto the band of interest using quasi-degenerate perturbation theory (see, e.g., Appendix B of Winkler (2003)). In lowest order this procedure will lead to a Hamiltonian whose eigenstates are just the unperturbed states $u_{n\mathbf{0}}$ (where $n$ is the band we have projected onto), while higher-order corrections to the wavefunctions will describe hybridization between the bands. We will come back to this in more detail in Chapter 5.

From the explicit form of the Kane Hamiltonian given in Appendix B.1, we can see that at $\mathbf{k}=\mathbf{0}$ the HH and LH states are energetically degenerate (see Fig. 2.2). However, it is possible to lift this degeneracy by confining the crystal to two dimensions, which in practice is typically achieved by growing thin layered structures of different semiconducting materials (Yu and Cardona, 2005). Once the degeneracy is lifted, we are left with a good two-level system

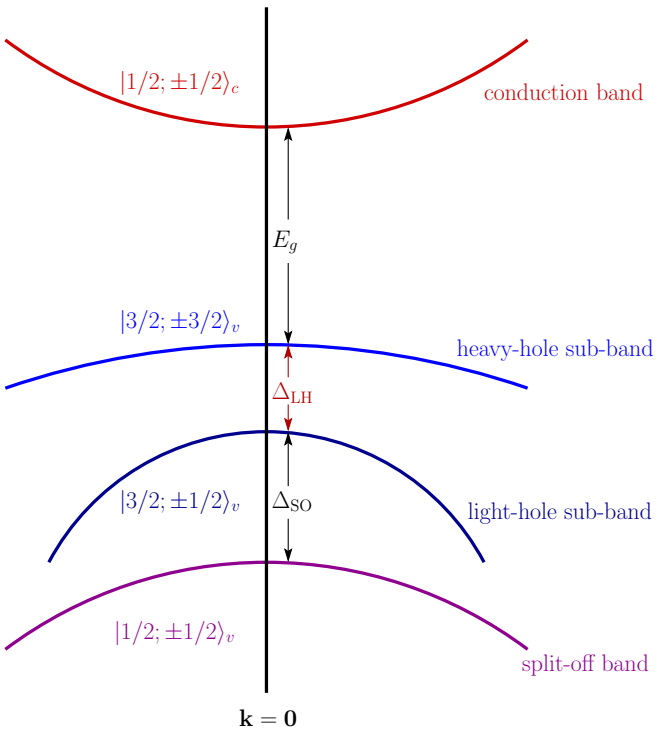


Figure 2.3: Band structure of a III-V semiconductor quantum well near the Γ-point.

in the HH and LH sub-bands, which is important when viewed in the context of hole-spin quantum bits (see Chapter 5).

Chapter 3

# Electrons in III-V Semiconductors: Effective-Hamiltonian Approach

## 3.1 Introduction

We have discussed in Chapter 1 that a promising physical implementation of a quantum bit is to use the spin states of electrons in confined structures (Loss and DiVincenzo, 1998; Hanson et al., 2007; Leuenberger and Loss, 2001; Vrijen et al., 2000; Jelezko et al., 2004). A series of recent experiments on electron spin states in quantum dots (Petta et al., 2005; Koppens et al., 2006), electrons bound to phosphorus donors in silicon (Abe et al., 2004), NV centers in diamond (Jelezko et al., 2004; Childress et al., 2006; Hanson et al., 2006), and molecular magnets (Ardavan et al., 2007) have shown that the hyperfine interaction between confined electron spins and nuclear spins in the surrounding material is the major obstacle to maintaining coherence in these systems.

Previous studies of this decoherence mechanism have pointed to the non-Markovian nature of a slow nuclear-spin environment, leading to non-exponential coherence decay (Khaetskii et al., 2002; Merkulov et al., 2002; de Sousa and Das Sarma, 2003; Breuer et al., 2004; Coish and Loss, 2004; Erlingsson and Nazarov, 2004; Yuzbashyan et al., 2005; Deng and Hu, 2006; Al-Hassanieh et al., 2006; Witzel and Das Sarma, 2007; Yao et al., 2007; Koppens et al., 2007; Chen et al., 2007; Fischer and Breuer, 2007). These results suggest that it may be necessary to revise quantum error correction protocols to accommodate such a 'nonstandard', but ubiquitous environment (Terhal and Burkard, 2005). Here we show that virtual flip-flops between electron and nuclear spins can lead to well-defined Markovian dynamics, giving a simple exponential decay in a large Zeeman field and for particular initial conditions, i.e., a 'narrowed' nuclear-spin state (Coish and Loss, 2004; Klauser et al., 2006; Stepanenko et al., 2006; Giedke et al., 2006). Once such a state is prepared, it can be maintained over an astonishingly long time scale, exceeding hours (Greilich et al., 2007), since spin diffusion processes are highly suppressed near confined electron spins (Klauser et al., 2008). Recently, great progress has been made in experimentally realizing such state narrowing (Greilich et al., 2006, 2007; Reilly et al., 2008; Greilich et al., 2009; Latta et al., 2009; Vink et al., 2009; Xu et al., 2009). Moreover, we

calculate the decoherence time $T_2$, revealing the dependence on many external parameters for a general system.

## 3.2 Effective Hamiltonian: Schrieffer-Wolff transformation

We begin from the Hamiltonian for the Fermi contact hyperfine interaction between a localized spin-1/2 $\mathbf{S}$ and an environment of nuclear spins (see Chapter 2),

$$H_{\rm hf} = bS^z + b\sum_k \gamma_k I_k^z + \mathbf{S}\cdot\mathbf{h}, \tag{3.1}$$

with the Overhauser operator defined by

$$\mathbf{h} = \sum_k A_k \mathbf{I}_k. \tag{3.2}$$

Here, $\mathbf{I}_k$ is the nuclear spin operator for the spin at site $k$ with associated hyperfine coupling constant $A_k$, $b = g^*\mu_{\rm B}B$ is the electron Zeeman splitting in an applied magnetic field $B$ and $\gamma_k$ is the nuclear gyromagnetic ratio in units of the electron gyromagnetic ratio (we set $\hbar = 1$): $\gamma_k = g_{I_k}\mu_N/g^*\mu_B$. For an electron with envelope wave function $\psi(\mathbf{r})$, we have $A_k = v_0 A^{i_k}|\psi(\mathbf{r}_k)|^2$, where $A^{i_k}$ is the total coupling constant to a nuclear spin of species $i_k$ at site $k$ and $v_0$ is the volume of a unit cell containing one nucleus. For convenience, we define $A = \sqrt{\sum_i \nu_i \left(A^i\right)^2}$, where $\nu_i$ is the relative concentration of isotope $i$. The envelope function $\psi(\mathbf{r})$ of the bound electron has finite extent, and consequently there will be a finite number $\sim N$ of nuclei with appreciable $A_k$. For typical quantum dots, $N \sim 10^4 - 10^6$, and for donor impurities or molecular magnets, $N \sim 10^2 - 10^3$. In Eq. (3.1) we have neglected the anisotropic hyperfine interaction, dipole-dipole interaction between nuclear spins, and nuclear quadrupolar splitting, which may be present for nuclear spin $I > 1/2$. The anisotropic hyperfine interaction gives a small correction (due to hybridization with the $p$-type valence bands) for electrons in a primarily $s$-type conduction band (Abragam, 1961), such as in III-V semiconductors. Nuclear dipole-dipole coupling can give rise to dynamics in the spin bath, which can lead to electron-spin decay due to spectral diffusion on a time scale found to be $T_M \sim 10 - 100\,\mu$s for GaAs quantum dots (de Sousa and Das Sarma, 2003; Yao et al., 2006; Witzel and Sarma, 2006). These times are one to two orders of magnitude longer than the $T_2$ we predict for a GaAs quantum dot carrying $N = 10^5$ nuclei (see Fig. 3.3, below). For smaller systems, we expect the decay mechanism discussed here to dominate dipole-dipole effects substantially. The quadrupolar splitting has also been measured for nanostructures in GaAs, giving inverse coupling strengths on the order of $100\,\mu$s (Yusa et al., 2005), comparable to the dipole-dipole coupling strength, so quadrupolar effects should become relevant on comparable time scales.

For large $b$, we divide $H_{\rm hf} = H_0 + V_{\rm ff}$ into an unperturbed part $H_0$ that preserves $S^z$ and a term $V_{\rm ff}$ that leads to energy non-conserving flip-flops between electron and nuclear spins

(Coish and Loss, 2004):

$$H_{\rm hf} = H_0 + V_{\rm ff}, \tag{3.3}$$
$$H_0 = (b + h^z)\, S^z + b \sum_k \gamma_k I_k^z, \tag{3.4}$$
$$V_{\rm ff} = \frac{1}{2}\left(S_+ h_- + S_- h_+\right). \tag{3.5}$$

Our goal is to find an effective Hamiltonian that eliminates the flip-flop term $V_{\rm ff}$ at leading order. We apply a unitary transformation:

$$\overline{H} = e^S H_{\rm hf} e^{-S}, \tag{3.6}$$

where $S = -S^\dagger$ to ensure unitarity. We now expand Eq. (3.6) in powers of $S$, retaining terms up to $\mathcal{O}\left(V_{\rm ff}^3\right)$, assuming $S \sim \mathcal{O}\left(V_{\rm ff}\right)$:

$$\overline{H} = H_0 + V_{\rm ff} - [H_0, S] - [V_{\rm ff}, S] + \frac{1}{2}[S, [S, H_0]] + \mathcal{O}\left(V_{\rm ff}^3\right). \tag{3.7}$$

To eliminate $V_{\rm ff}$ at leading order, we must choose $S$ to satisfy $V_{\rm ff} - [H_0, S] = 0$. The $S$ that satisfies this relation is given by

$$S = \frac{1}{\mathsf{L}_0} V_{\rm ff}, \qquad \mathsf{L}_0 O = [H_0, O], \tag{3.8}$$

which is of order $V_{\rm ff}$, justifying our previous assumption: $S \sim \mathcal{O}\left(V_{\rm ff}\right)$. Re-inserting Eq. (3.8) into Eq. (3.7), we find, up to corrections that are third-, or higher-order in $V_{\rm ff}$:

$$\overline{H} = H + \mathcal{O}\left(V_{\rm ff}^3\right), \tag{3.9}$$
$$H = H_0 + \frac{1}{2}[S, V_{\rm ff}]. \tag{3.10}$$

Directly evaluating Eq. (3.8) with $H_0$ defined in Eq. (3.4) and $V_{\rm ff}$ defined in Eq. (3.5) gives

$$S = \frac{1}{2}\sum_k A_k \left( \frac{1}{b + h^z + \frac{A_k}{2} - b\gamma_k} S^+ I_k^- - \frac{1}{b + h^z - \frac{A_k}{2} - b\gamma_k} S^- I_k^+ \right). \tag{3.11}$$

Inserting Eq. (3.11) into Eq. (3.10) gives

$$H = |\uparrow\rangle\langle\uparrow| H_\uparrow + |\downarrow\rangle\langle\downarrow| H_\downarrow, \tag{3.12}$$
$$H_\uparrow = \frac{1}{2}(b + h^z) + b\sum_k \gamma_k I_k^z + h_\uparrow, \tag{3.13}$$
$$H_\downarrow = -\frac{1}{2}(b + h^z) + b\sum_k \gamma_k I_k^z - h_\downarrow. \tag{3.14}$$

Here, the contributions resulting from the term second-order in $V_{\rm ff}$ are given explicitly by

$$h_\uparrow = \frac{1}{8}\sum_{k,l} A_k A_l \left( \frac{1}{b + h^z + A_k/2 - b\gamma_k} I_k^- I_l^+ + I_l^- \frac{1}{b + h^z - A_k/2 - b\gamma_k} I_k^+ \right), \tag{3.15}$$
$$h_\downarrow = \frac{1}{8}\sum_{k,l} A_k A_l \left( \frac{1}{b + h^z - A_k/2 - b\gamma_k} I_k^+ I_l^- + I_l^+ \frac{1}{b + h^z + A_k/2 - b\gamma_k} I_k^- \right). \tag{3.16}$$

We can rewrite $H$ in terms of spin operators using $|\uparrow\rangle\langle\uparrow| = \frac{1}{2} + S^z$ and $|\downarrow\rangle\langle\downarrow| = \frac{1}{2} - S^z$, which gives

$$\begin{aligned} H &= (\omega + X)\, S^z + D, && (3.17)\\ X &= (1 - \mathsf{P}_\mathrm{d})\,(h_\uparrow + h_\downarrow)\,, && (3.18)\\ D &= b\sum_k \gamma_k I_k^z + \frac{1}{2}\,(h_\uparrow - h_\downarrow)\,, && (3.19)\\ \omega &= b + h^z + \mathsf{P}_\mathrm{d}\,(h_\uparrow + h_\downarrow)\,. && (3.20) \end{aligned}$$

In the above expressions, we have introduced the diagonal projection superoperator

$$\mathsf{P}_\mathrm{d} O = \sum_l |l\rangle\,\langle l|\,\langle l|\,O\,|l\rangle\,, \tag{3.21}$$

where the index $l$ runs over all nuclear-spin product states $|l\rangle = \bigotimes_k \left|I_k m_k^l\right\rangle$. We now apply the commutation relation $\left[I_k^+, I_l^-\right] = 2I_k^z\delta_{kl}$ and expand the prefactors in Eqs. (3.15) and (3.16) in terms of the smallness parameter

$$\frac{A_k}{b + h^z - b\gamma_k} \sim \frac{1}{N}\frac{A}{b} \ll 1. \tag{3.22}$$

At leading order in the expansion, we find $h_{\uparrow,\downarrow} \approx h_{\uparrow,\downarrow}^{(0)}$, where

$$\begin{aligned} h_\uparrow^{(0)} &= \frac{1}{8}\sum_{k,l}\frac{A_k A_l}{b + h^z - b\gamma_k}\left(I_k^- I_l^+ + I_l^- I_k^+\right), && (3.23)\\ h_\downarrow^{(0)} &= \frac{1}{8}\sum_{k,l}\frac{A_k A_l}{b + h^z - b\gamma_k}\left(I_k^+ I_l^- + I_l^+ I_k^-\right). && (3.24) \end{aligned}$$

By commuting the nuclear spin operators, Eqs. (3.23) and (3.24) can be rewritten to give

$$h_\downarrow^{(0)} = h_\uparrow^{(0)} + \frac{1}{2}\sum_k \frac{A_k^2}{b + h^z - b\gamma_k} I_k^z. \tag{3.25}$$

This relation allows us to approximate the various terms in Eqs. (3.18), (3.19), and (3.20):

$$\begin{aligned} X &\approx (1 - \mathsf{P}_\mathrm{d})\left(2h_\uparrow^{(0)}\right),\\ &= \frac{1}{4}\sum_{k\neq l}\frac{A_k A_l}{b + h^z - b\gamma_k}\left(I_k^- I_l^+ + I_l^- I_k^+\right), && (3.26)\\ D &\approx \sum_k \left(b\gamma_k - \frac{A_k^2}{4\,(b + h^z - b\gamma_k)}\right) I_k^z, && (3.27)\\ \omega &\approx b + h^z + \mathsf{P}_\mathrm{d}\left(2h_\uparrow^{(0)}\right) + \frac{1}{2}\sum_k \frac{A_k^2}{b + h^z - b\gamma_k} I_k^z\\ &= b + h^z + \frac{1}{2}\sum_k \frac{A_k^2}{b + h^z - b\gamma_k}\left(I_k(I_k+1) - (I_k^z)^2\right). && (3.28) \end{aligned}$$

Neglecting further corrections that are smaller by the factor $b\gamma_k/\omega \sim \gamma_k \sim 10^{-3}$ in Eq. (3.26) and terms of order $\lesssim \sum_k \frac{A_k^2}{b+h^z-b\gamma_k} \sim \frac{A^2}{Nb}$ in Eqs. (3.27) and (3.28), we arrive at

$$H = (\omega + X)\, S^z + D, \tag{3.29}$$

with

$$\omega \simeq b + h^z, \tag{3.30}$$

$$D \simeq b \sum_k \gamma_k I_k^z, \tag{3.31}$$

$$X \simeq \frac{1}{2} \sum_{k \neq l} \frac{A_k A_l}{\omega} I_k^- I_l^+. \tag{3.32}$$

The terms of order $\sim A^2/Nb$ may become important on a time scale $\tau \sim Nb/A^2$. In our treatment, this time scale is long compared to the bath correlation time $\tau_c \sim N/A$ in the perturbative regime $A/b < 1$, and so neglecting these terms is justified.

## 3.3 Markov approximation

For large $b$, $H_{\rm hf}$ leads only to an incomplete decay of the longitudinal spin $\langle S_z \rangle_t$ (Coish and Loss, 2004). However, it is still possible for the transverse spin $\langle S_+ \rangle_t$ to decay fully (Deng and Hu, 2006) through a pure dephasing process, which we now describe in detail. We assume that the electron and nuclear systems are initially unentangled with each other and that the nuclear spin system is prepared in a narrowed state (an eigenstate of the operator $\omega$: $\omega \left|n\right\rangle = \omega_n \left|n\right\rangle$) through a sequence of weak measurements (Klauser et al., 2006; Giedke et al., 2006; Stepanenko et al., 2006), polarization pumping (Ramon and Hu, 2007), frequency focusing under pulsed optical excitation (Greilich et al., 2007), or by any other means. For these initial conditions, the dynamics of the transverse electron spin $\langle S_+ \rangle_t$ are described by the exact equation of motion (Coish and Loss, 2004):

$$\langle \dot{S_+} \rangle_t = i\omega_n \langle S_+ \rangle_t - i \int_0^t dt' \Sigma(t-t') \langle S_+ \rangle_{t'}\,, \tag{3.33}$$

with the memory kernel (or self energy)

$$\Sigma(t) = -i \mathrm{tr} S_+ \mathsf{L} e^{-i\mathsf{QL}t} \mathsf{QL} \left|n\right\rangle \left\langle n\right| S_-. \tag{3.34}$$

Here, $\mathsf{L}$ and $\mathsf{Q}$ are superoperators, defined by their action on an arbitrary operator $O$: $\mathsf{L}O = [H, O]$, $\mathsf{Q}O = (1 - \left|n\right\rangle \left\langle n\right| \mathrm{tr}_I)\, O$, where $\mathrm{tr}_I$ indicates a partial trace over the nuclear spin system (see Chapter 2.1).

To remove fast oscillations in $\langle S_+ \rangle_t$ we transform to a rotating frame, in which we define the coherence factor

$$x_t = 2 \exp\left[-i(\omega_n + \Delta\omega)t\right] \langle S_+ \rangle_t \tag{3.35}$$

and associated memory kernel

$$\tilde{\Sigma}(t) = \exp\left[-i(\omega_n + \Delta\omega)t\right] \Sigma(t), \tag{3.36}$$

with frequency shift determined self-consistently through

$$\Delta\omega = -\mathrm{Re}\int_0^\infty dt\tilde{\Sigma}(t). \tag{3.37}$$

Additionally, we change the integration variable to $\tau = t - t'$. The equation of motion for $x_t$ then reads

$$\dot{x}_t = -i\int_0^t d\tau\tilde{\Sigma}(\tau)x_{t-\tau}. \tag{3.38}$$

If $\tilde{\Sigma}(\tau)$ decays to zero sufficiently quickly on the time scale $\tau_c \ll T_2$, where $T_2$ is the decay time of $x_t$, we can approximate $x_{t-\tau} \approx x_t$ and extend the upper limit on the integral to $t \to \infty$ (Markov approximation), giving an exponential coherence decay with a small error $\epsilon(t)$:

$$x_t = x_0\exp\left(-t/T_2\right) + \epsilon(t), \qquad \frac{1}{T_2} = -\mathrm{Im}\int_0^\infty dt\tilde{\Sigma}(t). \tag{3.39}$$

The non-Markovian correction $\epsilon(t)$ can be bounded precisely if $\tilde{\Sigma}(t)$ is known (Fick and Sauermann, 1990):

$$|\epsilon(t)| \leq |\epsilon(t)|_{\max} = 2\int_0^t dt'\left|\int_{t'}^\infty dt''\tilde{\Sigma}(t'')\right|. \tag{3.40}$$

Eq. (3.40) gives a hard bound on the validity of the Markov approximation, and consequently, any corrections to the exponential decay formula. Fig. 3.1 demonstrates an application of Eqs. (3.39) and (3.40) for decay in a homonuclear spin system, which we discuss below.

We note that the integral in Eq. (3.39) becomes undefined if the memory kernel has an asymptotic time dependence $\tilde{\Sigma}(t) \sim 1/t^\alpha$, where $\alpha \leq 1$, and consequently the Markov approximation breaks down in this case. A weaker version of Markovian violation can occur more generally for $\alpha \leq 2$, in which case the bound, Eq. (3.40), may still be small for times $t \sim T_2$, but grows unbounded in time. This situation occurs, for example, in the ohmic spin-boson model (DiVincenzo and Loss, 2005).

## 3.4 Homonuclear system

If only one spin-carrying nuclear isotope is present, then $\gamma_k = \gamma$, independent of the nuclear site. We then approximate $\Sigma(t)$ to leading order in the perturbation $V = XS^z$ (Born approximation, see Appendix A.2) by expanding Eq. (3.34) through iteration of the Dyson identity,

$$e^{-i\mathsf{L}\mathsf{Q}t} = e^{-i\mathsf{L}_0\mathsf{Q}t} - i\int_0^t dt' e^{-i\mathsf{L}_0\mathsf{Q}(t-t')}\mathsf{L}_V\mathsf{Q}e^{-i\mathsf{L}\mathsf{Q}t'}, \tag{3.41}$$

where $\mathsf{L}_V O = [V, O]$. Higher-order corrections to the Born approximation will be suppressed by the small parameter $A/\omega_n$ (Coish and Loss, 2004). Inserting the result into Eq. (3.39) we find:

$$\frac{1}{T_2} = \mathrm{Re}\int_0^\infty dt e^{-i\Delta\omega t}\left\langle X(t)X\right\rangle, \qquad X(t) = e^{-i\omega t}Xe^{i\omega t}. \tag{3.42}$$

Here, $\langle\cdots\rangle = \langle n|\cdots|n\rangle$ denotes an expectation value with respect to the initial nuclear state. Eq. (3.42) resembles the standard result for pure dephasing in a weak coupling expansion, where

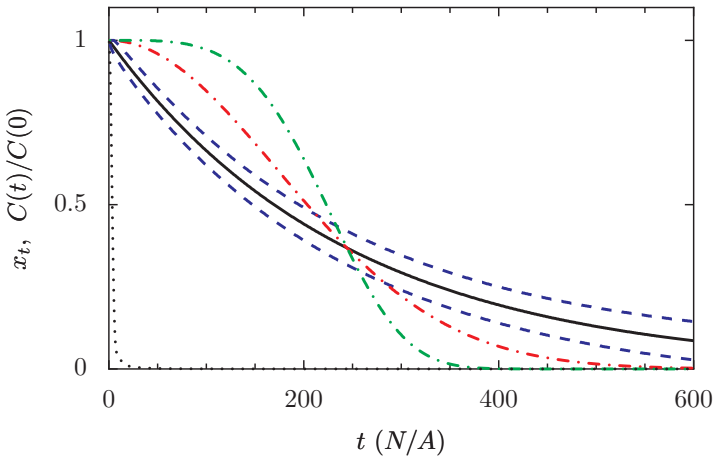


Figure 3.1: Exponential decay $x_t = \exp(-t/T_2)$ (solid line) and maximum error bounds $x_t \pm |\epsilon(t)|_{\max}$ (dashed lines), found by numerical integration of Eq. (3.40) with parameters for a two-dimensional quantum dot (before Eq. (3.50)), $I = 3/2$ and $A/b = 1/20$. For comparison, we show the decay curves for super-exponential forms $\exp\{-(t/T_2)^2\}$ and $\exp\{-(t/T_2)^4\}$ (dot-dashed lines) and rapidly decaying bath correlation function $C(t)/C(0)$ (dotted line, see Eqs. (3.42) and (3.43)).

$X(t)$ would represent the bath operator in the interaction picture with an independent bath Hamiltonian. However, for the spin bath there is no such weak coupling expansion, and $X(t)$ appears in the interaction picture with $\omega$, the same operator that provides an effective level splitting for the system. Additionally, the general result for a heteronuclear system including inter-species flip-flops cannot be written in such a compact form.

Previously, it has been shown by Coish and Loss (2004) that a Born-Markov approximation to *second* order in $V_{\rm ff}$ leads to no decay. In contrast, a Born-Markov approximation applied to the effective Hamiltonian leads directly to a result that is *fourth* order in $V_{\rm ff}$ – as can be seen from Eq. (3.42) – describing dynamics that become important at times longer than the second-order result. It is not *a priori* obvious that the effective Hamiltonian, evaluated only to second order in $V_{\rm ff}$, can be used to accurately calculate rates to fourth order in $V_{\rm ff}$. We have, however, verified that all results for the decay rates that we present here are equivalent to a direct calculation expanded to fourth order in $V_{\rm ff}$ at leading order in $A/b \ll 1$ (see Chapter 4).

If the initial nuclear polarization is smooth on the scale of the electron wave function, the matrix elements of operators like $I_k^{\pm} I_k^{\mp}$ can be replaced by average values. Neglecting corrections that are small in $A/Nb \ll 1$, this gives (see also Appendix A.3):

$$C(t) = \langle X(t)X(0)\rangle = \frac{c_+ c_-}{4\omega_n^2} \sum_{k\neq l} A_k^2 A_l^2 e^{-i(A_k - A_l)t}. \tag{3.43}$$

Above, we have introduced the coefficients

$$c_\pm = I(I+1) - \langle\langle m(m\pm 1)\rangle\rangle \tag{3.44}$$

and the double angle bracket indicates an average over $I_k^z$ eigenvalues $m$ (Coish and Loss, 2004).

In the limit $N \gg 1$ we can include the term $k = l$ in Eq. (3.43) and perform the continuum limit $\Sigma_k \to \int dk$ with small corrections. For an isotropic electron wave function of the form

$$\psi(r) = \psi(0) \exp\left\{-\frac{1}{2}\left(\frac{r}{r_0}\right)^q\right\} \tag{3.45}$$

containing $N$ nuclei within radius $r_0$ in $d$ dimensions, the hyperfine coupling constants are distributed according to

$$A_k = A_0 \exp\left\{-\left(\frac{k}{N}\right)^{q/d}\right\}, \tag{3.46}$$

where $k$ is a non-negative index, and we choose $A_0$ to normalize $A_k$ according to $A = \int_0^\infty dk A_k$ (Coish and Loss, 2004) – see also Appendix A.1.

After performing the continuum limit, $C(t)$ will decay, with characteristic time $\tau_c$ given by the inverse bandwidth of nuclear flip-flop excitations $\tau_c \sim 1/A_0 \sim N/A$. For large $b$, $1/T_2$ will be suppressed due to the smallness of $X$ (see Eq. (3.32)), whereas $\tau_c$ remains fixed. At sufficiently large $b$, it will therefore be possible to reach the Markovian regime, where $\tau_c$ is short compared to $T_2$: $\tau_c/T_2 \ll 1$. Evaluating the time integral in Eq. (3.42), we find the general result to leading order in $A/\omega_n$ (see Appendix A.3):

$$\frac{1}{T_2} = \frac{\pi}{4} c_+ c_- f\left(\frac{d}{q}\right)\left(\frac{A}{\omega_n}\right)^2 \frac{A}{N}, \tag{3.47}$$

with

$$f(r) = \frac{1}{r}\left(\frac{1}{3}\right)^{2r-1} \frac{\Gamma(2r-1)}{[\Gamma(r)]^3}, \qquad r > 1/2. \tag{3.48}$$

In Eq. (3.47), $A/N$ sets the scale for the maximum decay rate in the perturbative regime, the coefficients $c_\pm$ set the dependence on the initial nuclear polarization $p$ (e.g., with $I = 1/2$, we have $c_+c_- = (1-p^2)/4$), $A/\omega_n < 1$ gives the small parameter which controls the Born approximation, and $f(d/q)$ is a geometrical factor (plotted in Fig. 3.2). $f(d/q)$ is exponentially suppressed for $d/q > 1$ ($f(r) \propto (1/3)^{2r-1}(1/r)^r$, $r > 1$), but $f(d/q) \to \infty$ for $d/q - 1/2 \to 0^+$. Due to this divergence, no Markov approximation is possible (within the Born approximation) for $d/q \leq 1/2$. We understand the divergence in $f(d/q)$ explicitly from the asymptotic dependence of $C(t)$ at long times:

$$C(t) \propto 1/t^{2d/q}, \qquad t \gg N/A, \qquad d/q < 2. \tag{3.49}$$

Surprisingly, there is a difference of nearly *two orders* of magnitude in $1/T_2$ going from a two-dimensional (2D) quantum dot with Gaussian envelope function ($d = 2$, $q = 2$, $d/q$=1) to a donor impurity with a hydrogen-like exponential wave function ($d = 3$, $q = 1$, $d/q = 3$), if all other parameters are fixed (see Fig. 3.2).

We now specialize to an initial uniform unpolarized spin bath, which is nevertheless narrowed: $\omega\,|n\rangle = b\,|n\rangle$, with equal populations of all nuclear Zeeman levels, i.e., $\langle\langle m\rangle\rangle = 0$ and $\langle\langle m^2\rangle\rangle = \frac{1}{3}I(I+1)$. For a 2D quantum dot with a Gaussian envelope function ($d = q = 2$) we

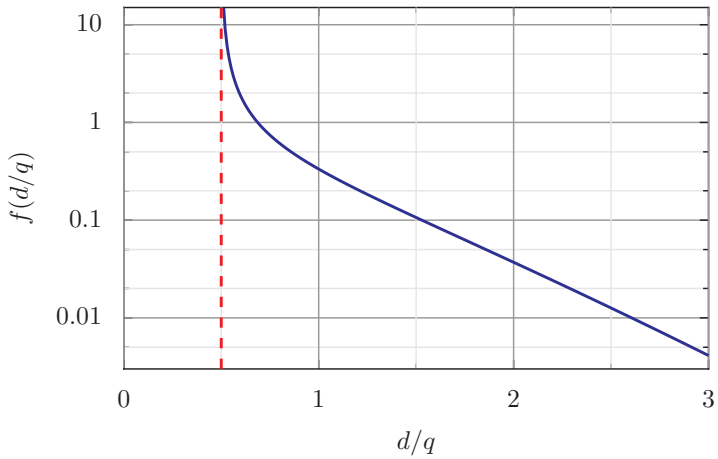


Figure 3.2: Geometrical factor $f(d/q)$ from Eq. (3.48), where $d = 1, 2, 3$ is the dimension and $q$ characterizes the electron envelope function $\psi(r) = \psi(0)\exp\left[-(r/r_0)^q/2\right]$. The dashed line at $d/q = 1/2$ indicates the limit of applicability of the Markov approximation.

find, from Eqs. (3.47) and (3.48):

$$\frac{1}{T_2} = \frac{\pi}{3}\left(\frac{I(I+1)A}{3b}\right)^2 \frac{A}{N}. \tag{3.50}$$

There are two remarkable features of this surprisingly simple result. First, the condition for the validity of the Markov approximation, $T_2 > \tau_c \sim N/A$ will be satisfied whenever $A/b < 1$, which is the same condition that validates a Born approximation. Second, $1/T_2$ has a very strong dependence on the nuclear spin ($1/T_2 \propto I^4$). Thus, systems with large-spin nuclei such as In ($I_{\mathrm{In}} = 9/2$) will show relatively significantly faster decay (see, e.g., Fig. 3.3).

## 3.5 Heteronuclear system

For sufficiently large $b$, i.e. $|\gamma_k - \gamma_{k'}|\, b \gg |A_k - A_{k'}| \sim A/N$, heteronuclear flip-flops between two isotopic species with different $\gamma_k$ are forbidden due to energy conservation. In this case, $1/T_2$ is given in terms of an incoherent sum,

$$\frac{1}{T_2} = \Gamma = \sum_i \Gamma_i, \tag{3.51}$$

where $\Gamma_i$ is the contribution from flip-flops between nuclei of the common species $i$. Assuming a uniform distribution of all isotopes in a 2D quantum dot with a Gaussian envelope function, we find (see also Appendix A.3)

$$\Gamma_i = \frac{1}{T_2^i} = \nu_i^2 \frac{\pi}{3}\left(\frac{I_i(I_i+1)A^i}{3b}\right)^2 \frac{A^i}{N}. \tag{3.52}$$

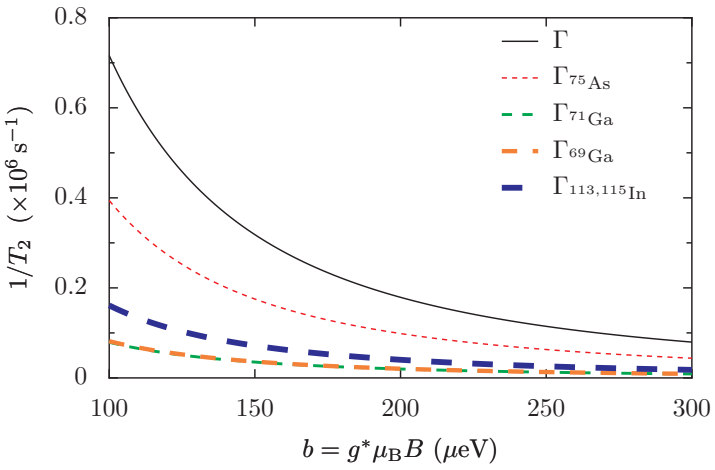


Figure 3.3: Decay rates for an $In_xGa_{1-x}As$ quantum dot with In doping $x = 0.05$. Here, we have assumed $N = 10^5$ and used values of $\nu_i$ and $A^i$ for GaAs from Ref. (Paget et al., 1977): $A^{^{75}\mathrm{As}} = 86\,\mu eV$, $A^{^{69}\mathrm{Ga}} = 74\,\mu eV$, $A^{^{71}\mathrm{Ga}} = 96\,\mu eV$, $\nu_{^{75}\mathrm{As}} = 0.5$, $\nu_{^{69}\mathrm{Ga}} = 0.3(1-x)$, $\nu_{^{71}\mathrm{Ga}} = 0.2(1-x)$. The hyperfine coupling for In in InAs was taken from Liu et al. (2007): $A^{^{113}\mathrm{In}} \approx A^{^{115}\mathrm{In}} \approx A^{\mathrm{In}} = 170\,\mu eV$, $\nu_{\mathrm{In}} = x/2$.

The quadratic dependence on isotopic concentration $\nu_i$ is particularly striking. Due to this dependence, electron spins in GaAs, where Ga has two naturally occurring isotopic species, whereas As has only one, will show a decay predominantly due to flip-flops between As spins. This is in spite of the fact that all isotopes in GaAs have the same nuclear spin and nominally similar hyperfine coupling constants (see Fig. 3.3). Interestingly, we note that the relatively large flip-flop rates for In and As, due to large nuclear spin and isotopic concentration, respectively, may partly explain why only Ga (and not In or As) spins have been seen to contribute to coherent effects in experiments by Ono and Tarucha (2004) on electron transport through (In/Ga)As quantum dots: The same effect may also explain why polarization appears to be transferred more efficiently from electrons to As (rather than Ga) in GaAs quantum dots.

## 3.6 Conclusions

We have shown that a single electron spin can exhibit a purely exponential decay for narrowed nuclear-spin bath initial conditions and in the presence of a sufficiently large electron Zeeman splitting $b$. This work may be important for implementing existing quantum error correction schemes, which typically assume exponential decay of correlation functions due to a Markovian environment. In the limit of large Zeeman splitting $b > A$, where a Born-Markov approximation is valid, we have found explicit analytical expressions for the decoherence time $T_2$, giving explicit dependence's on the electron wave function, magnetic field, bath polarization, nuclear spin, and isotopic abundance for a general nuclear spin bath. Moreover, within the Born-Markov approximation, we have found a divergence in the decoherence rate $1/T_2$ for a one-dimensional quantum dot, indicating a breakdown of the Markov approximation in this case.

Chapter 4

# Electrons in III-V Semiconductors: Direct Approach

## 4.1 Introduction

In the previous chapter, we have seen that, in the absence of refocusing pulses, and at time scales that are short compared to the relevant time scale for the nuclear dipolar interaction, the spin of a confined electron interacting with a narrowed nuclear-spin environment decoheres due to dynamics induced by flip-flop processes between the electron and nuclear spins mediated by the hyperfine interaction. In the presence of a large Zeeman splitting due to an applied magnetic field, direct electron spin-flips are energetically forbidden, giving rise to pure dephasing of the electron spin. Under these conditions, the electron-spin dynamics pass through various stages with a zoo of different decay laws, obtained by various methods (see Fig. 1.1(b)): an exact solution for a fully-polarized nuclear system and leading-order generalized master equation (GME) have both shown a short-time (partial) power-law decay (Khaetskii et al., 2002, 2003; Coish and Loss, 2004), an effective-Hamiltonian and short-time-expansion approach shows that the initial partial decay is followed by a quadratic decay shoulder (Yao et al., 2006; Liu et al., 2007), and a Born-Markov approximation applied to the same effective Hamiltonian – as shown in the previous chapter – shows that the majority of the decay is typically exponential in the high-field (perturbative) regime (Coish et al., 2008; Cywiński et al., 2009a,b). Finally, an equation-of-motion approach has shown a long-time power-law decay to zero (Deng and Hu, 2006, 2008).

In this chapter, we show that each of these results can be obtained in a systematic way from a single unified approach, by extending the generalized master equation (GME) introduced by Coish and Loss (2004) to higher order. In addition to recovering previous results at all time scales, we find important qualitatively new features, including a modulation of the decay envelope (even for a fully isotropic hyperfine interaction). Moreover, we give sub-leading corrections (in the inverse electron Zeeman splitting $1/b$) to the decoherence rate $1/T_2$ calculated in Chapter 3. These corrections suggest an interesting non-monotonic dependence of $1/T_2$ on $b$. Neither the envelope modulations, nor the sub-leading corrections to $1/T_2$ can be

found from dynamics under the effective Hamiltonian alone. The results presented here therefore show limits to the validity of some previous approaches based on high-order expansions of a leading-order effective Hamiltonian, and should be directly compared and contrasted to the results presented in Chapter 3.

## 4.2 Hamiltonian and generalized master equation

We consider the Hamiltonian for a localized electron spin-1/2 (with associated spin operator $\mathbf{S}$), interacting with a bath of nuclear spins $\mathbf{I}_k$ via the Fermi contact hyperfine interaction. We allow generally for a Zeeman splitting $b = g\mu_B B$ of the central spin $\mathbf{S}$ and site- (or species-) dependent Zeeman splitting $b\gamma_k$ in the bath for a nuclear spin $\mathbf{I}_k$ at site $k$. The Hamiltonian for this system is (setting $\hbar = 1$)

$$H = bS^z + b\sum_k \gamma_k I_k^z + \mathbf{S}\cdot\mathbf{h};\quad \mathbf{h} = \sum_k A_k \mathbf{I}_k, \tag{4.1}$$

where the hyperfine coupling constant at site $k$ is given by $A_k = v_0 A^{j_k} |\psi(\mathbf{r}_k)|^2$ if the nucleus at site $k$ is of isotopic species $j_k$ with associated total hyperfine coupling constant $A^{j_k}$, $\psi(\mathbf{r}_k)$ is the electron envelope wavefunction, evaluated at site $\mathbf{r}_k$ (the position of the $k^{\text{th}}$ nuclear spin), and $v_0$ is the atomic volume.

In Eq. (4.1) we have neglected the nuclear dipole-dipole interaction, which can give rise to additional internal dynamics in the nuclear spin system, and consequent decay of the electron spin (Klauder and Anderson, 1962; de Sousa and Das Sarma, 2003; Witzel and Sarma, 2006; Yao et al., 2006; Cywiński et al., 2009a). Dipole-dipole-induced nuclear spin dynamics are highly suppressed in the presence of an inhomogeneous quadrupolar splitting [1] (Maletinsky et al., 2009), or Knight-field gradient in a small quantum dot (the "frozen-core" or diffusion-barrier effect, see Ramanathan (2008) for a review). The relevant decoherence rate due purely to the hyperfine interaction is enhanced for a small dot ($1/T_2 \sim 1/N$ for a quantum dot containing $N$ nuclear spins), whereas the dipole-dipole-induced nuclear dynamics are suppressed for a small dot due to the frozen-core effect. Thus, there will always be some dot size $N$ where the nuclear dipolar interactions can be neglected, even up to times that are long compared to the electron-spin decoherence time.

[1] Hyperfine-induced long-range nuclear pair flips have a bandwidth of $\sim A/N$ for large electron Zeeman splitting $b > A$, whereas the short-range nuclear dipolar interactions induce excitations with a narrow bandwidth $\sim \delta A_{\text{nn}}$, where $\delta A_{\text{nn}}$ is the typical difference in nearest-neighbor hyperfine coupling constants. In the presence of a nonuniform gradient in the Zeeman energy or secular ($I_k^z$-preserving) quadrupolar splitting, we expect hyperfine-mediated pair flips to be allowed, while dipolar pair flips are suppressed, at least in the regime where $A/N \gtrsim \Delta E_{\max}$ and $\Delta E_{\text{nn}} > \delta A_{\text{nn}} \sim (1/N)^{1/d} A/N$, where $d$ is the dimensionality of the dot, $\Delta E_{\text{nn}}$ is the typical difference in the quadrupolar splitting or Zeeman energy between neighboring nuclei and $\Delta E_{\max}$ is the maximum difference in quadrupolar splitting or Zeeman energy between any two nuclei in the dot. The inequalities will be satisfied for a range of $\Delta E_{\text{nn}}$ and $\Delta E_{\max}$ whenever the gradient in quadrupolar or Zeeman energy is nonuniform on the scale of the dot. This will be true, e.g., for local disorder due to random doping of In atoms in a $\text{In}_x\text{Ga}_{1-x}\text{As}$ quantum dot. For a uniform gradient, we estimate $\Delta E_{\max} \sim N^{1/d}\Delta E_{\text{nn}}$, which saturates the bounds. While this estimate demonstrates the existence of such a regime, a more complete calculation taking both hyperfine interaction and nuclear dipolar interactions fully into account would be required to establish the complete range of validity.

### 4.2.1 Initial conditions

We choose product-state initial conditions

$$\rho(0) = \rho_S(0) \otimes \rho_I(0), \tag{4.2}$$

where $\rho_{I(S)} = \mathrm{tr}_{S(I)}\rho$ is the reduced density matrix for the nuclear (electron) system. Such an initial state can be prepared through fast strong pulses applied to the electron spin or by allowing an electron to tunnel rapidly into a localized orbital (Coish and Loss, 2004).

Typically, nothing will be known about the nuclear-spin system at the beginning of an experiment, and the density matrix $\rho_I(0)$ will be well-characterized by a completely random (infinite temperature) mixture. Randomized initial conditions for the nuclear-spin bath result in a rapid Gaussian decay of the transverse electron spin in the presence of a strong Zeeman splitting $b$ (Khaetskii et al., 2002; Merkulov et al., 2002; Schliemann et al., 2002, 2003; Coish and Loss, 2004; Petta et al., 2005). This rapid decay, due to static fluctuations in the initial conditions, can be removed by performing a measurement of the $z$-component of the slowly-varying nuclear field $h^z$ (Coish and Loss, 2004). There have been several theoretical proposals (Stepanenko et al., 2006; Klauser et al., 2006; Giedke et al., 2006) to measure the nuclear-spin system into an eigenstate of $h^z$ and there are now several experiments where similar state preparation has been achieved through dynamical pumping (Greilich et al., 2007; Reilly et al., 2008; Greilich et al., 2009; Vink et al., 2009; Latta et al., 2009; Xu et al., 2009). After preparing the nuclei in an eigenstate of the operator $h^z$, the nuclear system will be described most generally by an arbitrary mixture of $g$ degenerate $h^z$-eigenstates $|n_i\rangle$ $(i = 1, 2, \ldots, g)$:

$$\rho_I(0) = \sum_i \rho_{ii} |n_i\rangle \langle n_i| + \sum_{i \neq j} \rho_{ij} |n_i\rangle \langle n_j| , \tag{4.3}$$

where

$$h^z |n_i\rangle = h^z_n |n_i\rangle \quad \forall i. \tag{4.4}$$

In this paper, we will assume that there is no 'special' phase relationship between the different $h^z$-eigenstates, which allows us to approximate $\rho_I(0)$ by the diagonal part of Eq. (4.3)

$$\rho_I(0) \approx \sum_i \rho_{ii} |n_i\rangle \langle n_i| , \tag{4.5}$$

where, for any particular $i$, the state $|n_i\rangle$ is given by a product of $I^z_k$-eigenstates:

$$|n_i\rangle = \bigotimes_{j,k_j} \left| I_j m^i_{k_j} \right\rangle \tag{4.6}$$

with spin operator $I^z_{k_j}$ associated with the nuclear spin of isotopic species $j$ at site $k_j$: $I^z_{k_j} \left| I_j m_{k_j} \right\rangle = m^i_{k_j} \left| I_j m_{k_j} \right\rangle$, and where $I_j \leq m^i_{k_j} \leq I_j$.

We will find it convenient to define the average of an arbitrary function of $I^z$-eigenvalues $f^j(m)$ for the subset of nuclear spins of species $j$ by:

$$\left\langle \left\langle f^j(m) \right\rangle \right\rangle \equiv \sum_i \rho_{ii} \langle n_i| f^j(I^z_{k_j}) |n_i\rangle , \tag{4.7}$$

where we assume a uniformly polarized nuclear-spin system throughout this article, making the average on the right-hand side independent of $k_j$. Specifically, this condition will be satisfied whenever a sufficiently large number $g \gg 1$ of degenerate $h^z$-eigenstates contribute to the average so that $\sum_i \rho_{ii}$ can be replaced by the same probability distribution $\sum_m P_j(m)$ for all sites $k_j$ (see also Appendix B of Coish and Loss (2004)):

$$\sum_i \rho_{ii} \langle n_i | f^j(I^z_{k_j}) | n_i \rangle = \sum_{m=-I_j}^{I_j} P_j(m) f^j(m). \tag{4.8}$$

### 4.2.2 Generalized master equation

In this section we derive an exact equation of motion for the transverse components of the electron spin alone, taking the dynamics of the coupled electron-nuclear spin system into account (see also Chapter 2.1). Our starting point is the von Neumann equation for the full density matrix $\dot{\rho} = -i[H, \rho] = -i\mathsf{L}\rho$. To find the reduced dynamics of the electron spin alone, we rewrite the von Neumann equation in the form of the Nakajima-Zwanzig generalized master equation (Fick and Sauermann, 1990; Breuer and Petruccione, 2002). Introducing a projection superoperator $\mathsf{P}$ that preserves the initial condition $\mathsf{P}\rho(0) = \rho(0)$, the Nakajima-Zwanzig generalized master equation can be written as

$$\mathsf{P}\dot{\rho}(t) = -i\mathsf{PLP}\rho(t) - i\int_0^t dt' \Sigma(t-t')\mathsf{P}\rho(t'), \tag{4.9}$$

$$\Sigma(t) = -i\mathsf{PLQ}e^{-i\mathsf{LQ}t}\mathsf{QLP}. \tag{4.10}$$

Additionally, the projector $\mathsf{P}$ must satisfy $\mathsf{P}^2 = \mathsf{P}$ and is typically chosen to preserve all system variables $S^\alpha$: $\mathrm{tr} S^\alpha \rho(t) = \mathrm{tr} S^\alpha \mathsf{P}\rho(t)$. Here, $\mathsf{Q}$ is the complement projector: $\mathsf{Q} = \mathsf{1} - \mathsf{P}$. For the special case of the Hamiltonian (4.1) and the initial condition (4.5), we choose the projection superoperator $\mathsf{P} = \rho_I(0)\mathrm{tr}_I$ and find that the exact equation of motion for the transverse electron spin ($S_\pm = S^x \pm iS^y$) is of the form (Coish and Loss, 2004)

$$\frac{d}{dt}\langle S_+ \rangle_t = i\omega_n \langle S_+ \rangle_t - i\int_0^t dt' \Sigma(t-t') \langle S_+ \rangle_{t'}, \tag{4.11}$$

$$\Sigma(t) = \mathrm{tr}\left[S_+ \Sigma(t) S_- \rho_I(0)\right], \tag{4.12}$$

where $\omega_n = b + h^z_n$.

### 4.2.3 Rotating frame

We define the coherence factor $x_t$, which measures the transverse components of the electron spin in a frame co-rotating with the spin at frequency $\omega_n + \Delta\omega$ through

$$x_t = 2e^{-i(\omega_n + \Delta\omega)t} \langle S_+ \rangle_t, \tag{4.13}$$

and the associated self-energy

$$\tilde{\Sigma}(t) = e^{-i(\omega_n + \Delta\omega)t}\Sigma(t), \tag{4.14}$$

with Lamb shift $\Delta\omega$ due to virtual excitations of the bath:

$$\Delta\omega = -\mathrm{Re}\int_0^\infty dt\tilde{\Sigma}(t). \tag{4.15}$$

This gives an equation of motion for $x_t$:

$$\dot{x}_t = -i\Delta\omega x_t - i\int_0^t dt'\tilde{\Sigma}(t-t')x_{t'}. \tag{4.16}$$

Eq. (4.16) is an exact equation of motion for the coherence factor $x_t$, and therefore serves as an important starting point for systematic approximations in the rest of this article.

## 4.3 Self-energy expansion

In the absence of an exact closed-form expression for $\tilde{\Sigma}(t)$, we must resort to an approximation scheme. For a large electron-spin Zeeman splitting $b$, and due to the large difference between the magnetic moments of electron and nuclear spin ($\gamma_k \sim 10^{-3}$), it is appropriate to separate the Hamiltonian (4.1) into an unperturbed piece that preserves $S^z$ and a flip-flop term, which induces energy non-conserving flip-flops between electron and nuclear spins: $H = H_0 + V_{\mathrm{ff}}$, where

$$H_0 = \omega S^z + b\sum_k \gamma_k I_k^z, \quad \omega = b + h^z, \tag{4.17}$$

$$V_{\mathrm{ff}} = \frac{1}{2}\left(h^+ S_- + h^- S_+\right). \tag{4.18}$$

We can then write $\tilde{\Sigma}(t)$ in powers of $V_{\mathrm{ff}}$ by performing a Dyson-series expansion (see Eq. (2.14)) of Eq. (4.10) and inserting the result into the definition (4.12) (Coish and Loss, 2004):

$$\tilde{\Sigma}(t) = \tilde{\Sigma}^{(2)}(t) + \tilde{\Sigma}^{(4)}(t) + O\left(V_{\mathrm{ff}}^6\right). \tag{4.19}$$

Progressively higher-order terms in the expansion involve a larger number of flip-flops between the electron and nuclear bath spins. Consequently, higher-order terms are suppressed by the energy cost for such flip-flops, provided by the electron spin splitting $b$ for an unpolarized nuclear bath. In particular, up to factors of order unity and an overall common prefactor, the size of the $2(n+1)^{\mathrm{th}}$-order term is given by (see also Appendix A of Coish and Loss (2004)):

$$\tilde{\Sigma}^{(2[n+1])}(t) \propto \left(\frac{I(I+1)A}{b}\right)^n. \tag{4.20}$$

For a nuclear spin of order unity ($I \sim 1$), the condition for the validity of a perturbative expansion in terms of $V_{\mathrm{ff}}$, i.e., the condition for convergence of the series in Eq. (4.19), is then given approximately by (Coish and Loss, 2004; Deng and Hu, 2006; Coish et al., 2008)

$$b \gtrsim A, \tag{4.21}$$

which is the same condition as for the Born-Markov approximation in Chapter 3.

In the Born approximation, the self-energy $\tilde{\Sigma}(t)$ is replaced by the leading-order non-vanishing term in the expansion of Eq. (4.19): $\tilde{\Sigma}(t) \approx \tilde{\Sigma}^{(2)}(t)$. To understand the evolution of $x_t$ within the Born approximation, it is convenient to introduce the function $\psi(t) = \int_t^\infty dt' \tilde{\Sigma}^{(2)}(t')$, which allows us to rewrite the equation of motion (4.16) as (Fick and Sauermann, 1990)

$$\dot{x}_t = -i(\psi(0) + \Delta\omega)x_t + \frac{d}{dt}R(t), \tag{4.22}$$

where $R(t) = i\int_0^t dt' \psi(t-t')x_{t'}$. In a standard Born-Markov approximation, the dynamics induced by $R(t)$ are neglected. The real part of $\psi(0)$ cancels any remaining precession: $-\mathrm{Re}\psi(0) = \Delta\omega$ (see Eq. (4.15)) and the imaginary part of $\psi(0)$ gives rise to a purely exponential decay of $x_t$ with decay rate $\Gamma = -\mathrm{Im}\psi(0)$. It has been shown by Coish and Loss (2004) that the decay rate for this system within a Born-Markov approximation vanishes: $\Gamma = 0$. Within a Born approximation, all non-trivial dynamics in the rotating frame are therefore induced by the non-Markovian remainder term $R(t)$. The remainder term $R(t)$ has been investigated in detail by Khaetskii et al. (2002, 2003) and Coish and Loss (2004) and leads to a partial decay of the coherence factor of order $|R(t)| \sim O\left[\frac{1}{N}\left(\frac{A}{b}\right)^2\right]$ on a time scale $\sim N/A$, with long-time power-law tails (Coish and Loss, 2004). In the rest of this chapter, we include the effects of the Born approximation in inducing the Lamb shift (4.15), but neglect the $\lesssim O(1/N)$ corrections due to $R(t)$ in the perturbative regime. Additionally, we will go beyond the Born approximation by including the fourth-order correction to the self-energy in the expansion of Eq. (4.19), which we show induces a more dramatic decay, albeit at a longer time scale.

We now approximate the self-energy by including all terms at second and fourth order in electron-nuclear spin flip-flops

$$\tilde{\Sigma}(t) \approx \tilde{\Sigma}^{(2)}(t) + \tilde{\Sigma}^{(4)}(t). \tag{4.23}$$

Inserting (4.23) into (4.16) we find, neglecting the dynamics with amplitude suppressed by $\sim 1/N$ in the perturbative regime due to $R(t)$:

$$\dot{x}_t = -i\int_0^t dt' \tilde{\Sigma}^{(4)}(t-t')x_{t'}, \tag{4.24}$$

$$\Delta\omega \approx -\mathrm{Re}\int_0^\infty dt \tilde{\Sigma}^{(2)}(t). \tag{4.25}$$

The integro-differential equation (4.24) is difficult to solve, in general. However, in terms of Laplace-transformed variables, this equation becomes an algebraic equation, which can be solved directly. Introducing the Laplace transform of some function $f(t)$,

$$f(s) = \int_0^\infty dt\, e^{-st} f(t), \quad \mathrm{Re}(s) > 0, \tag{4.26}$$

we rewrite Eqs. (4.24) and (4.25) as

$$x(s) = \frac{x_0}{s + i\tilde{\Sigma}^{(4)}(s)}, \tag{4.27}$$

$$\Delta\omega \approx -\mathrm{Re}\tilde{\Sigma}^{(2)}(s = 0^+). \tag{4.28}$$

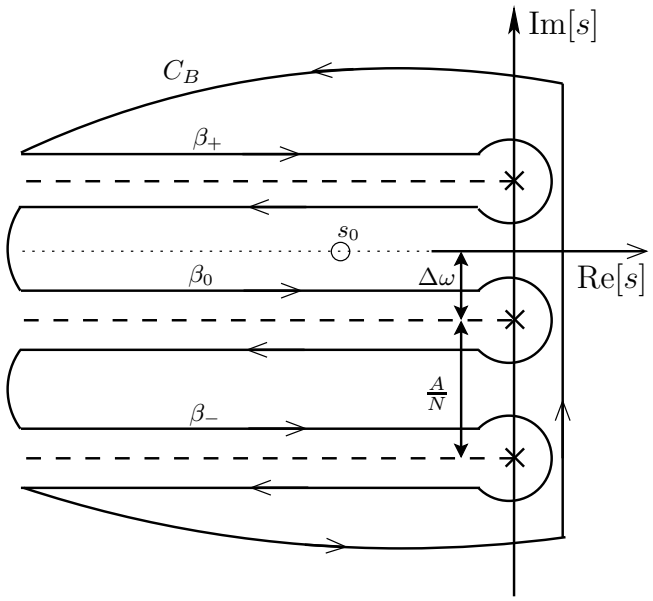


Figure 4.1: Contour used to evaluate the Bromwich inversion integral (in the rotating frame defined by Eq. (4.13)). The dynamics of the coherence factor $x_t$ are determined by a single pole at $s_0 = -1/T_2$ and three branch cuts (see main text). The pole is offset from the branch cuts by the Lamb shift $\Delta\omega$ and the excitation bandwidth (separation between branch points) is given by the size of the hyperfine coupling to a single nucleus at the center of the quantum dot, $A/N$.

Here, the initial value of the coherence factor is denoted by $x_0 = x_t|_{t=0}$. We have calculated the self-energy $\tilde{\Sigma}$ in Appendix A.4, including terms up to fourth order in $V_{\mathrm{ff}}$.

The dominant contributions to $\tilde{\Sigma}(s)$ occur for $|s| \ll |\omega_n|$ in the rotating frame (high-frequency, $s \simeq i\omega_n$ in the lab frame). We have expanded the second- and fourth-order self-energies in this limit, as described in Appendix A.4. Corrections to this expansion are smaller than the retained contributions by a factor of $A/N\omega_n \ll 1$. For explicit calculation, it is useful to specialize to the case of a homonuclear system (where $\gamma_k = \gamma$ for all $k$) and a two-dimensional quantum dot with Gaussian envelope function, leading to coupling constants (Coish and Loss, 2004; Coish et al., 2008) $A_k = (A/N)e^{-k/N}$. Performing the continuum limit ($\sum_k \to \int dk$) and evaluating the relevant energy integrals for a uniformly polarized nuclear spin system leads to

$$\tilde{\Sigma}^{(4)}(s - i\Delta\omega) = i\alpha\left[F_+(s)J_+(s) + F_-(s)J_-(s) - s\right], \tag{4.29}$$

$$\Delta\omega \simeq -\tilde{\Sigma}^{(2)}(s = 0^+) = \frac{1}{8}(c_+ + c_-)\frac{A}{\omega_n}\frac{A}{N}, \tag{4.30}$$

with

$$\alpha = \frac{c_+ c_-}{24}\left(\frac{A}{\omega_n}\right)^2, \tag{4.31}$$

and where $c_\pm = I(I+1) - \langle\langle m(m \pm 1)\rangle\rangle$ are the coefficients introduced by Coish and Loss (2004) with $\langle\langle \cdots \rangle\rangle$ indicating an average over the mixture of $I_k^z$-eigenvalues, described by Eq.

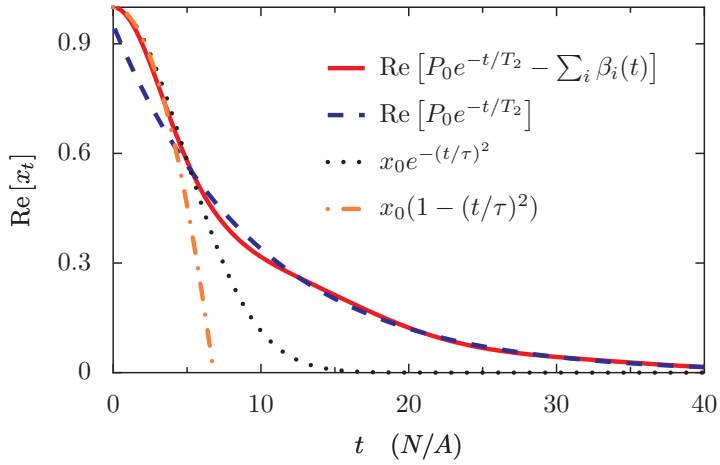


Figure 4.2: Comparison of the contribution from the pole at $s_0$ in Fig. 4.1 with exponentially decaying residue (blue dashed line) with the full fourth-order result, obtained numerically (red solid line). For comparison, the re-exponentiated short-time quadratic decay is also shown (black dotted line) with a parabolic decay having the same time scale (orange dash-dotted line). We take the initial condition $x_0 = 1$, assume an unpolarized nuclear spin system [with $\omega_n = b$, $c_\pm = \frac{2}{3}I(I+1)$, which follows from $\langle\langle m^2 \rangle\rangle = I(I+1)/3$ if all Zeeman levels have equal population], and have chosen $I = 3/2$ and $A/b = 1/3$.

(4.7). Additionally, we have introduced the functions

$$F_\pm(s) = \left(\frac{N}{A}\right)^2 \left(s \pm i\frac{A}{N}\right)^2 \left(s \mp 2i\frac{A}{N}\right), \tag{4.32}$$

$$J_\pm(s) = \log\left(s \pm i\frac{A}{N}\right) - \log(s). \tag{4.33}$$

After inserting (6.18) into (4.27), we find that the Laplace-transformed coherence factor has three branch points, and if the principle branch is chosen for all branch cuts and at large electron Zeeman splitting ($b \gg A$), there is one pole at $s = s_0$ (see Fig. 4.1). These non-analytic features determine the dynamics of the coherence factor (see below). The equation-of-motion method adopted by Deng and Hu (2006, 2008) bears some similarity to the current approach. However, the excitation bandwidth (distance between branch points) found by Deng and Hu (2006, 2008) is half that found here ($A/2N$ rather than $A/N$), leading to a difference (by a factor of 2) for relevant decay time scales. We comment on other differences, below.

## 4.4 Spin dynamics

We find the time-dependent coherence factor by evaluating the Bromwich inversion integral

$$x_t = \lim_{\gamma \to 0^+} \frac{1}{2\pi i} \int_{\gamma - i\infty}^{\gamma + i\infty} ds e^{st} x(s), \tag{4.34}$$

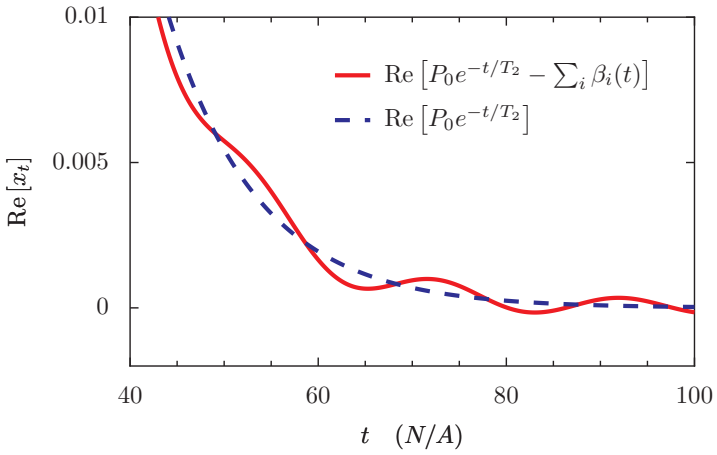


Figure 4.3: Long-time decay. At long times, the exponential decay envelope is modulated by branch-cut contributions at a frequency given by the Lamb shift $\Delta\omega$. Parameters are as in Fig. 4.2.

which can be rewritten in terms of an integral over the closed contour $C_B$ and branch-cut integrals $\beta_j$, $j = 0, +, -$ (see Fig. 4.1):

$$\begin{aligned} x_t &= \frac{1}{2\pi i}\oint_{C_B} ds e^{st} x(s) - \sum_j \beta_j(t) \\ &= \mathrm{Res}\left[e^{st}x(s), s = s_0\right] - \sum_j \beta_j(t). \end{aligned} \tag{4.35}$$

In Eq. (4.35), we have applied the residue theorem to write the integral over $C_B$ in terms of a residue at the pole $s_0$.

Since the rotating frame is chosen to give $s_0 = -1/T_2$ purely real, we find the general result

$$x_t = P_0 e^{-t/T_2} - \sum_i \beta_i(t), \tag{4.36}$$

with $P_0$ given by Eq. (4.46), below. The coherence factor is characterized by two terms: an exponential, which dominates in the perturbative regime ($A \lesssim b$, see Fig. 4.2), and a sum of branch-cut integrals, which give rise to modulations of the decay envelope and a dominant long-time power-law decay (see Fig. 4.3).

### 4.4.1 Envelope modulations and long-time decay

From direct asymptotic analysis of the branch-cut integrals, we find $\beta_\pm(t) \propto 1/t^3$, while $\beta_0(t) \propto 1/t^2$ at long times. Since the pole contribution decays exponentially, the leading long-time asymptotics of $x_t$ are thus given by $\beta_0(t)$. Evaluating the prefactor, we find the long-time limit (valid for $t \gg \max\left[1/\Delta\omega, (6\alpha/\Delta\omega)\ln|N\Delta\omega/6\alpha A|\right]$):

$$\beta_0(t) \sim -\frac{6\alpha x_0}{(2\pi\alpha A/N - i\Delta\omega)^2}\frac{e^{-i\Delta\omega t}}{t^2}, \tag{4.37}$$

which gives the long-time behavior of the coherence factor with initial condition $x_0 = 1$ (see Fig. 4.4):

$$\mathrm{Re}[x_t] \sim \frac{C\cos(\Delta\omega t + \phi)}{t^2}, \tag{4.38}$$

where

$$C = \frac{6\alpha}{(2\pi\alpha A/N)^2 + \Delta\omega^2}, \tag{4.39}$$

$$\phi = -2\arctan\left(\frac{\Delta\omega N}{2\pi\alpha A}\right). \tag{4.40}$$

The modulations at a frequency $\Delta\omega$ in Eq. (4.38) can be understood on physical grounds in the following way: The short-time dynamics of the electron spin are controlled by nuclear spins near the center of the dot, which are coupled most strongly. The effective precession frequency of the electron spin is therefore renormalized by the shift $\Delta\omega$ due to virtual flip-flop processes with nuclei near the center for most of the decay envelope. The long-time decay, however, is controlled by weakly-coupled nuclei far from the center of the dot, which cannot strongly shift the electron-spin precession frequency. The long-time dynamics therefore occur at the 'bare' precession frequency $\omega_n$. The difference in frequency between the dominant (short-time) and sub-dominant (long-time) behavior leads to a relative beating at the frequency difference $\Delta\omega$. We note that the physical origin of this envelope modulation is completely different from the more typical case of electron spin-echo envelope modulation (ESEEM), which is often observed in systems with an anisotropic hyperfine interaction (Rowan et al., 1965; Mims, 1972; Childress et al., 2006; Witzel et al., 2007). The modulations described here occur even in the present case of a purely isotropic interaction and without spin echoes. The two cases can be experimentally distinguished through a difference in the magnetic-field dependence of the modulation frequency. Finally, we note that the modulations found here are reminiscent of modulations in branch-cut contributions that have been highlighted previously for the spin-boson model (DiVincenzo and Loss, 2005).

Another striking feature of Eq. (4.38) is the long-time power-law tail. This differs from the long-time exponential decay found by Liu et al. (2007) and Cywiński et al. (2009a,b) using re-summation and re-exponentiation techniques. The same long-time power-law decay ($\propto 1/t^2$) has previously been predicted by Deng and Hu (2006, 2008) based on an equation-of-motion method, but without mention of the phase shift or envelope modulations predicted by Eq. (4.38). To compare the results given here directly with those of Deng and Hu (2006, 2008), we consider the case of $I = 1/2$ with an unpolarized nuclear-spin bath. This gives

$$C = \frac{4}{(A/N)^2}\left(1 + \mathcal{O}\left[\left(\frac{A}{b}\right)^2\right]\right), \tag{4.41}$$

$$\phi = -\pi + \mathcal{O}\left[\left(\frac{A}{b}\right)^3\right]. \tag{4.42}$$

Although the power law found here matches that reported by Deng and Hu (2006, 2008), and the modulations or phase shift can be ignored in the limit $A/b \ll 1$, the prefactor $C$ (which

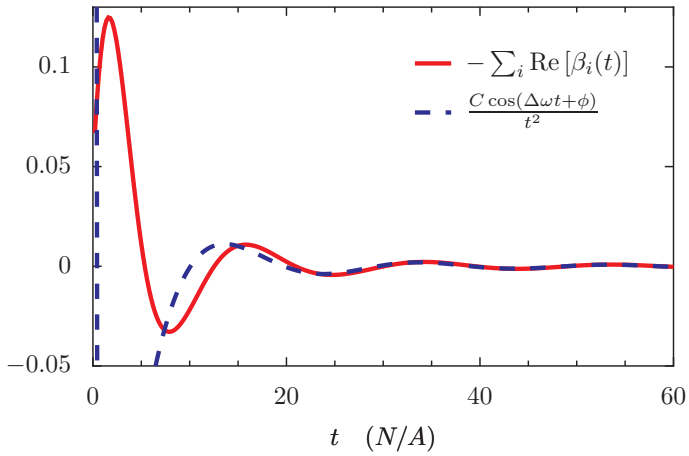


Figure 4.4: Comparison of the full numerical branch-cut integral $-\sum_i \mathrm{Re}\left[\beta_i(t)\right]$ with the long-time asymptotic expression given by Eq. (4.38). Parameters are as in Fig. 4.2.

is[2] $C = \mathcal{O}\left[(b/A)^2\right]$ in the work of Deng and Hu (2006, 2008)) is qualitatively different. In particular, here we find that the power-law contribution with modulations can have substantial weight (of order unity) in the perturbative regime $A \lesssim b$. This is clear from Fig. 4.4, where we show that the branch-cut contributions can contribute approximately 10% of the total decay amplitude.

### 4.4.2 Decay shoulder

For small $t$, we perform a Taylor-series expansion of $x_t$:

$$x_t = x_t|_{t\to 0^+} + \dot{x}_t|_{t\to 0^+} t + \frac{1}{2}\,\ddot{x}_t|_{t\to 0^+} t^2 + \ldots . \tag{4.43}$$

From Eq. (4.24) and the initial value theorem we find $\dot{x}_t|_{t\to 0^+} = 0$ and $\ddot{x}_t|_{t\to 0^+} = -i\tilde{\Sigma}^{(4)}(t = 0) = -i \lim_{s\to\infty} s\tilde{\Sigma}^{(4)}(s)$. Inserting Eq. (A.53) for $\tilde{\Sigma}^{(4)}(s)$ and choosing $x_0 = 1$ gives:

$$x_t \simeq 1 - \frac{t^2}{\tau^2}, \quad \tau \simeq \sqrt{\frac{2\omega_n^2}{c_+ c_- \left(\sum_k A_k^2\right)^2}}. \tag{4.44}$$

Eq. (4.44) gives the same short-time decay reported by Liu et al. (2007), which was taken to describe a Gaussian coherence decay: $x_t \simeq x_0 \exp\left[-(t/T_{2,A})^2\right]$. Here we note that the Gaussian approximation is only valid for times less than the actual decay time ($t \ll \tau$) in the perturbative regime ($b \gtrsim A$) since the dominant decay is exponential in this regime for a typical (two-dimensional parabolic) quantum dot, as we have shown in Chapter 3 and illustrated here in Fig. 4.2. Re-exponentiation also fails for the fourth-order solution at lower magnetic field, as we show in Sec. 4.5, below.

[2] $A/b$ in our notation is equivalent to $N/\Omega$ in the dimensionless units of Deng and Hu (2006, 2008).

For a uniform unpolarized nuclear spin system, and for an electron with Gaussian envelope function in two dimensions, we find

$$\tau \simeq \frac{6\sqrt{2}}{I(I+1)} \left(\frac{b}{A}\right) \left(\frac{N}{A}\right). \tag{4.45}$$

We compare the initial decay found using this formula with the full non-Markovian solution in Fig. 4.2. While the short-time decay shoulder is well-described by a Gaussian, the full decay envelope is much better described by the dominant exponential solution. At larger Zeeman splitting $b$, the distinction between Gaussian and exponential becomes significantly more pronounced.

### 4.4.3 Exponential decay

We evaluate the residue at the pole $s_0$ in Fig. 4.1, giving

$$P_0 = \frac{1}{1 + i\, \frac{d}{ds}\tilde{\Sigma}^{(4)}(s)\Big|_{s=-1/T_2}}. \tag{4.46}$$

For a two-dimensional parabolic quantum dot, with an unpolarized nuclear system, we find $P_0 = 1 + \mathcal{O}\left(\left[\frac{A}{b}\right]^2 \ln\left[\frac{A}{b}\right]\right)$. Thus, when $A < b$, a Markov approximation is justified (resulting in a dominant exponential decay), in agreement with the results presented in Chapter 3.

In the Markovian regime, the decay rate for the exponentially decaying pole can be determined through (Coish et al., 2008) $1/T_2 = -\mathrm{Im}\tilde{\Sigma}^{(4)}(0^+)$. From the self-energy given in Eq. (A.53) of Appendix A.4, this gives

$$\frac{1}{T_2} = \frac{\pi c_+ c_-}{4\omega_n^2} \sum_{k,k'} A_k^2 A_{k'}^2 \delta(A_k - A_{k'} - \Delta\omega). \tag{4.47}$$

We note that the decoherence rate vanishes in the limit of full polarization $p \to 1$ since $1/T_2 \propto c_+ c_-$ and, e.g., $c_+ c_- \propto (1 - p^2)$ for $I = 1/2$. This is consistent with the exact solution in this limit given by Khaetskii et al. (2002).

The Markovian decay rate (4.47) depends on the density of states for pair flips at an energy determined by the Lamb shift $\Delta\omega \propto A/\omega_n$. The presence of $\Delta\omega$ in the energy-conservation condition can be understood physically as arising from the rapid initialization that we assumed, giving rise to the product-state initial condition (4.2). At the instant the flip-flop interaction $V_{\mathrm{ff}}$ is 'turned on', the electron spin experiences only the bare precession frequency $\omega_n$. However, after an interaction time scale $t \sim 1/\omega_n$ (see Appendix A.6), the renormalized precession frequency $\omega_n + \Delta\omega$ gives the electron energy splitting, and so the correct energy-conservation condition for nuclear-spin pair flips contains the difference of these two quantities (i.e., $\Delta\omega$). The dependence on $\Delta\omega$ shown in Eq. (4.47) results in an interesting (in general, non-monotonic) dependence of $1/T_2$ on magnetic field [3]. In contrast, the effective-Hamiltonian approach that

[3] This non-monotonic dependence of $1/T_2$ on the electron-spin splitting is reminiscent of a similar effect found in the spin-boson model. There, a non-monotonic dependence of the decoherence rate as a function of energy splitting is found when properly accounting for renormalization factors (DiVincenzo and Loss, 2005).

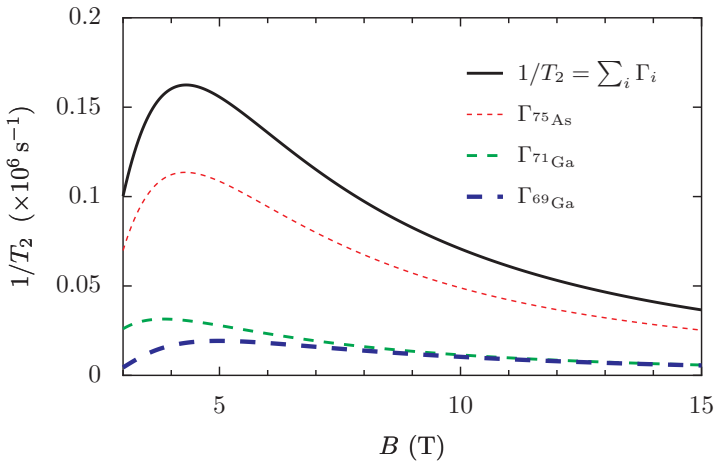


Figure 4.5: Decoherence rates $\Gamma_i$ from Eq. (4.50) and total decoherence rate $1/T_2 = \sum_i \Gamma_i$ for an electron spin in a GaAs quantum dot containing $N = 10^5$ nuclei with $g$-factor $|g| = 0.4$. The decoherence rate shows a non-monotonic behavior, reaching a pronounced maximum. This is in contrast to the leading-order result developed in Chapter 3 and in contrast to the results from other higher-order expansions (Cywiński et al., 2009b). We have used hyperfine coupling constants $A^{^{69}Ga} = 74\,\mu e\mathrm{V}$, $A^{^{71}Ga} = 96\,\mu e\mathrm{V}$, $A^{^{75}As} = 86\,\mu e\mathrm{V}$ and relative abundances $\nu_{^{69}Ga} = 0.3$, $\nu_{^{71}Ga} = 0.2$, $\nu_{^{75}As} = 0.5$, which have been estimated by Paget et al. (1977) (see also Table 1 of Coish and Baugh (2009)).

was adopted in Chapter 3 and by Yao et al. (2006), Liu et al. (2007), and Cywiński et al. (2009a,b) incorporates the leading-order frequency shift as an additive constant directly into the electron-spin Zeeman splitting, and so it does not enter into the formula for $1/T_2$. The Lamb shift that comes out of the same procedure used here, but starting from the effective Hamiltonian, has a higher-order dependence $\Delta\omega \propto (A/\omega_n)^2$ (see the discussion following Eq. (A.25)), so the effective-Hamiltonian treatment does not recover the correct magnetic-field dependence given by Eq. (4.47), although the leading-order $\Delta\omega \simeq 0$ behavior is recovered correctly. This is not surprising, since the effective Hamiltonian is only strictly valid to leading order in $A/\omega_n$. Through explicit calculation at higher orders, we have checked that the leading correction to the Markovian decay rate at sixth order in $V_{\mathrm{ff}}$ is $\mathcal{O}\left[(A/\omega_n)^4\right]$ (see Appendix A.5), and so the expression given here is at least correct up to and including terms of order $\mathcal{O}\left[(A/\omega_n)^3\right]$.

Specializing to a two-dimensional quantum dot with Gaussian envelope function and evaluating the energy integrals in the continuum limit gives

$$\frac{1}{T_2} = \frac{8\pi c_+ c_-}{3(c_+ + c_-)^2}\frac{A}{N}(\epsilon^5 - 3\epsilon^3 + 2\epsilon^2)\Theta(1-\epsilon), \tag{4.48}$$

where

$$\epsilon = \frac{c_+ + c_-}{8}\left|\frac{A}{\omega_n}\right|. \tag{4.49}$$

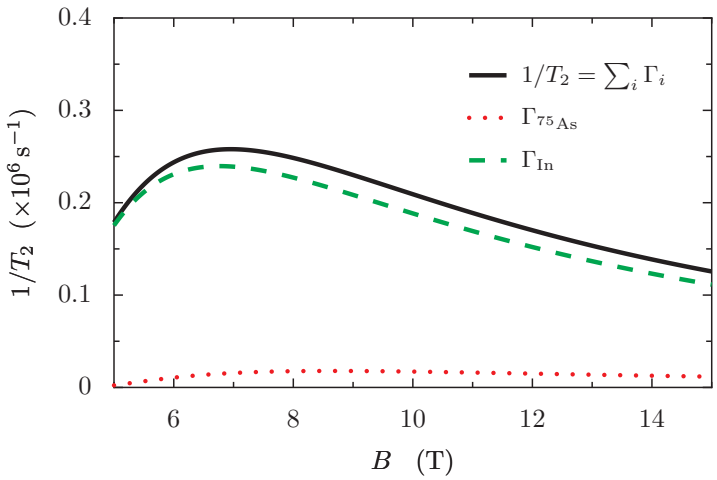


Figure 4.6: Total decoherence rate $1/T_2 = \sum_i \Gamma_i$ (solid line) with $\Gamma_i$ from Eq. (4.50) for an electron spin in a $In_xGa_{1-x}As$ quantum dot containing $N = 10^5$ nuclei with $g$-factor $|g| = 0.5$ and In doping $x = 0.3$. We show individual contributions from $\Gamma_{^{75}\mathrm{As}}$ (dotted) and $\Gamma_{\mathrm{In}}$ (dashed). Contributions from the gallium isotopes are not visible on this scale. For this plot, we have taken hyperfine coupling constants for the gallium and arsenic isotopes as in Fig. 4.5 and have used $A^{^{113}\mathrm{In}} = A^{^{115}\mathrm{In}} = A^{\mathrm{In}} = 110\,\mu e\mathrm{V}$ from Liu et al. (2007) (see Table 1 of Coish and Baugh (2009)).

First, we note that the sub-leading contribution to $1/T_2$ in Eq. (4.48) ($\propto \epsilon^3$) is suppressed only by one power of $A/\omega_n$ (up to corrections of order unity). Second, this sub-leading correction has the opposite sign of the leading ($\sim \epsilon^2$) term, potentially leading to a non-monotonic dependence of $1/T_2$ on the electron Zeeman splitting when $\epsilon \sim 1$. This non-monotonic dependence can be understood in the following way: As the electron Zeeman energy decreases from a large value $b \gg A$, the perturbative Lamb shift $\Delta\omega \propto 1/b$ increases, eventually reaching the edge of the band of single nuclear pair-flip excitations when $\Delta\omega \sim A/N$, at which point there are no more energy-conserving flip-flop processes. For still lower magnetic fields, higher-order processes are required to conserve energy, but we find that these processes are further suppressed by the small parameter $c_+c_-$ for a polarized nuclear spin system ($c_+c_- \propto (1-p^2)$ for nuclear spin $I = 1/2$) (see Appendix A.5). The qualitative non-monotonic magnetic-field dependence described by Eq. (4.48) will therefore apply at least in the case of a polarized nuclear spin system, even when higher-order terms in $V_{\mathrm{ff}}$ are taken into account.

It is straightforward to extend the analysis of this section to the case of a heteronuclear system. Provided the difference in nuclear Zeeman energies exceeds the excitation bandwidth ($|(\gamma_i - \gamma_j)b| > A/N$), the decoherence rate is given by a sum of contributions from each nuclear species $i$: $1/T_2 = \sum_i \Gamma_i$, where, for a two-dimensional quantum dot with Gaussian envelope

function, we find

$$\Gamma_i = \pi\nu_i^2\alpha_i\left(\epsilon_i^3 - 3\epsilon_i + 2\right)\frac{A^i}{N}\Theta\left(1-\epsilon_i\right), \tag{4.50}$$

$$\epsilon_i = \left|\frac{N\Delta\omega}{A^i}\right|, \quad \Delta\omega = \sum_i \nu_i \frac{\left(c_+^i + c_-^i\right)}{8\omega_n}\frac{A^i}{\omega_n}\frac{A^i}{N}, \tag{4.51}$$

and where we have introduced

$$\alpha_i = \frac{c_+^i c_-^i}{24}\left(\frac{A^i}{\omega_n}\right)^2, \tag{4.52}$$

with coefficients $c_\pm^i = I^i(I^i+1) - \left\langle\left\langle m^i(m^i \pm 1)\right\rangle\right\rangle$ for each isotopic species $i$. We show the magnetic-field dependence of the decoherence rate $1/T_2$ from Eq. (4.50) in Fig. 4.5 for a GaAs quantum dot, and in Fig. 4.6 for an InGaAs quantum dot with a typical indium doping of $x = 0.3$. The dependence of the $1/T_2$ curve on indium doping $x$ for an InGaAs quantum dot is illustrated in Fig. 4.7, where we see that the position of the maximum in the $1/T_2$ curve depends strongly on the concentration of the large-spin isotope (indium). An experimental confirmation of this dependence of the maximum in $1/T_2$ as a function of indium doping would be a strong confirmation of this theory.

## 4.5 Non-perturbative regime: $b \lesssim A$

Although the expression we have given for the self-energy is strictly valid only in the perturbative regime ($b \gg A$), here we explore the non-Markovian dynamics of this solution outside of the regime of strict validity and comment on where the results become unphysical.

We find the positions of poles and evaluate residues and branch-cut integrals numerically to find the coherence factor in this regime. We consider the case of an unpolarized homonuclear spin system with spin $I = 3/2$, appropriate to GaAs. As the electron Zeeman splitting $b$ is lowered from $b \gg A$, we find there is a critical value of $b$ (near $b \simeq 2A$), below which there is a second pole (at $s = s_1$) with exponentially-decaying residue. The coherence factor $x_t$ is then given by a sum over two pole contributions and three branch-cut integrals:

$$x_t = \sum_{i=0,1} P_i(t) - \sum_{j=0,+,-} \beta_j(t). \tag{4.53}$$

For $b = 2A$ (top panel of Fig. 4.8), there are two exponentially-decaying pole contributions, giving rise to a bi-exponential decay with strong envelope modulations corresponding to the difference in the imaginary part of the two poles. At smaller Zeeman energy $A/2 \lesssim b \lesssim A$ (e.g., $b = A$ in the center panel of Fig. 4.8), the pole at $s = s_0$ leaves the continuum band and merges with the imaginary axis, leading to a constant contribution $P_0(t) = P_0$, independent of $t$. For still lower Zeeman splitting $b \lesssim A/2$ ($b = A/2$ in the lower panel of Fig. 4.8), the second pole at $s = s_1$ leaves the continuum band at lower frequency and also merges with the imaginary axis. In this regime, the only decay in the fourth-order solution is due to the small contribution from branch cuts, although envelope modulations remain.

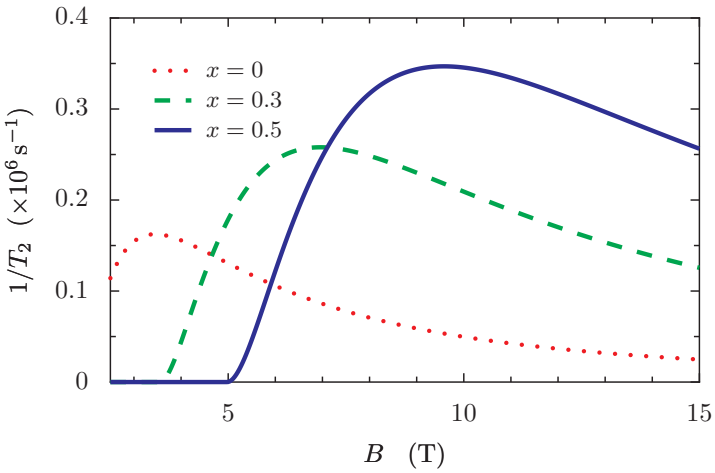


Figure 4.7: Decoherence rate $1/T_2$ for an electron spin in a $In_xGa_{1-x}As$ quantum dot containing $N = 10^5$ nuclei with $g$-factor $|g| = 0.5$ and In doping of $x = 0$, $x = 0.3$, and $x = 0.5$. Hyperfine coupling constants are as given in the caption of Fig. 4.6. The exponential decay rate shown here will be an accurate description of the full decay in the Markovian regime $T_2 \gtrsim \tau_c$, where $\tau_c$ is the bath correlation time. This regime is reached without nuclear polarization ($p = 0$) whenever the perturbative self-energy expansion is valid (see Chapter 3): $A \lesssim b$ ($\tau_c \simeq N/A$ for $A \lesssim b$). At finite polarization, $1/T_2$ will be further reduced (e.g., $1/T_2 \propto 1 - p^2$ for a system with nuclear spin $I = 1/2$), resulting in a dominant exponential decay even at lower electron spin splitting. Thus, at least for large nuclear polarization $p \to 1$, the qualitative behavior shown here will accurately describe the magnetic-field dependence of coherence decay. The behavior at $b \lesssim A$ cannot be accurately determined for $p = 0$ without including higher-order corrections.

The effects in the two lower panels of Fig. 4.8 demonstrate the danger of re-exponentiation of short-time behavior for a system where strong non-Markovian (history-dependent) effects become important. The non-decaying fractions shown in Fig. 4.8 are, however, unphysical consequences of extending the solution to a regime of electron Zeeman splitting where it does not apply. We expect higher-order corrections to the self-energy to broaden the continuum band as higher-order nuclear pair flips are included, resulting in several exponential decay time scales as the electron Zeeman energy is lowered. Nevertheless, we have found that processes that can broaden the continuum band will be suppressed even at small electron Zeeman splitting $b \lesssim A$, provided the nuclear-spin system is polarized (see Appendix A.5), and so some of this behavior will survive at least for a polarized nuclear-spin environment. Whether perturbation theory can be controlled at *any* polarization for $b < A$ through an adequate resummation of relevant terms and short-time approximation, as suggested by Cywiński et al. (2009a,b), is still unclear with the present method.

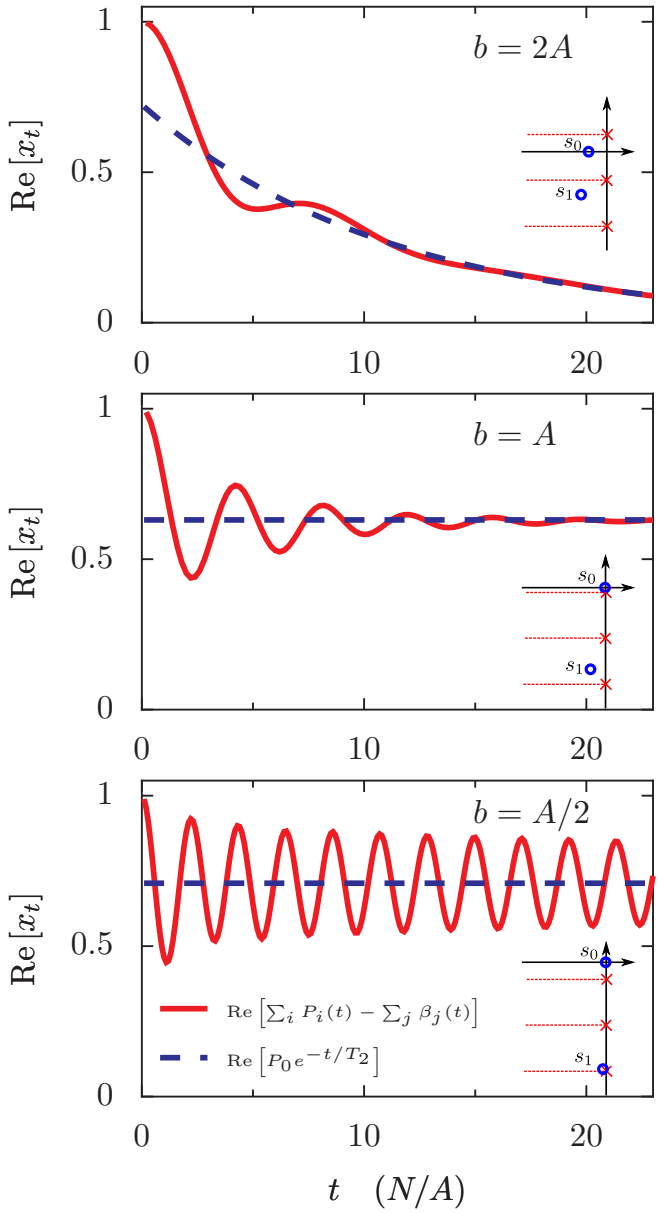


Figure 4.8: Decay envelopes calculated from numerical evaluation of branch-cut integrals and pole contributions for a two-dimensional quantum dot with Gaussian envelope function (solid lines). Dashed lines show the contributions from the dominant pole at $s = s_0$. When the electron Zeeman splitting $b$ is below some critical value $b < b_c \sim A$, a second exponentially-decaying pole appears, leading to a biexponential decay with strong envelope modulations (top, $b = 2A$). When $b$ is decreased further, the dominant pole moves to the real axis (middle, $b = A$). At still smaller values of $b$, the sub-dominant exponential pole has a vanishing decay rate (bottom, $b = A/2$), leading to sustained oscillations. All plots correspond to an unpolarized narrowed nuclear bath with $I = 3/2$. Insets illustrate the approximate relative positions of poles (circles) and branch points (crosses) in each case.

## 4.6 Conclusions

We have investigated transverse-spin dynamics for an electron confined to a quantum dot, interacting with a bath of nuclear spins via the Fermi contact hyperfine interaction. Using one unified technique, we have recovered results that have previously been reported using several different methods. These results include an initial partial decay, followed by a quadratic shoulder, a dominant exponential decay (discussed in Chapter 3), and a long-time power-law tail. Our results for the long-time behavior differ from those given by Yao et al. (2006), Liu et al. (2007), and Cywiński et al. (2009a,b). Here, we have found a long-time power-law decay ($\sim 1/t^2$), in contrast to the long-time exponential decay found by those authors. While the decay law $\sim 1/t^2$ matches that found previously by Deng and Hu (2006, 2008) using an equation-of-motion approach the prefactor found in the present work has a qualitatively different dependence on magnetic field. In contrast to earlier works, which argue in favor of a regime of Gaussian decay (Yao et al., 2006; Liu et al., 2007), here we find that re-exponentiation of the short-time quadratic decay shoulder is never justified. In the perturbative regime $b \gtrsim A$, the system is Markovian, being well-described by a single-exponential decay (see also Chapter 3). As the electron Zeeman splitting is lowered to $b \lesssim A$, we find strong non-Markovian effects (sustained oscillations and multiple decay rates), which once again invalidate re-exponentiation of the short-time decay shoulder.

In addition to recovering previous results, we have found qualitatively new behavior, including modulations of the decay envelope and sub-leading corrections to the decoherence rate for the dominant exponential decay. Our calculation gives an interesting non-monotonic dependence of the decoherence rate $1/T_2$ on magnetic field. These two results (envelope modulations and a non-monotonic dependence of the decoherence rate on magnetic field, both of which should be readily accessible in experiment) are not recovered in dynamics under a leading-order effective Hamiltonian, such as in Chapter 3, suggesting caution should be exercised in interpreting results of high-order expansions involving the effective Hamiltonian.

Chapter 5

# Holes in III-V Semiconductors

## 5.1 Introduction

In Chapters 3 and 4 we have discussed the spin decoherence of an electron confined to a quantum dot and interacting with a narrowed bath of nuclear spins via the Fermi contact hyperfine interaction. We have seen that preparing the nuclear spins in a narrowed state can prolong the electron-spin coherence time significantly: up to and beyond microseconds (see Figs. 4.5 and 4.6). If, however, no special effort is made to control the nuclear environment, the electron-spin coherence times are much shorter, typically on the order of nanoseconds (Merkulov et al., 2002; Khaetskii et al., 2002; Coish and Loss, 2004; Petta et al., 2005).

In this chapter, we want to describe another promising approach to the problem of short coherence times, which we have already mentioned in Chapter 1, i.e., to encode quantum information not into the spin of an electron but into the spin of a heavy hole. Recent experiments have shown initialization and readout of single hole spins in self-assembled quantum dots (Heiss et al., 2007; Ramsay et al., 2008; Gerardot et al., 2008), and control over the number of holes in single gated quantum dots (Komijani et al., 2008), prerequisites for single-hole-spin dephasing-time measurements. Ensemble hole-spin dephasing times have recently been measured in $p$-doped quantum wells (Syperek et al., 2007). Hole-spin coherence times in III-V semiconductor quantum dots have been anticipated to be much longer than electron-spin coherence times due to a weak hyperfine coupling relative to conduction-band electrons (Flissikowski et al., 2003; Shabaev et al., 2003; Woods et al., 2004; Bulaev and Loss, 2005; Laurent et al., 2005; Bulaev and Loss, 2007; Serebrennikov, 2008; Burkard, 2008). In this chapter, we shown that, in contrast, the coupling of a heavy hole (HH) to the nuclear spins in a quantum dot can be rather strong, potentially leading to coherence times that are comparable to those for electrons. However, in the quasi-two-dimensional (Q2D) limit, this interaction takes-on a simple Ising-like form,

$$H = \sum_k A_k^h \, s_z I_k^z, \tag{5.1}$$

where $A_k^h$ is the coupling of the HH to the $k^{\text{th}}$ nucleus, $s_z$ is the hole pseudospin-$\frac{1}{2}$ operator, and $I_k^z$ is the $z$-component of the $k^{\text{th}}$ nuclear-spin operator $\mathbf{I}_k$. The form of this effective Hamiltonian, which should be contrasted to the Heisenberg-type interaction (3.1) of an electron

with nuclear spins, has profound consequences for the spin dynamics. Coherence times can be dramatically extended by preparing the slowly-varying nuclear field in a well-defined state ("narrowing" the field distribution) (Coish and Loss, 2004; Giedke et al., 2006; Stepanenko et al., 2006; Klauser et al., 2006; Reilly et al., 2008; Greilich et al., 2006, 2007). For an electron spin interacting with nuclei via the contact hyperfine interaction, narrowing is effective only up to the time scale where slow internal nuclear-spin dynamics or transverse-coupling ("flip-flop") terms become relevant. As we will explain below, heavy holes confined to two dimensions have negligible flip-flops, potentially leading to significantly longer spin coherence times. The strong coupling of the HH to the nuclear spins is not due to confinement but is also present in bulk crystals, while the Ising-like interaction is a feature of Q2D systems.

## 5.2 Nuclear-spin interactions

### 5.2.1 Hamiltonians

For a relativistic electron in the electromagnetic field of a nucleus with non-zero spin at position $\mathbf{R}_k$, there are three terms that couple the electron spin and orbital angular momentum to the spin of the nucleus (see Chapter 2.2): the Fermi contact hyperfine interaction ($h_1^k$), a dipole-dipole-like interaction (the anisotropic hyperfine interaction, $h_2^k$), and the coupling of electron orbital angular momentum to the nuclear spin ($h_3^k$). Setting $\hbar = 1$, these interactions are described by the following Hamiltonians (Stoneham, 1972):

$$h_1^k = \frac{\mu_0}{4\pi}\,\frac{8\pi}{3}\,\gamma_S\gamma_{j_k}\,\delta(\mathbf{r}_k)\,\mathbf{S}\cdot\mathbf{I}_k, \tag{5.2}$$

$$h_2^k = \frac{\mu_0}{4\pi}\,\gamma_S\gamma_{j_k}\,\frac{3(\mathbf{n}_k\cdot\mathbf{S})(\mathbf{n}_k\cdot\mathbf{I}_k)-\mathbf{S}\cdot\mathbf{I}_k}{r_k^3(1+d/r_k)}, \tag{5.3}$$

$$h_3^k = \frac{\mu_0}{4\pi}\,\gamma_S\gamma_{j_k}\,\frac{\mathbf{L}_k\cdot\mathbf{I}_k}{r_k^3(1+d/r_k)}. \tag{5.4}$$

Here, $\gamma_S = 2\mu_B$, $\gamma_{j_k} = g_{j_k}\mu_N$, $\mu_B$ is the Bohr magneton, $g_{j_k}$ is the nuclear g-factor of isotopic species $j_k$, $\mu_N$ is the nuclear magneton, $\mathbf{r}_k = \mathbf{r} - \mathbf{R}_k$ is the electron-spin position operator relative to the nucleus, $d \simeq Z \times 1.5 \times 10^{-15}\,\mathrm{m}$ is a length of nuclear dimensions, $Z$ is the charge of the nucleus, and $\mathbf{n}_k = \mathbf{r}_k/r_k$. $\mathbf{S}$ and $\mathbf{L}_k = \mathbf{r}_k \times \mathbf{p}$ denote the spin and orbital angular-momentum operators of the electron, respectively.

Nuclear-spin interactions are typically much weaker than the spin-orbit interaction. It is therefore appropriate to form effective Hamiltonians with respect to a basis of eigenstates of the Coulomb and spin-orbit interactions. The $8 \times 8$ Kane Hamiltonian, which describes the band structure of a III-V semiconductor, provides such a basis (Winkler, 2003; Yu and Cardona, 2005). The Kane Hamiltonian is usually written in terms of conduction-band (CB) and valence-band (consisting of HH, light-hole (LH), and split-off sub-band) states. We derive an approximate basis of eigenstates in the HH sub-band by projecting the $8\times 8$ Kane Hamiltonian onto the two-dimensional HH subspace.

To form effective Hamiltonians, we must approximate the crystal-Hamiltonian eigenfunc-

tions given by Bloch's theorem for a single band $n$:

$$\Psi_{n\mathbf{k}\sigma}(\mathbf{r}) = \frac{1}{\sqrt{N_A}}\, e^{i\mathbf{k}\cdot\mathbf{r}} u_{n\mathbf{k}\sigma}(\mathbf{r}), \tag{5.5}$$

where $N_A$ is the number of atomic sites in the crystal, and the Bloch amplitudes $u_{n\mathbf{k}\sigma}(\mathbf{r})$ have the periodicity of the lattice.

We will approximate the $\mathbf{k} = \mathbf{0}$ Bloch amplitudes $u_{n\mathbf{0}\sigma}(\mathbf{r})$ within a primitive unit cell by a linear combination of atomic orbitals – see Eq. (5.15), below. Near an atomic site, the CB Bloch amplitudes have approximate $s$-symmetry (angular momentum $l = 0$), whereas the HH and LH Bloch amplitudes have approximate $p$-symmetry ($l = 1$). Adding spin, the $z$-component of total angular momentum of a HH is $m_J = \pm 3/2$, whereas a LH has $m_J = \pm 1/2$. In the Q2D limit, i.e., going from the bulk crystal to a quantum well (whose growth direction we take to be [001]), a splitting $\Delta_{\mathrm{LH}}$ develops between the HH and LH sub-bands at $\mathbf{k} = \mathbf{0}$ (see Fig. 2.3). We estimate $\Delta_{\mathrm{LH}} \simeq 100\,\mathrm{meV}$ for a quantum well of height $a_z \simeq 5\,\mathrm{nm}$ in GaAs, much larger than the hyperfine coupling (see Appendix B.1). The splitting $\Delta_{\mathrm{LH}}$ is essential since it produces a well-defined two-level system in the HH sub-band, and we can restrict our considerations to the manifold of $m_J = \pm 3/2$ states.

### 5.2.2 Interactions in an atom

Before addressing confinement in quantum dots, we illustrate that the interaction of an electron in a hydrogenic $p$ orbital with the spin of the nucleus (which we choose to be at $\mathbf{R}_k = \mathbf{0}$) is generally non-zero. Moreover, when projected onto the manifold of $m_J = \pm 3/2$ states, this interaction takes-on a simple Ising form. Although our final analysis will apply to any III-V semiconductor, we will take GaAs as a concrete example.

The effective screened nuclear charges $Z_{\mathrm{eff}}$ "felt" by the valence electrons (in $4s$ and $4p$ orbitals) in Ga and As atoms have been calculated by Clementi and Raimondi (1963). The $4s$ orbitals and $4p$ orbitals (with orbital angular momentum $m_L = \pm 1$) are given in terms of hydrogenic eigenfunctions with the replacements $Z \to Z_{\mathrm{eff}}$ by $\Psi_{400}(\mathbf{r}) = R_{40}(r)Y_0^0(\theta,\varphi)$ and $\Psi_{41\pm1}(\mathbf{r}) = R_{41}(r)Y_1^{\pm1}(\theta,\varphi)$, respectively. Including spin and evaluating matrix elements of the Hamiltonians (5.2)-(5.4) with respect to hydrogenic $4s$ states leads to effective spin Hamiltonians of the form (Abragam, 1961; Stoneham, 1972) $h_1^{4s} = A_s \mathbf{S}\cdot\mathbf{I}_k$ and, due to the spherical symmetry of the wavefunction, $h_2^{4s} = h_3^{4s} = 0$. The same procedure with the $4p$ states leads to effective Hamiltonians $h_1^{4p} = 0$ (since $p$-states vanish at the origin) and $h_2^{4p} + h_3^{4p} = A_p s_z I_k^z$, where $s_z = \pm\frac{1}{2}$ corresponds to $m_J = \pm 3/2$. $A_s$ and $A_p$ denote the coupling strengths of electrons in $4s$ and $4p$ orbitals, respectively. Evaluating all integrals exactly gives

$$\frac{A_p}{A_s} = \frac{1}{5}\left(\frac{Z_{\mathrm{eff}}(\kappa, 4p)}{Z_{\mathrm{eff}}(\kappa, 4s)}\right)^3, \qquad \kappa = \mathrm{Ga},\ \mathrm{As}. \tag{5.6}$$

Quite significantly, after inserting the values for $Z_{\mathrm{eff}}$ given by Clementi and Raimondi (1963) into Eq. (5.6), we find that the ratio of coupling strengths is fairly large – on the order of 10%: $A_p/A_s \simeq 0.14$ for Ga, and $A_p/A_s \simeq 0.11$ for As. Since $h_2^k$ and $h_3^k$ do not contribute to the hyperfine interaction of an electron in an $s$ orbital, research on hyperfine interaction for

electrons in an $s$-type conduction band has focused on the contact term $h_1^k$, neglecting the other interactions. The fact that $h_1^k$, in contrast, gives no contribution for an electron in a $p$ orbital has led to the claim that electrons in $p$ orbitals (and holes) do not interact with nuclear spins. Eq. (5.6) shows that $h_2^k$ and $h_3^k$ can contribute significantly. Furthermore, while the interaction of a $4s$-electron with the nuclear spin is of Heisenberg type, within the manifold of $m_J = \pm 3/2$ states, the interaction of a $4p$-electron is Ising-like at leading order (virtual transitions via the $m_J = \pm 1/2$ states may lead to non-Ising corrections). This result is a direct consequence of the Wigner-Eckart theorem and the fact that the Hamiltonians (5.2)-(5.4) can be written in the form $h_i^k = \mathbf{v}_i^k \cdot \mathbf{I}_k$, where $\mathbf{v}_i^k$ are vector operators in the electron (spin and orbital) Hilbert space.

### 5.2.3 Interactions in a quantum dot

We now return to the problem directly relevant to a HH in a two-dimensional quantum well. We consider an additional circular-symmetric parabolic confining potential in the plane of the quantum well defining a quantum dot. Neglecting hybridization with other bands, which we estimate to be typically on the order of 1% (see Appendix B.1), the pseudospin states for a HH within the envelope-function approximation read

$$|\Psi_\sigma\rangle = |\phi; u_{\mathrm{HH}\mathbf{0}\sigma}\rangle|\sigma\rangle, \tag{5.7}$$

where $|\phi; u_{\mathrm{HH}\mathbf{0}\sigma}\rangle$ and $|\sigma\rangle$ ($\sigma = \pm$) denote the orbital and spin states, respectively. The orbital wavefunctions are given explicitly by

$$\langle \mathbf{r}|\phi; u_{\mathrm{HH}\mathbf{0}\sigma}\rangle = \sqrt{v_0}\, \phi(\mathbf{r}) u_{\mathrm{HH}\mathbf{0}\sigma}(\mathbf{r}). \tag{5.8}$$

Here, $v_0$ is the volume occupied by a single atom (half the volume of a two-atom zinc-blende primitive unit cell), and $\phi(\mathbf{r}) = \phi_z(z)\phi_\rho(\rho)$ is the envelope function. The radial ground-state envelope function is a Gaussian:

$$\phi_\rho(\rho) = \frac{1}{\sqrt{\pi} l}\, \exp\left(-\frac{\rho^2}{2l^2}\right), \tag{5.9}$$

where $\boldsymbol{\rho} = (x, y)$, $\rho = |\boldsymbol{\rho}|$, $l = l_0\,[1 + (B_z/B_0)^2]^{-1/4}$, $B_z$ is the component of an externally applied magnetic field along the growth direction and $B_0 = \Phi_0/\pi l_0^2$ where $\Phi_0 = h/|e|$ is a flux quantum. A typical dot Bohr radius of $l_0 = 30\,\mathrm{nm}$ gives $B_0 \simeq 1.5\,\mathrm{T}$.

In a solid, the HH is delocalized over the lattice sites of the crystal. The nuclei do not interact solely with the fraction of the HH in the same primitive unit cell ('on-site' interaction), but also with density localized at more distant atomic sites (long-ranged interactions). We neglect the long-ranged interactions, which lead to corrections on the order of 1% relative to the on-site interaction (see Appendix B.3). If the envelope function varies slowly on the length scale of a primitive cell, we find (combining $h_2^k$ and $h_3^k$) $A_k^h = A_h^{j_k} v_0 |\phi(\mathbf{R}_k)|^2$, where

$$A_h^{j_k} = -\frac{\mu_0}{4\pi}\, \gamma_S \gamma_{j_k} \left\langle \frac{3\cos^2\theta_k + 1}{r_k^3 (1 + d/r_k)} \right\rangle_{\mathrm{p.c.}}. \tag{5.10}$$

Here, $\langle \cdots \rangle_{\text{p.c.}}$ denotes the expectation value with respect to $u_{\text{HH}\mathbf{0}\sigma}(\mathbf{r})$ over a primitive unit cell ($\sigma = \pm$ give the same matrix elements), and $\theta_k$ is the polar angle of $\mathbf{r}_k$. The magnetic moment of a HH is inverted with respect to that for an electron. This results in a change of sign in Eqs. (5.2)-(5.4) and leads to the minus sign in Eq. (5.10) and of the values in columns (i) and (ii) of Table 5.1.

### 5.2.4 Non-Ising corrections

There will be small corrections to the form of the effective Hamiltonian given in Eq. (5.1). Evaluating off-diagonal matrix elements of (5.3) and (5.4) with the approximate Bloch amplitudes (5.15) yields non-Ising terms, whose associated coupling strengths $A_h^\perp$ we find to be small: $A_h^\perp < 0.06\, A_h^j$. Higher-order virtual transitions between the $m_J = \pm 3/2$ states via the LH sub-band are suppressed by $\sim A_k^h/\Delta_{\text{LH}} \ll 1$. Hybridization with other bands can also lead to non-Ising corrections. For unstrained quantum dots, we find that these corrections are small: typically on the order of 1% of the values given in Table I (see also Appendix B.1). Strain can lead to considerably stronger band mixing and, hence, to significantly larger non-Ising corrections to Eq. (5.1).

## 5.3 Spin Decoherence

Now that the effective Hamiltonian (5.1) has been established, we can analyze the dephasing of a HH pseudospin in the presence of a random nuclear environment. In an applied magnetic field, pseudospin dynamics of the HH are described by the Hamiltonian

$$H = (b_\perp + h_z)\, s_z + b_\parallel s_x, \tag{5.11}$$

where $h_z = \sum_k A_k^h I_k^z$ is the nuclear field operator, $b_\perp = g_\perp \mu_B B_z$ is the Zeeman splitting due to a magnetic field $B_z$ along the growth direction, and $b_\parallel = g_\parallel \mu_B B_x$ is the Zeeman splitting due to an applied magnetic field $B_x$ in the plane of the quantum dot. $g_\perp$ and $g_\parallel$ are the components of the HH g-tensor along the growth direction and in the plane of the quantum dot, respectively (we assume the in-plane g-tensor to be isotropic).

If no special effort is made to control the nuclear field, the field value will be Gaussian-distributed in the limit of a large number of nuclear spins (Coish and Loss, 2004). The variance for a random nuclear-spin distribution is (see Appendix B.4)

$$\langle h_z^2 \rangle = \sigma^2 \simeq \frac{1}{4N} \sum_j \nu_j I^j (I^j + 1)(A_h^j)^2, \tag{5.12}$$

where $N = \pi l^2 a_z / v_0$ is the number of nuclei within the quantum dot. The nuclear-field fluctuation $\sigma$ therefore inherits a magnetic-field dependence from $l$ (see Eq. (5.9)). A finite nuclear-field variance will result in a random distribution of precession frequencies experienced by the hole pseudospin, inducing pure dephasing (decay of the components of hole pseudospin transverse to $\mathbf{B}$).

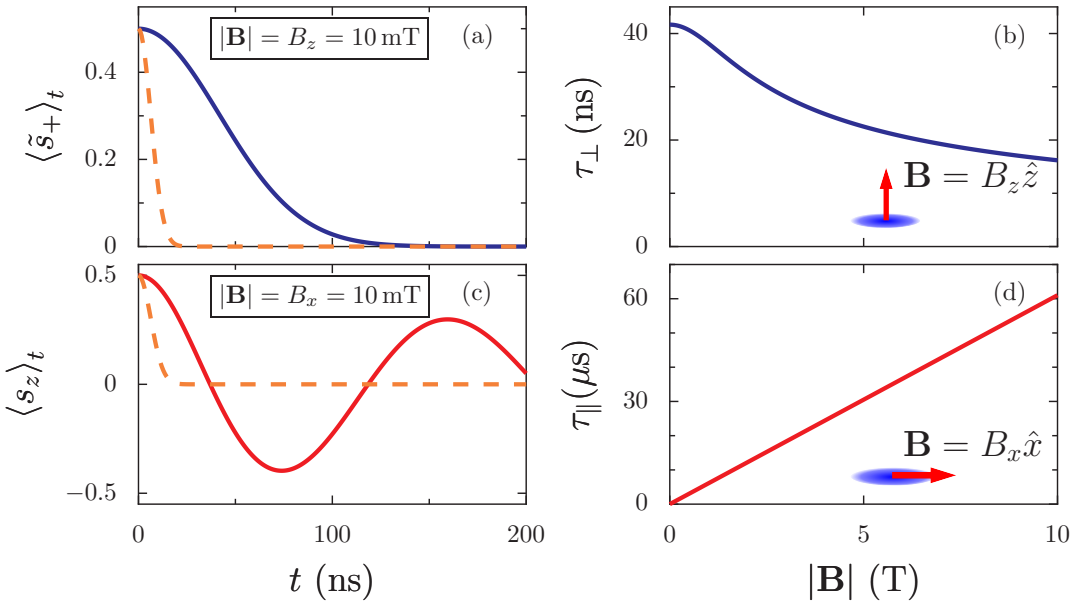


Figure 5.1: Dephasing of HH pseudospin states (solid lines in (a) and (c)). The decay is Gaussian for an out-of-plane magnetic field $B_z$ (a) (see Eq. (5.13)) and given by a slow power law at long times ($\sim 1/\sqrt{t}$) for an in-plane magnetic field $B_x$ (c) (see Eq.(5.14)). We have chosen $|\mathbf{B}| = 10\,\mathrm{mT}$ in (a) and (c). Magnetic-field dependencies of the relevant coherence times are shown for a field that is out-of-plane (b) and in-plane (d). We have assumed $g_\parallel = 0.04$ (Marie et al., 1999) and a zero-field lateral dot size $l_0 = 30\,\mathrm{nm}$ and height $a_z = 5\,\mathrm{nm}$, leading to $N = \pi l_0^2 a_z/v_0 = 6.5\times 10^5$ nuclei within the dot at $B_z = 0$. We have taken $v_0 = a_L^3/8$, where $a_L = 5.65\,\text{Å}$ is the GaAs lattice constant. The dashed lines in (a) and (c) show the dephasing of CB electron spin states in the high-field limit, $|\mathbf{B}| \gg \sigma_e/g_e\mu_B$, where $g_e$ is the electron g-factor, and $\sigma_e$ is obtained from Eq. (5.12) by replacing $A_h^j$ by the electron hyperfine coupling constants $A_e^j$.

First, we consider the case $b_\parallel = 0$. For a hole pseudospin initially oriented along the $x$ direction, we find a Gaussian decay (see Fig. 5.1 (a)) of the transverse pseudospin in the rotating frame $\langle \tilde{s}_+\rangle_t = \exp(-ib_\perp t)\left(\langle s_x\rangle_t + i\langle s_y\rangle_t\right)$:

$$\langle \tilde{s}_+\rangle_t = \frac{1}{2}\exp\left(-\frac{t^2}{2\tau_\perp^2}\right), \qquad \tau_\perp = \frac{1}{\sigma}. \tag{5.13}$$

This is the same Gaussian decay that occurs for electrons (Merkulov et al., 2002; Khaetskii et al., 2002; Coish and Loss, 2004). Here, since the magnetic field is taken to be out-of-plane, we must take account of the diamagnetic "squeezing" of the wavefunction. This squeezing affects the number $N$ of nuclear spins within the dot and hence, the finite-size fluctuation $\sigma$. The coherence time $\tau_\perp(B_z) = 1/\sigma(B_z) = \tau_\perp(0)\left[1 + (B_z/B_0)^2\right]^{-1/4}$ then *decreases* for large $B_z$ (see Fig. 5.1 (b)). This undesirable effect can be avoided for confined electron spins by generating a large Zeeman splitting through an in-plane (rather than out-of-plane) magnetic field. This option may not be available for a HH where, typically, $g_\parallel \ll g_\perp$.

| j | $A_h^j$ ($\mu$eV) | | $A_e^j$ ($\mu$eV) | |
|---|---|---|---|---|
| | (i) | (ii) | (iii) | (iv) |
| $^{69}$Ga | -7.1 | -13 | 40 | 74 |
| $^{71}$Ga | -9.0 | -17 | 51 | 94 |
| $^{75}$As | -8.2 | -12 | 59 | 89 |
| $A_\alpha = \sum_j \nu_j A_\alpha^j \quad (\alpha = e, h)$ | -8.0 | -13 | 52 | 86 |

Table 5.1: Estimates of the coupling strengths for a HH ($A_h^j$) and a CB electron ($A_e^j$) for the three isotopes in GaAs. Columns (i) and (iii) show values obtained from a linear combination of hydrogenic eigenfunctions, using free-atom values of $Z_{\text{eff}}$ calculated by Clementi and Raimondi (1963). Column (iv) gives the accepted values of $A_e^j$ from Paget et al. (1977). Column (ii) shows the rescaled values from column (i) (see text). In the last row we give the average coupling constants weighted by the natural isotopic abundances: $\nu_{^{69}\text{Ga}} = 0.3$, $\nu_{^{71}\text{Ga}} = 0.2$, $\nu_{^{75}\text{As}} = 0.5$.

The situation changes drastically for an in-plane magnetic field ($b_\perp = 0$). In this case, since the hyperfine fluctuations are purely transverse to the applied field direction, the decay is given by a slow power law at long times (see Fig. 5.1 (c)) and the relevant dephasing time *increases* as a function of the applied magnetic field (see Fig. 5.1 (d)). In the limit $b_\parallel \gg \sigma$ and for a HH pseudospin initially prepared along the $\hat{z}$-direction, we find

$$\langle s_z \rangle_t \simeq \frac{\cos\left(b_\parallel t + \frac{1}{2}\arctan(t/\tau_\parallel)\right)}{2[1 + (\frac{t}{\tau_\parallel})^2]^{1/4}}, \qquad \tau_\parallel = \frac{b_\parallel}{\sigma^2}. \tag{5.14}$$

The derivation of Eq. (5.14) is directly analogous to that for the decay of driven Rabi oscillations (Koppens et al., 2007).

## 5.4 Estimates of the coupling strengths

To estimate the size of $A_h^j$, we need an explicit expression for the HH $\mathbf{k} = \mathbf{0}$ Bloch amplitudes. We approximate $u_{\text{HH}\mathbf{0}\sigma}(\mathbf{r})$ within a Wigner-Seitz cell centered halfway along the Ga-As bond by a linear combination of atomic orbitals, following Gueron (1964):

$$u_{\text{HH}\mathbf{0}\sigma}(\mathbf{r})\Big|_{\mathbf{r}\in\text{WS}} = N_{\alpha_v}\Big(\alpha_v \Psi_{41\sigma}^{\text{Ga}}(\mathbf{r} + \mathbf{d}/2) + \sqrt{1-\alpha_v^2}\,\Psi_{41\sigma}^{\text{As}}(\mathbf{r} - \mathbf{d}/2)\Big). \tag{5.15}$$

Here, $\mathbf{d} = \frac{a}{4}(1,1,1)$ is the Ga-As bond vector, $a$ is the lattice constant, $\alpha_v$ describes the relative electron sharing at the Ga and As sites in the HH sub-band, and $N_{\alpha_v}$ is a normalization constant, chosen to enforce $\int_{\text{WS}} d^3r |u_{\text{HH}\mathbf{0}\sigma}(\mathbf{r})|^2 = 2$, where the integration is performed over the Wigner-Seitz cell defined above. To simplify numerical integration, we replace the Wigner-Seitz cell by a sphere centered halfway along the Ga-As bond, with radius given by half the Ga-Ga nearest-neighbor distance. We find the electron sharing in the CB from the densities given by Paget et al. (1977) to be $\alpha_c^2 \simeq 1/2$ (see Appendix B.2) and assume the same ($\alpha_v^2 = 1/2$) for Eq. (5.15). Using $Z_{\text{eff}}$ for free atoms (Clementi and Raimondi, 1963), we evaluate Eq. (5.10) with

the ansatz (5.15), by numerical integration, giving the values shown in Table 5.1, column (i). We check the validity of this procedure by writing the CB Bloch amplitudes as in Eq. (5.15), replacing the $4p$-eigenfunctions by $4s$-eigenfunctions. Evaluating the coupling constants for the CB ($A_e^j$) from $h_1^k$ gives the numbers in column (iii). The accepted values of $A_e^j$ from Paget et al. (1977) are shown in column (iv) for comparison. Our method produces $A_e^j$ to within a factor of two of the accepted values. Our procedure, which relies on free-atom orbitals, most likely under-estimates the electron density near the atomic sites, which should be enhanced in a solid due to confinement. Assuming the relative change in density going from a free atom to a solid is the same for the CB and HH band, we rescale the results in column (i) by the ratio of the values in columns (iv) and (iii), giving column (ii). Due to the approximations involved, we expect the values in columns (i) and (ii) only to be valid to within a factor of two or three.

## 5.5 Conclusions

We have shown that the interaction of a quantum-dot-confined heavy hole with nuclear spins is stronger than previously anticipated. We have estimated the associated coupling strength to be on the order of $10\mu e$V in GaAs – only one order of magnitude less than the hyperfine coupling for electrons. However, the interaction turns out to be Ising-like which has profound consequences for hole-spin decoherence. Since no flip-flop terms occur in the effective Hamiltonian (5.1), the main source of decoherence is given by the broad frequency distribution of the nuclear spins. Recent theoretical and experimental studies have shown that state-narrowing techniques are capable of strongly suppressing this source of decoherence, which makes the heavy hole an attractive spin-qubit candidate.

Very recently, experimental results on hole-spin relaxation in self-assembled quantum dots have been released (Gerardot et al., 2008; Eble et al., 2009). Gerardot *et al.* report an extremely weak coupling of HH spin states, which is explained by our theory to be a direct consequence of the Ising-like nuclear-spin interaction (negligible flip-flop terms). Eble *et al.*, in contrast, find very short hole-spin relaxation times on the order of 15 nanoseconds. This is due to the strong strain present in the particular dots used in this experiment, resulting in a considerable HH-LH mixing and a highly non-Ising interaction (large flip-flop terms).

Chapter 6

# Holes in III-V Semiconductors: Narrowed Nuclear-Spin Bath

## 6.1 Introduction

In the previous chapter, we have discussed the interaction of a heavy hole (HH) confined to a III-V semiconductor quantum dot (QD) with the spins of the nuclei residing in the host material. We have seen that the for HHs, the form of the nuclear-spin interaction is predominantly Ising-like, in contrast to the Heisenberg-type interaction of electrons. We have found an ensemble-hole-spin decoherence due to the inhomogeneous broadening of the nuclear magnetic field (Overhauser field), whose associated decoherence time dramatically depends on the direction (and magnitude) of the externally applied magnetic field.

Several possibilities to suppress decoherence due to inhomogeneous broadening have been proposed (see Chapter 1), one of which is to prepare the nuclear spins in a so-called narrowed or frequency-focused state (Coish and Loss, 2004; Klauser et al., 2006; Stepanenko et al., 2006). On the experimental side, enormous progress has been achieved in preparing such narrowed states (Greilich et al., 2006, 2007; Reilly et al., 2008; Greilich et al., 2009; Latta et al., 2009; Xu et al., 2009; Vink et al., 2009), which have been shown to persist over astonishingly long timescales exceeding hours (Greilich et al., 2007). As we have discussed in Chapters 3 and 4, for electrons interacting with a narrowed nuclear bath, spin decoherence happens due to nuclear pair flip processes induced by the transverse hyperfine interaction, and the associated single-spin decoherence time $T_2$ can be several orders of magnitude longer than the ensemble-spin decoherence time $T_2^*$ (Coish et al., 2008; Cywiński et al., 2009b). For HHs, with their predominantly Ising-like coupling to nuclear spins (Fischer et al., 2008), this transverse interaction (perpendicular to the Ising axis) can be expected to be very small, potentially leading to very long single-hole-spin decoherence times $T_2$.

In this chapter, we study the spin dynamics of a HH confined to a III-V semiconductor QD and interacting with a narrowed nuclear-spin bath. We show that band hybridization leads to non-Ising (transverse) terms in the hyperfine Hamiltonian, whose magnitude depends on the geometry of the QD. This transverse coupling induces nuclear pair-flip processes, leading to

fluctuations of the Overhauser field and to exponential single-hole-spin decoherence. We show that for typical unstrained quantum dots the associated timescale $T_2$ has a lower bound on the order of tens of microseconds and that it can be tuned over many orders of magnitude by changing external parameters such as the applied magnetic field. Thus, it is in principle possible to operate hole-spin QDs in a regime where the hyperfine interaction is practically switched off and where other decoherence mechanisms, such as nuclear dipole or spin-orbit interactions, will become relevant and, hence, experimentally observable.

## 6.2 Hybridized states

We start from the $8 \times 8$ Kane Hamiltonian describing states in the conduction band (CB), heavy-hole (HH), light-hole (LH) and split-off (SO) bands of bulk III-V semiconductors (see Appendix C of Ref. Winkler (2003)). The Kane Hamiltonian can be 'folded down' to an effective $2 \times 2$ Hamiltonian whose eigenstates describe the spin states in the band of interest, where the admixture of neighboring bands is taken into account perturbatively (Winkler, 2003). Using this procedure, we find the following hybridized HH pseudospin states (see Appendix B.5):

$$|\Psi_\pm\rangle \simeq \mathcal{N}\Big(|u^\pm_{\rm HH};\phi^{00}_{\rm HH}\rangle|\pm_{\rm HH}\rangle \mp \lambda_{\rm CB}\,|u^\pm_{\rm CB};\phi^{0\pm}_{\rm CB}\rangle|\pm_{\rm CB}\rangle \pm \lambda_{\rm LH}\,|u^\pm_{\rm LH};\phi^{1\pm}_{\rm LH}\rangle|\pm_{\rm LH}\rangle\Big). \tag{6.1}$$

Here, we have assumed a parabolic confinement potential $V_{\rm QD} = m_\parallel\omega_\parallel^2(x^2+y^2)/2 + m_\perp\omega_\perp^2 z^2/2$ defining the QD, where $m_\perp = m_0/(\gamma_1-2\gamma_2)$ and $m_\parallel = m_0/(\gamma_1+\gamma_2)$ are the HH effective masses along the growth axis $z$ (taken to be along [001]) and in the $xy$-plane, respectively, $\gamma_1$ and $\gamma_2$ are the Luttinger parameters, $m_0$ is the free-electron mass, $\omega_\perp = \hbar/(m_\perp a_z^2)$ with quantum-well height $2a_z$, $\omega_\parallel = \hbar/(m_\parallel L^2)$ with quantum-dot radius $L$, and $\mathcal{N}$ enforces proper normalization of the wavefunctions. The condition for the validity of Eq. (6.1) is given by $a_z \ll L$, which is needed for the perturbation expansion on the Kane Hamiltonian. The amount of CB and LH admixture is determined by the dimensionless prefactors

$$\lambda_{\rm CB} = i\beta_{\rm CB}\frac{P}{\sqrt{2}LE_g}, \qquad \lambda_{\rm LH} = \frac{\sqrt{3}}{2\sqrt{2}}\frac{\gamma_3}{\gamma_2}\beta_{\rm LH}\frac{a_z L}{L^2-a_z^2}, \tag{6.2}$$

where $P$ is the interband momentum, $E_g$ is the fundamental band gap, and

$$\beta_{\rm CB} = \frac{4(\gamma_1+\gamma_2)}{(1+\gamma_1+\gamma_2)^2}\frac{\sqrt{2}(\gamma_1-2\gamma_2)^{1/4}}{\sqrt{1+(\gamma_1-2\gamma_2)}}, \qquad \beta_{\rm LH} = \left[1-\left(\frac{\gamma_2}{\gamma_1}\right)^2\right]\frac{(\gamma_1^2-4\gamma_2^2)^{3/4}}{\gamma_1^{3/2}} \tag{6.3}$$

come from envelope-function overlap integrals of the form $\langle\phi^{00}_{\rm HH}|k_\pm k_z|\phi^{1\pm}_{\rm LH}\rangle$ and account for the difference in effective masses between the bands.

Near the Γ-point, the spin-orbit-coupled states can be approximated by

$$|u_{\rm CB\pm}\rangle|\pm_{\rm CB}\rangle \simeq |s\rangle|\uparrow,\downarrow\rangle, \tag{6.4}$$

$$|u_{\rm HH\pm}\rangle|\pm_{\rm HH}\rangle \simeq |p_\pm\rangle|\uparrow,\downarrow\rangle, \tag{6.5}$$

$$|u_{\rm LH\pm}\rangle|\pm_{\rm LH}\rangle \simeq \frac{1}{\sqrt{3}}(\sqrt{2}|p_z\rangle|\uparrow,\downarrow\rangle \mp |p_\pm\rangle|\downarrow,\uparrow\rangle), \tag{6.6}$$

in terms of $s$- and $p$-symmetric Bloch states ($|p_\pm\rangle = (|p_x\rangle \pm i|p_y\rangle)/\sqrt{2}$) and real-spin states $|\uparrow,\downarrow\rangle$ with respect to the growth axis (Winkler, 2003). The envelope functions appearing in Eq. (6.1) are defined via their position representations $\langle \mathbf{r}|\phi_\alpha^{ij}\rangle = \phi_\alpha^i(z)\phi_\alpha^j(x,y)$ ($i = 0,1$, $j = 0,\pm$), where $\phi_\alpha^0(x,y) = \phi_\alpha^0(x)\phi_\alpha^0(y)$, $\phi_\alpha^\pm(x,y) = (\phi_\alpha^1(x)\phi_\alpha^0(y) \pm i\phi_\alpha^0(x)\phi_\alpha^1(y))/\sqrt{2}$, and $\phi_\alpha^n(x)$ is the $n^{\text{th}}$ harmonic-oscillator eigenfunction along the $x$-direction in band $\alpha$. Due to terms appearing in the Kane Hamiltonian which are linear in the crystal momentum $\mathbf{k}$ and which couple neighboring bands, the admixture of CB and LH states features *excited-state* envelope functions. This has profound physical consequences which will be discussed below. For a quantum dot with $L = 10$nm and $a_z = 2$nm, we estimate $|\lambda_{\text{CB}}| \simeq 0.02$, $|\lambda_{\text{LH}}| \simeq 0.11$ for GaAs. The split-off-band contribution to the HH states is very small has thus been neglected in Eq. (6.1).

## 6.3 Nuclear-spin interactions and effective Hamiltonian

As we have already discussed in Chapter 5, there are three interactions that couple the HH – whose pseudospin states have been derived in Eq. (6.1) – to the spins of the surrounding nuclei: the Fermi contact interaction $h_1^k$, the anisotropic hyperfine interaction $h_2^k$, and the coupling of orbital angular momentum to the nuclear spins $h_3^k$, which are represented by the following Hamiltonians (setting $\hbar = 1$) (Stoneham, 1972):

$$h_1^k = \frac{\mu_0}{4\pi}\frac{8\pi}{3}\,\gamma_S\gamma_{j_k}\,\delta(\mathbf{r}_k)\,\mathbf{S}\cdot\mathbf{I}_k, \tag{6.7}$$

$$h_2^k = \frac{\mu_0}{4\pi}\,\gamma_S\gamma_{j_k}\,\frac{3(\mathbf{n}_k\cdot\mathbf{S})(\mathbf{n}_k\cdot\mathbf{I}_k) - \mathbf{S}\cdot\mathbf{I}_k}{r_k^3(1+d/r_k)}, \tag{6.8}$$

$$h_3^k = \frac{\mu_0}{4\pi}\,\gamma_S\gamma_{j_k}\,\frac{\mathbf{L}_k\cdot\mathbf{I}_k}{r_k^3(1+d/r_k)}. \tag{6.9}$$

Here, $\gamma_S = 2\mu_B$, $\gamma_{j_k} = g_{j_k}\mu_N$, $\mu_B$ is the Bohr magneton, $g_{j_k}$ is the nuclear g-factor of isotopic species $j_k$ at lattice site $k$, $\mu_N$ is the nuclear magneton, $\mathbf{r}_k = \mathbf{r} - \mathbf{R}_k$ is the electron-spin position operator relative to the $k^{\text{th}}$ nucleus with spin $\mathbf{I}_k$, $d \simeq Z \times 1.5 \times 10^{-15}$ m is a length of nuclear dimensions, $Z$ is the charge of the nucleus, and $\mathbf{n}_k = \mathbf{r}_k/r_k$. $\mathbf{S}$ and $\mathbf{L}_k = \mathbf{r}_k \times \mathbf{p}$ denote the spin and orbital angular-momentum operators of the HH, respectively.

In order to derive an effective spin Hamiltonian for the HH, we take matrix elements $\langle\Psi_\tau|h_i^k|\Psi_{\tau'}\rangle$ ($\tau,\tau' = \pm$, $i = 1,2,3$) with respect to the hybridized HH wavefunctions (6.1). Due to the $\delta$-function in Eq. (6.7), only the CB admixture contributes to the Fermi contact interaction, since $p$-states vanish at the positions $\mathbf{R}_k$ of the nuclei. On the other hand, the terms in Eq. (6.1) associated with HH and LH states contribute to matrix elements of Eqs. (6.8) and (6.9), while the CB admixture does not contribute due to symmetry ($h_2^k$) and vanishing orbital angular momentum ($h_3^k$). Adding up all contributions, and taking into account a Zeeman term due to a magnetic field $B$ along the $z$-direction (Faraday geometry), we find the following effective spin Hamiltonian describing the hole-nuclear-spin interactions:

$$H = (b + h^z)S^z + \frac{1}{2}(h^+S^- + h^-S^+). \tag{6.10}$$

Here, $b = g_h \mu_B B$ is the Zeeman energy of the HH, $g_h$ is the HH g-factor along the magnetic-field direction $z$, and $\mu_B$ is the Bohr magneton. The Overhauser-field components are defined by

$$h^z = \sum_k A_k^z I_k^z, \qquad h^\pm = \sum_k A_k^\pm I_k^\pm, \tag{6.11}$$

where $I_k^\pm = I_k^x \pm i I_k^y$ and where $A_k^z$ and $A_k^\pm$ denote the longitudinal and transverse hyperfine coupling of the HH to the $k^{\text{th}}$ nuclear spin, respectively.

The hybridized states in Eq. (6.1) are predominantly HH-like. We have shown in Chapter 5 that taking matrix elements of the Hamiltonians (6.7)-(6.9) with respect to pure HH states (i.e., neglecting band hybridization) results in an Ising Hamiltonian $h^z S^z$. The longitudinal coupling constants are thus dominated by the HH contribution, $A_k^z \simeq A_{k,\text{HH}}^z$, and the transverse (non-Ising) terms in Eq. (6.10) are only due to hybridzation with CB and LH states, $A_k^\pm = A_{k,\text{CB}}^\pm + A_{k,\text{LH}}^\pm$. Explicitly, the longitudinal and transverse coupling constants are given by

$$A_{k,\text{HH}}^z \simeq A_{\text{HH}}^{j_k} v_0 |\phi_0(z_k)|^2 |\phi_0(x_k, y_k)|^2, \tag{6.12}$$

$$A_{k,\text{CB}}^\pm \simeq A_{\text{CB}}^{j_k} v_0 |\phi_0(z_k)|^2 \phi_\pm^*(x_k, y_k) \phi_\mp(x_k, y_k), \tag{6.13}$$

$$A_{k,\text{LH}}^\pm \simeq A_{\text{LH}}^{j_k} v_0 |\phi_1(z_k)|^2 \phi_\mp^*(x_k, y_k) \phi_\pm(x_k, y_k), \tag{6.14}$$

respectively, where $v_0$ is the volume occupied by one nucleus and $A_\alpha^{j_k}$ is the hyperfine coupling strength of isotope $j_k$ associated with band $\alpha$. Introducing the average $A_\alpha = \sum_j \nu_j A_\alpha^j$, where $\nu_j$ denotes the abundance of isotope $j$, we estimate $A_{\text{HH}} \simeq -13\mu e\text{V}$ (Fischer et al., 2008), $A_{\text{CB}} \simeq 0.02\mu e\text{V}$, and $A_{\text{LH}} \simeq 0.05\mu e\text{V}$ for a GaAs QD with $L = 10\text{nm}$ and $a_z = 2\text{nm}$. In contrast to the interaction of an electron with nuclear spins, the hole-nuclear-spin interaction given in Eq. (6.10) is highly anisotropic. $A_{\text{CB}} \propto |\lambda_{\text{CB}}|^2$ and $A_{\text{LH}} \propto |\lambda_{\text{LH}}|^2$ have a strong dependence on the QD geometry, therefore the non-Ising terms in Eq. (6.10) can be 'tuned' to be more CB or LH-like.

## 6.4 Hole-spin dynamics

We now study the dynamics of the transverse spin component $S^+$ describing the coherence of the HH pseudospin states. To this end, we use the Nakajima-Zwanzig master equation (see also Chapter 4)

$$\langle \dot{S}^+ \rangle_t = i\omega_n \langle S^+ \rangle_t - i \int_0^t dt' \, \Sigma(t - t') \langle S^+ \rangle_{t'}, \tag{6.15}$$

where $\omega = b + h^z$, $\omega|n\rangle = \omega_n|n\rangle$, and $|n\rangle$ denotes a narrowed state of the nuclear-spin system. $\Sigma(t) = \text{tr}\{S^+ \hat{\Sigma}(t) S^- |n\rangle\langle n|\}$ is the self-energy (or memory kernel) describing the transverse-spin dynamics, where $\hat{\Sigma}(t) = -i\mathsf{P}L\mathsf{Q}e^{-iL\mathsf{Q}t}\mathsf{Q}L\mathsf{P}$, $\mathsf{P}$ is a projector onto a product state of HH and nuclear spins, $\mathsf{Q} = 1 - \mathsf{P}$, and $L\mathcal{O} = [H, \mathcal{O}]$ for some operator $\mathcal{O}$ acting on the total Hilbert space of HH and nuclear spins (Coish and Loss, 2004). It is convenient to perform a Laplace transform $f(s) = \int_0^\infty dt \, e^{-st} f(t)$ on the integro-differential equation (6.15), yielding an algebraic equation of the form

$$S^+(s + i\omega_n) = \frac{\langle S^+ \rangle_0}{s + i\Sigma(s + i\omega_n)} \tag{6.16}$$

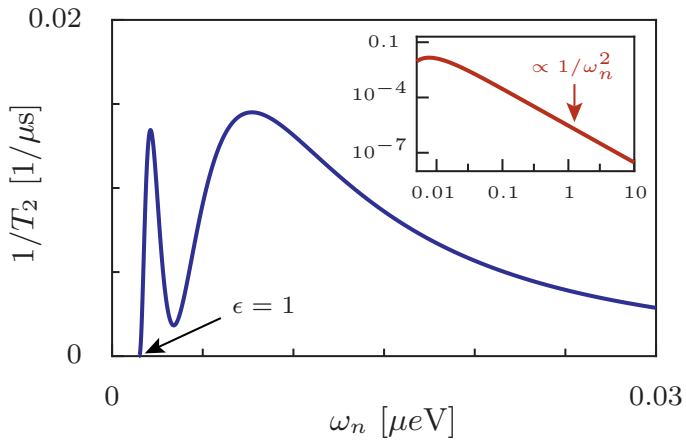


Figure 6.1: Decoherence rate $1/T_2$ from Eq. (6.21) as a function of the HH Zeeman energy $\omega_n = g_h\mu_B B + pIA_{\rm HH}$. For $L = 10$nm and $a_z = 4$nm, we estimate $N \simeq 7.3 \times 10^4$. Inset: $1/T_2$ for Zeeman splittings up to $10\mu e$V, corresponding to magnetic fields of $B \simeq 1$T or a polarization $p \simeq 1$ (axes in the same units as in the main figure).

in the frame rotating with frequency $\omega_n$. Eqs. (6.15) and (6.16) are exact equations describing, in general, non-Markovian dynamics of the transverse HH-spin component. The structure of the self-energy $\Sigma(s)$ is, however, very complex, so we have to resort to an approximation scheme. The energy scales associated with the transverse coupling $V = (h^+S^- + h^-S^+)/2$ are much smaller than those associated with the longitudinal coupling $H_0 = (b + h^z)S^z$ (see above), and we expand the self-energy in powers of hole-nuclear-spin flip-flop processes induced by $V$: $\Sigma(s) = \Sigma^{(2)}(s) + \Sigma^{(4)}(s) + \mathcal{O}(V^6)$. Odd orders in $V$ vanish because of the Zeeman mismatch between HH and nuclear spins which energetically forbids such processes. For a nuclear spin $I$ of order unity, the smallness parameter which controls this expansion is given approximately by $A_\perp/\omega_n$ (see Appendix A of Coish and Loss (2004)), where $A_\perp = \sqrt{A_{\rm CB}^2 + A_{\rm LH}^2}$. For a GaAs QD with $L = 10$nm and $a_z = 2$nm, $A_\perp < \omega_n = g_h\mu_B B + pIA_z$ ($A_z = |A_{\rm HH}|$) for an external field $B \gtrsim 0.5$mT or a nuclear-spin polarization $p \gtrsim 0.5\%$.

We evaluate the second- and fourth-order self-energy contributions explicitly, following the procedure described in Appendix A.4 for the electron case. We find, for a homonuclear system in the frame rotating with frequency $\omega_n$,

$$\Sigma^{(2)}(s + i\omega_n) \simeq -\frac{c_+ + c_-}{4\omega_n}\sum_k |A_k^\pm|^2, \tag{6.17}$$

$$\Sigma^{(4)}(s + i\omega_n) \simeq -i\frac{c_+c_-}{4\omega_n^2}\sum_{k_1,k_2}\frac{|A_{k_1}^\pm|^2|A_{k_2}^\pm|^2}{s + i(A_{k_1}^z - A_{k_2}^z)}, \tag{6.18}$$

where the sums run over all nuclear sites $k$. We have introduced $c_\pm = I(I+1) - \langle\langle m(m\pm 1)\rangle\rangle$, where $I$ is the nuclear spin, $m = -I, \ldots, I$, and the double angle bracket indicates averaging over the $I_k^z$ eigenvalues $m$ (Coish and Loss, 2004).

We emphasize that the structure of the self-energies $\Sigma^{(2)}$ and $\Sigma^{(4)}$ bears some similarity with our previous results on electron-spin decoherence (compare directly with Eqs. (A.50) and (A.53)). However, there are two important differences compared to the electron case: (i) The appearance of different coupling constants $A_k^z$ and $A_k^\pm$ in Eqs. (6.17) and (6.18) is due to the anisotropy of the hyperfine Hamiltonian (6.10) and provides an additional smallness factor $A_\perp/A_z \ll 1$ to the self-energy (6.20). (ii) The spatial dependence of the transverse coupling constants differs from the longitudinal ones due to the appearance of excited-state envelope functions. In particular, this means that nuclear spins at the edge of the QD (rather than in its center as in the electron case) couple most strongly to the HH along the transverse direction – an effect which manifests itself directly in the appearance of a distinct minimum in the decoherence rate $1/T_2$ (see Fig. 6.1).

We now evaluate the second- and fourth-order self-energy in the continuum limit (changing sums to integrals), following Coish et al. (2010). Since $a_z \ll L$ (see above), we can perform a two-dimensional limit by averaging over the $z$-dependence in the hyperfine coupling constants $A_k^z$ and $A_k^\pm$. From Eq. (6.17), we see that the second-order self-energy $\Sigma^{(2)}$ is purely real, leading to no decay but a frequency shift $\Delta\omega = -\mathrm{Re}\Sigma^{(2)}(s+i\omega_n)$, or

$$\Delta\omega = \frac{c_+ + c_-}{16N}\,\frac{A_\perp^2}{\omega_n}, \tag{6.19}$$

where $N$ is the number of nuclear spins enclosed by the envelope function. The fourth-order self-energy becomes (see Appendix B.6)

$$\Sigma^{(4)}(s+i\omega_n) \simeq -i\frac{c_+c_-}{4N}\,\frac{A_\perp}{A_z}\,\frac{A_\perp^3}{\omega_n^2}\int_0^1 dx\int_0^1 dy\,\frac{x(\log x)^2\,y(\log y)^2}{s+i(x-y)} \tag{6.20}$$

in the continuum limit, where $x=\exp\{-r_1^2\}$, $y=\exp\{-r_2^2\}$, and $r_i=\sqrt{x_i^2+y_i^2}/L$ $(i=1,2)$. Here, we have approximated $|A_k^\pm|^2 \simeq |A_{k,\mathrm{CB}}^\pm|^2 + |A_{k,\mathrm{LH}}^\pm|^2$ since the overlap term vanishes under spatial averaging. The appearance of polynomial prefactors $r^4$, represented by the log functions in the numerator of Eq. (6.20), is a direct consequence of the excited-state envelope functions describing the distribution of transverse coupling constants $A_k^\pm$ within the quantum dot.

The transverse-spin dynamics of the HH are described by the non-analytic structure of the right-hand side of Eq. (6.16) (see also Chapter 4.4 and in particular Fig. 4.1). Inserting the self-energies $\Sigma^{(2)}$ and $\Sigma^{(4)}$ into Eq. (6.16), we find one pole at $s \simeq i\Delta\omega - \Gamma$, whose negative real part gives decoherence rate of the HH: $\Gamma = 1/T_2 \simeq -\mathrm{Im}\Sigma^{(4)}(i\omega_n + i\Delta\omega + 0^+)$ (see Chapter 4.4.3), where $0^+$ denotes a positive infinitesimal. Evaluating Eq. (6.20), we find

$$\frac{1}{T_2} = \frac{\pi c_+c_-}{4N}\,\frac{A_\perp}{A_z}\,\frac{A_\perp^3}{\omega_n^2}\int_\epsilon^1 dx\,x[\log x]^2(x+\epsilon)[\log(x+\epsilon)]^2, \tag{6.21}$$

where $\epsilon = N|\Delta\omega/A_{\mathrm{HH}}|$. The integral in Eq. (6.21) can now be evaluated numerically for any value of $\epsilon$ (i.e., of $\omega_n$).

In Fig. 6.1, we show the hole-spin decoherence rate $1/T_2$ as a function of the Zeeman energy $\omega_n = g_h\mu_B B + pIA_{\mathrm{HH}}$ ($0 \le p \le 1$ is the degree of nuclear-spin polarization). The non-monotonic

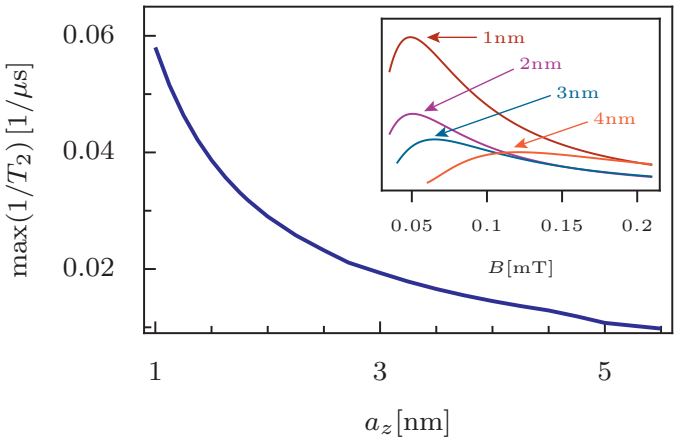


Figure 6.2: Maximum of the decoherence rate $1/T_2$ as a function of the QD height $a_z$. For increasing $a_z$, the maximal value of $1/T_2$ decreases (see main plot) and the position of the maximum is shifted (see inset).

behavior of $1/T_2$ for small $\omega_n$ appears when $\epsilon \propto 1/\omega_n$ approaches unity. We emphasize that the range of validity of this result is given by $\epsilon < 1$, which is much less restrictive than the condition $A_\perp/\omega_n < 1$ suggested by the self-energy expansion:

$$\epsilon = \frac{c_+ c_-}{16} \frac{A_\perp}{A_z} \frac{A_\perp}{\omega_n} \ll \frac{A_\perp}{\omega_n}. \tag{6.22}$$

For electrons, we have found non-monotonic behavior of $1/T_2$ as well (see Fig. 4.5), albeit with a different dependence on $\epsilon$ and around magnetic fields of several tesla. In contrast, for holes, the non-monotonicity occurs at much lower fields ($B \simeq 0.1$mT for the parameters used in Fig. 6.1), and the rate $1/T_2$ features an additional dip which is a footprint of the excited-state envelope functions appearing in Eq. (6.1). The huge difference in energy scales has very important consequences for the tunability of the hole-spin decoherence rate: by increasing the externally applied magnetic field (or the degree of nuclear-spin polarization), it is possible to decrease $1/T_2$ over many orders of magnitude within the experimentally accessible range of magnetic fields (see inset of Fig. 6.1). This means that this system offers the possibility to entirely 'turn off' hyperfine-associated spin decoherence. As a consequence, hole-spin quantum dots may be operated in a regime where other interactions, such as spin-orbit or direct nuclear dipole interactions, will be the dominant source of spin decoherence and will therefore become experimentally observable. We emphasize that Eq. (6.21) is still valid at $B = 0$, as long as $\epsilon < 1$ (i.e., for non-zero nuclear-spin polarization).

The degree of band hybridization, and therefore the decoherence rate $1/T_2$, depends on the geometry of the QD, i.e., on $L$ and $a_z$. For flat QDs the amount of LH admixture to the HH states (6.1) is decreased, leading to smaller non-Ising terms in the Hamiltonian (6.10). On the other hand, the envelope wavefunction of a flat dot encloses less nuclear spins (for fixed $L$). These two effects lead to an increase of the maximal decoherence rate for smaller $a_z$ (see Fig. 6.2), and a shift of its position as a function of $B$ (see inset of Fig. 6.2).

## 6.5 Conclusions

We have shown that in HH quantum dots, band hybridization leads to a hole-nuclear-spin coupling which is transverse to the growth axis of the semiconductor and which depends on the geometry of the QD. If the nuclear spins are prepared in a narrowed state, this transverse coupling induces an exponential hole-spin decoherence due to hyperfine-mediated nuclear-pair-flip processes. We have shown that the associated decoherence time $T_2$ can be tuned over many orders of magnitude by sweeping an external magnetic field from sub-millitesla to tesla ranges.

Chapter 7

# Electrons in Carbon Nanostructures

## 7.1 Introduction

In Chapter 1 we have discussed the idea of spin-based quantum computation and the related problem of short decoherence times, which are typically due to interactions with the ubiquitous nuclear spins. For III-V semiconductor quantum dots, with their high abundance of spin-carrying nuclear isotopes, the associated decoherence times are quite short, usually of order nanoseconds (Merkulov et al., 2002; Khaetskii et al., 2002; Coish and Loss, 2004; Petta et al., 2005), if no manipulations on the nuclear system are performed.

One way of overcoming the problem of short decoherence times is to build quantum dots from semiconductors with lower abundances of spin-carrying isotopes, potentially resulting in weaker nuclear-spin interactions. Carbon structures naturally consist of 99% $^{12}$C with nuclear spin 0 and only of 1% $^{13}$C with nuclear spin $\frac{1}{2}$, and are therefore promising materials for building quantum dots featuring long spin decoherence times. This extraordinary property of carbon materials, as well as their comparatively weak spin-orbit interactions, has led to proposals of fabricating quantum dots in graphene ribbons with armchair boundaries (Trauzettel et al., 2007) and in carbon nanotubes (CNTs) (Bulaev et al., 2008).

Although it was not yet possible to experimentally realize a single-electron quantum dot in graphene, Coulomb-blockade measurements in gated graphene quantum dots have already been carried out successfully (Schnez et al., 2009; Ponomarenko et al., 2008). Experiments on single electrons in CNTs have advanced even more (Tans et al., 1997; Bockrath et al., 1997; Kong et al., 2000; Minot et al., 2004; Jarillo-Herrero et al., 2004; Mason et al., 2004; Biercuk et al., 2005; Cao et al., 2005; Sapmaz et al., 2006; Onac et al., 2006; Gräber et al., 2006; Jørgensen et al., 2006; Meyer et al., 2007; Kuemmeth et al., 2008; Steele et al., 2009). Very recently, first measurements on nuclear-spin interactions and electron-spin dynamics in CNTs have been performed by Churchill et al. (2009a,b), reporting an unexpectedly strong hyperfine interaction of order $A \simeq 100\,\mu e$V in $^{13}$C enriched CNTs. Furthermore, theoretical and experimental NMR studies on fullerenes (Pennington and Stenger, 1996) have been carried out as well as *ab initio* calculations on hyperfine interaction in small graphene flakes (Yazyev, 2008).

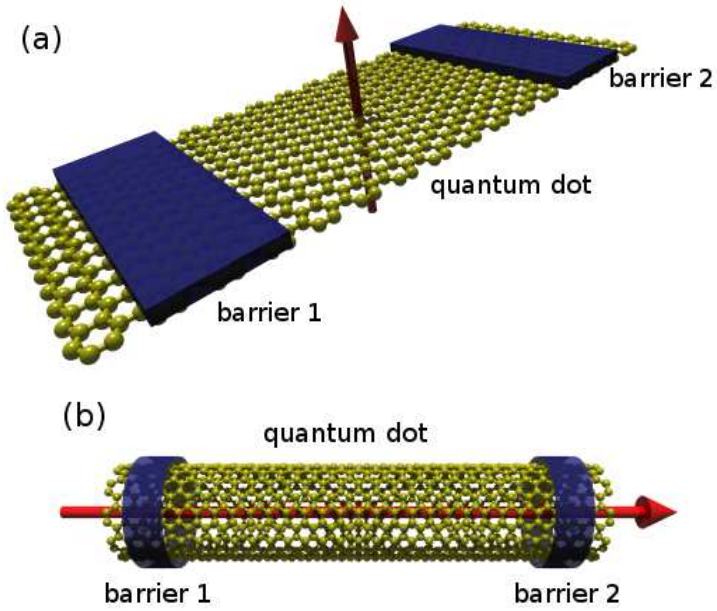


Figure 7.1: Sketch of the systems under consideration throughout this work: (a) a single electron confined to a quantum dot defined by two barriers on a graphene ribbon; (b) a single-electron quantum dot defined in a carbon nanotube. Externally applied magnetic fields are indicated by the red arrows.

In this chapter we analytically calculate the interaction of a single electron confined to a graphene ribbon or a CNT (see Fig. 7.1) with the spins of the surrounding $^{13}$C nuclei. For CNTs we find an interesting interplay between isotropic and anisotropic hyperfine interactions which depends on the CNT geometry and which leads to a highly anisotropic Knight shift and an unusual alignment of the nuclear spins around a CNT circumference (in the ground state). Furthermore, we calculate the decoherence dynamics of the electron spin and find that, even without manipulating the nuclear spins, the hyperfine-associated decoherence times can be on the order of tens of microseconds or longer, depending on the relative abundance of $^{13}$C nuclei. These timescales are much longer than the ones typically found for III-V semiconductor quantum dots, making carbon-based quantum dots promising spin-qubit candidates.

## 7.2 Bonds and bands

The carbon atom features six electrons: two core electrons and four valence electrons. In a solid, the four valence electrons (which are in $2s$ and $2p$ states) form the bonds with the nearest-neighbor atoms. In two-dimensional graphite, or graphene, each atom has three nearest neighbors, and three of the four valence electrons form $sp^2$-hybridized bonds (called $\sigma$-bonds) with those neighbors, while the fourth electron is in a so-called $\pi$-state perpendicular to the $\sigma$-bonds (Saito et al., 1998). The $\pi$-electrons in graphene determine the band structure near the Fermi energy, while the $\sigma$-electrons form more remote bands. A conduction-band electron

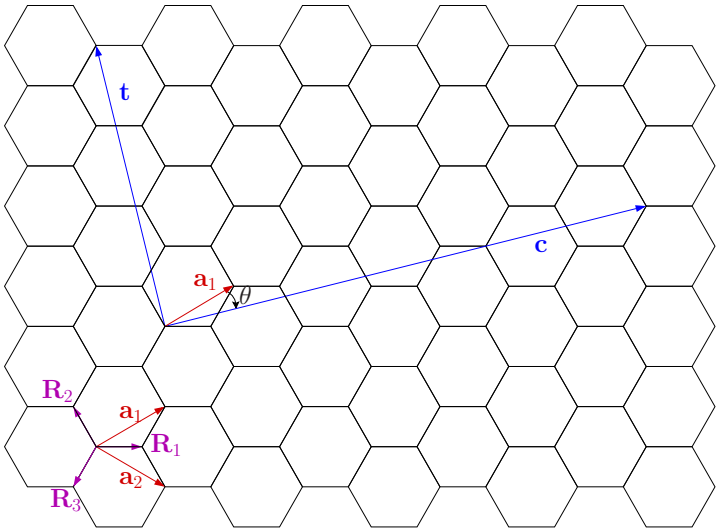


Figure 7.2: Definitions used throughout this work: $\mathbf{a}_1$ and $\mathbf{a}_2$ denote the basis vectors of the honeycomb lattice, $\mathbf{R}_j$ are the relative nearest-neighbor positions, $\mathbf{c}$ and $\mathbf{t}$ are the circumferential and transverse vectors, respectively, and $\theta = \theta_{nm}$ is the chiral angle between $\mathbf{c}$ and $\mathbf{a}_1$.

is therefore in a $\pi$-state.

A CNT can be regarded as a graphene sheet that had been rolled up along some direction $\mathbf{c}$, defining a symmetry axis $\mathbf{t}$ of the CNT. The circumferential and translational vectors are defined in terms of the basis vectors $\mathbf{a}_1$ and $\mathbf{a}_2$ as (see Fig. 7.2)

$$\mathbf{c} = n\mathbf{a}_1 + m\mathbf{a}_2, \quad \mathbf{t} = t_1\mathbf{a}_1 + t_2\mathbf{a}_2. \tag{7.1}$$

Here, $n, m \in \mathbb{N}_0$ are the chiral indices, and $t_1 = (2m+n)/d_R$, $t_2 = -(2n+m)/d_R$ with $d_R$ being the greatest common divisor of $2n+m$ and $2m+n$. We denote the chiral angle between $\mathbf{c}$ and $\mathbf{a}_1$ by $\theta = \theta_{nm}$.

The curvature of the CNT causes a geometrical tilting of the $\sigma$-bonds which results in an *sp*-hybridization of the conduction-band states. Kleiner and Eggert (2001) have studied this effect perturbatively in lowest order in the small parameter $2\pi/L$, where $L = \sqrt{n^2+nm+m^2}$ is the circumference of the CNT in units of the lattice constant $a \simeq 2.5\,\text{Å}$. For typical CNTs we have $2\pi/L < 1$. However, the parameter can approach unity for ultra-small nanotubes. At this point, our theory breaks down.

The wavefunction of a conduction-band electron in a periodic crystal is given by Bloch's theorem: $\Psi_{\mathbf{k}\sigma} = \frac{1}{\sqrt{N_A}} e^{i\mathbf{k}\cdot\mathbf{r}} u_{\mathbf{k}\sigma}(\mathbf{r})$, where $N_A$ is the number of atomic sites in the crystal and the Bloch amplitude $u_{\mathbf{k}\sigma}(\mathbf{r})$ has the periodicity of the lattice. Similar to our treatment of heavy holes in Chapter 5, we approximate the Bloch amplitude $u_{\mathbf{k}\sigma}(\mathbf{r})$ at the K and K' points (the minima of the conduction band) by a linear combination of hydrogenic orbitals, $u_\sigma(\mathbf{r}) = \sum_{\mathbf{R}} \pi(\mathbf{r}-\mathbf{R})$, where (Kleiner and Eggert, 2001)

$$\pi(\mathbf{r}) = N_{nm}\Big\{\psi_{2p_\perp}(\mathbf{r}) + \frac{\pi}{2\sqrt{3}L}\Big(\psi_{2s}(\mathbf{r}) + \sin(3\theta'_{nm})\psi_{2p_t}(\mathbf{r}) + \cos(3\theta'_{nm})\psi_{2p_c}(\mathbf{r})\Big)\Big\}, \tag{7.2}$$

and the sum runs over all lattice sites in the CNT. In the above, $\psi_{2s}$ represents a hydrogenic $2s$ orbital, $\psi_{2p_t}$, $\psi_{2p_c}$ and $\psi_{2p_\perp}$ are, respectively, the $2p$ orbitals along the transverse, circumferential, and radial direction of the CNT, and $N_{nm}$ normalizes the Bloch amplitude to two atoms per unit cell. $\theta'_{nm}$ is the angle between $\mathbf{c}$ and $\mathbf{R}_1$, and we can write $\sin(3\theta'_{nm}) = (n-m)(2n^2+5nm+2m^2)/2L^3$ and $\cos(3\theta'_{nm}) = 3\sqrt{3}nm(n+m)/2L^3$ in terms of the chiral indices (Kleiner and Eggert, 2001). The hydrogenic orbitals consist of a radial and an angular part, e.g., $\psi_{2s}(\mathbf{r}) = R_{20}(r)Y_0^0(\vartheta,\varphi)$. We will choose a local coordinate system at each lattice site, such that $\psi_{2p_t}$, $\psi_{2p_c}$, and $\psi_{2p_\perp}$ correspond to hydrogenic $2p$ orbitals in $z$-, $y$-, and $x$-direction, respectively (see below). The radial components of the hydrogenic orbitals depend on an effective screened nuclear charge $Z_{\text{eff}}$ 'seen' by the electron (Clementi and Raimondi, 1963).

Our choice of the Bloch amplitude implicitly assumes that the electron is tightly bound to the nuclei, i.e., that the radial component of $\pi(\mathbf{r})$ drops off fast on the scale of the nearest-neighbor distance. We have estimated that $|\pi(\mathbf{r}+\mathbf{R}_{\text{n.n.}})|^2/|\pi(\mathbf{r})|^2 \simeq 10^{-3}$ for any nearest-neighbor lattice vector $\mathbf{R}_{\text{n.n.}}$, justifying our assumption.

In a quantum dot, the electron is delocalized over many lattice sites and its Bloch amplitude is modulated by an envelope function $\Phi_\sigma$ defined by the confinement potential (see Bulaev et al. (2008) for the envelope function of a quantum dot defined by a rectangular confinement potential in a semiconducting CNT). Including the spin states $|\sigma\rangle = |\uparrow,\downarrow\rangle$, we write the electron states as

$$|\Psi_\sigma\rangle = |\Phi_\sigma; u_\sigma\rangle|\sigma\rangle, \tag{7.3}$$

where, in the envelope-function approximation, $\langle\mathbf{r}|\Phi_\sigma; u_\sigma\rangle = \Phi_\sigma(\mathbf{r})u_\sigma(\mathbf{r})$. Since we did not include spin-orbit interactions in our model, the orbital wavefunction is independent of the spin state, and we may omit the subscript $\sigma$: $\Phi_\sigma(\mathbf{r}) = \Phi(\mathbf{r})$ and $u_\sigma(\mathbf{r}) = u(\mathbf{r})$.

## 7.3 Nuclear-spin interactions

### 7.3.1 Carbon nanotubes

As we have seen in Chapter 2.2, there are three terms that couple the spin of the confined electron to the nuclear spins in the CNT: the Fermi contact interaction, the anisotropic hyperfine interaction and the coupling of electron orbital angular momentum to the nuclear spins. These interactions are represented by the Hamiltonians

$$h_1^k = \frac{\mu_0}{4\pi}\frac{8\pi}{3}\gamma_S\gamma_{j_k}\,\delta(\mathbf{r}_k)\,\mathbf{S}\cdot\mathbf{I}_k, \tag{7.4}$$

$$h_2^k = \frac{\mu_0}{4\pi}\gamma_S\gamma_{j_k}\frac{3(\mathbf{n}_k\cdot\mathbf{S})(\mathbf{n}_k\cdot\mathbf{I}_k)-\mathbf{S}\cdot\mathbf{I}_k}{r_k^3(1+d/r_k)}, \tag{7.5}$$

$$h_3^k = \frac{\mu_0}{4\pi}\gamma_S\gamma_{j_k}\frac{\mathbf{L}_k\cdot\mathbf{I}_k}{r_k^3(1+d/r_k)}, \tag{7.6}$$

respectively, where $\gamma_S = 2\mu_B$, $\gamma_{j_k} = g_{j_k}\mu_N$, $\mu_B$ is the Bohr magneton, $g_{j_k}$ is the nuclear g-factor of isotopic species $j_k$, $\mu_N$ is the nuclear magneton, $\mu_0$ is the vacuum permeability, $\mathbf{r}_k = \mathbf{r}-\mathbf{R}_k$ is the electron-spin position operator relative to the nucleus, $d \simeq Z\times 1.5\times 10^{-15}$ m is a length

of nuclear dimensions, $Z$ is the charge of the nucleus, and $\mathbf{n}_k = \mathbf{r}_k/r_k$. $\mathbf{S}$ and $\mathbf{L}_k = \mathbf{r}_k \times \mathbf{p}$ denote the spin and orbital angular-momentum operators (with respect to the $k^{\text{th}}$ nucleus) of the electron, respectively. The cutoff $1 + d/r_k$ comes from the Dirac equation (see Chapter 2.2) and avoids unphysical divergences from expectation values of the Hamiltonians $h_2^k$ and $h_3^k$. In the problem considered here, this cutoff may be omitted for the following reasons: (i) The expectation values of $h_2^k$ and $h_3^k$ with respect to an $s$-state vanish identically due to the spherical symmetry of the wavefunction and the vanishing orbital angular momentum, respectively. The expectation values with respect to a $p$-state are non-zero, but the $p$-wavefunction goes to zero sufficiently fast at the position of each nucleus, thus avoiding a divergence. (ii) As mentioned above, the electron wavefunction does not extend significantly to the nearest-neighbor lattice sites. Hence, within our tight-binding approximation, the orbital $\pi(\mathbf{r})$ centered around some nucleus cannot cause a divergence at the position of a nearest neighbor.

We note that the orbital angular momentum $\mathbf{L}_k$ which appears in Eq. (7.6) is associated with the electronic motion around the $k^{\text{th}}$ nucleus and is described by the Bloch part of the electron wavefunction. On the other hand, it has been shown by Latil et al. (2001), that interatomic currents can occur along the nanotube circumference to which another orbital angular momentum $\mathcal{L}$ may be associated which is described by the envelope part of the electron wavefunction. However, the hyperfine coupling strength is defined via the Bloch part of the electron wavefunction and therefore a consideration of the coupling between the valley degrees of freedom via envelope-function-associated angular momenta is beyond the scope of the analysis presented here.

We will consider CNTs and graphene with different abundances of the nuclear isotopes $^{12}$C and $^{13}$C. While $^{12}$C does not carry a nuclear spin, the nuclear gyromagnetic ratio of $^{13}$C is non-vanishing and given by $\gamma_{^{13}\text{C}} = 7.1 \times 10^{-27}$ J/T.

The Fermi contact interaction (7.4) yields a finite contribution for $s$-states, but vanishes for $p$-states. The anisotropic hyperfine interaction (7.5) and the coupling of orbital angular momentum (7.6) vanish for $s$-states because of their spherical symmetry and zero orbital angular momentum, but yield a finite contribution for $p$-states. Therefore, when considering CNTs, all three interactions (7.4) - (7.6) have to be taken into account because of the $sp$-hybridized electron states (7.2), while for graphene, only the interactions (7.5) and (7.6) are relevant, due to the purely $p$-type wavefunction (corresponding to the limit $n, m \to \infty$ in Eq. (7.2)).

We first calculate matrix elements of the interactions (7.4) - (7.6) with respect to the electron wavefunction (7.3), which will lead to effective spin Hamiltonians and to the associated coupling strengths in the CNT case. Throughout this section, we will consider a CNT that consists only of spin-carrying $^{13}$C isotopes. The possibility of different nuclear isotope abundances will then be taken into account in Sec. 7.5. From the CNT results, it will be possible to perform the 'graphene limit', which we postpone to Sec. 7.3.2.

We start with the Fermi contact interaction and calculate

$$\langle \Psi_\sigma | h_1^k | \Psi_{\sigma'} \rangle = \frac{2\mu_0 \gamma_S \gamma_{^{13}\text{C}}}{3} \sum_k |u(\mathbf{r}_k)|^2 |\Phi(\mathbf{r}_k)|^2 \langle \sigma | \mathbf{S} \cdot \mathbf{I}_k | \sigma' \rangle, \tag{7.7}$$

assuming that the electron-spin density does not depend on the lattice site, which is justified if,

e. g., the envelope function $\Phi(\mathbf{r})$ describes the ground state of the quantum dot. The effects of a site dependence of the electron-spin density have recently been considered by Pályi and Burkard (2009). Evaluating the spin matrix elements leads to the following effective spin Hamiltonian:

$$H_1 = \sum_k A_k^{(1)} \mathbf{S} \cdot \mathbf{I}_k, \tag{7.8}$$

with coupling constants $A_k^{(1)} = A_1 v_0 |\Phi(\mathbf{r}_k)|^2$ (where $v_0$ is the volume of a primitive unit cell) and the associated coupling strength

$$A_1 = \frac{\mu_0 \gamma_S \gamma_{^{13}\mathrm{C}} Z_{\mathrm{eff}}^3}{3\pi a_0^3} N_{nm}^2 \beta_{nm}^2, \tag{7.9}$$

where we have introduced $\beta_{nm} = \pi/2\sqrt{3}L$, and $a_0$ is the Bohr radius. The normalization factor $N_{nm}$ can be determined by normalizing Eq. (7.2) to two atoms per unit cell:

$$N_{nm} = 2\sqrt{\frac{L^2}{\pi^2 + 4L^2}}. \tag{7.10}$$

We have evaluated Eq. (7.9) for CNTs of different chiralities in Table 7.1. For typical CNTs, the coupling strength $A_1$ is about three orders of magnitude smaller than that for an electron in a GaAs quantum dot ($A_1^{\mathrm{GaAs}} \simeq 90\mu e\mathrm{V}$, see Paget et al. (1977)), for two reasons: (i) The hybridization prefactor $N_{nm}\beta_{nm}$ is on the order of 0.05 and enters quadratically into $A_1$. (ii) The effective nuclear charge (which enters in third power into $A_1$) is $Z_{\mathrm{eff}}^{\mathrm{C}} \simeq 3.2$ for carbon, but $Z_{\mathrm{eff}}^{\mathrm{Ga}} \simeq 7.1$ for gallium and $Z_{\mathrm{eff}}^{\mathrm{As}} \simeq 8.9$ for arsenic (Clementi and Raimondi, 1963).

The sign of the isotropic interaction is positive for all nanotube diameters, in contrast to results reported previously by Semenov et al. (2007), where spin relaxation of conduction electrons has been calculated numerically and a sign change of the hyperfine coupling constant $A_1$ has been found for small nanotube diameters. This is due to the fact that Semenov et al. (2007) have included the coupling of the $1s$ core electrons to the nuclear spins, which, however, is irrelevant for the hyperfine interaction of a conduction electron and, hence, for the electron spin dephasing considered here.

Now we look at the anisotropic hyperfine interaction. Due to symmetry, the $s$-part of the hybridized wavefunction does not contribute. Taking matrix elements $\langle \Psi_\sigma | h_2^k | \Psi_{\sigma'} \rangle$ just like above, we arrive at an effective Hamiltonian

$$H_2 = \sum_k \Big( A_k^{(2,x)} S^x I_k^x + A_k^{(2,y)} S^y I_k^y + A_k^{(2,z)} S^z I_k^z \Big), \tag{7.11}$$

with coupling constants $A_k^{(2,j)} = A_2^j v_0 |\Phi(\mathbf{r}_k)|^2$ and the coupling strengths

$$A_2^j = \frac{\mu_0 \gamma_S \gamma_{^{13}\mathrm{C}} Z_{\mathrm{eff}}^3}{120\pi a_0^3} N_{nm}^2 \lambda_j, \tag{7.12}$$

where

$$\lambda_x = 1 - \frac{1}{2}\beta_{nm}^2, \tag{7.13}$$

$$\lambda_y = -\frac{1}{2} - \frac{1}{2}\beta_{nm}^2 \sin^2(3\theta'_{nm}) + \beta_{nm}^2 \cos^2(3\theta'_{nm}), \tag{7.14}$$

$$\lambda_z = -\frac{1}{2} + \beta_{nm}^2 \sin^2(3\theta'_{nm}) - \frac{1}{2}\beta_{nm}^2 \cos^2(3\theta'_{nm}). \tag{7.15}$$

| | $(10,0)$ | $(20,0)$ | $(5,10)$ | $(9,15)$ | $(5,5)$ | $(10,10)$ | $(20,20)$ |
|---|---|---|---|---|---|---|---|
| $A_1$ | 0.19 | 0.05 | 0.12 | 0.05 | 0.26 | 0.07 | 0.02 |
| $A_2^x$ | 0.59 | 0.60 | 0.59 | 0.60 | 0.58 | 0.60 | 0.61 |
| $A_2^y$ | $-0.29$ | $-0.30$ | $-0.30$ | $-0.30$ | $-0.29$ | $-0.30$ | $-0.30$ |
| $A_2^z$ | $-0.30$ | $-0.30$ | $-0.30$ | $-0.30$ | $-0.30$ | $-0.30$ | $-0.30$ |

Table 7.1: Estimated hyperfine coupling strengths (in $\mu e$V) for nanotubes of different chiralities $(n,m)$.

We see that the coupling induced by the anisotropic hyperfine interaction is different in all three spatial directions. Recall that we have labeled our axes such that $z$, $y$, and $x$ refer to the translational, circumferential, and radial directions, respectively. We show typical values for $A_2^j$ in Table 7.1. The direction of strongest hyperfine interaction is radial to the nanotube. The fact that $A_2^x \simeq -2A_2^y \simeq -2A_2^z$ for the CNTs in Table 7.1 comes directly from the angular integration in the expressions $\langle\Psi_\sigma|h_2^k|\Psi_{\sigma'}\rangle$, leading to Eq. (7.11): the admixture of $\psi_{2p_t}$ and $\psi_{2p_c}$ to the $\pi$-orbital in Eq. (7.2) is very small, such that the integration approximately reduces to the $\psi_{2p_\perp}$ term (the $\psi_{2s}$ term does not contribute by symmetry). It is interesting to note the competing signs: the Fermi contact interaction (expressed via $A_1$) enhances the anisotropic hyperfine interaction along the radial direction, but reduces it along the circumferential and transverse directions. Furthermore, the signs of the hyperfine coupling along different directions indicate ferro- and antiferromagnetic alignment of the nuclear spins with respect to the electron spin (in the ground state). We will come back to this in Sec. 7.4.

Finally, we address the coupling of electron orbital angular momentum. Calculating matrix elements of $h_3^k$, it is straightforward to see that this interaction vanishes identically by applying the operators $L_j$ to the hydrogenic orbitals appearing in Eq. (7.2), then evaluating $\langle\Psi_\sigma|h_3^k|\Psi_{\sigma'}\rangle$ and summing up all contributions.

### 7.3.2 Graphene

We consider the 'graphene limit' corresponding to let $n,m\to\infty$ in all expressions in Sec. 7.3.1. Then $\beta_{nm}\to 0$ and $N_{nm}\to 1$ and, denoting quantities related to graphene with a tilde,

$$\tilde{A}_1 = 0, \quad \tilde{A}_2^z = \tilde{A}_2^y = -\frac{\tilde{A}_2^x}{2} = -\frac{\mu_0\gamma_S\gamma_{^{13}\mathrm{C}}Z_{\mathrm{eff}}^3}{240\pi a_0^3}. \tag{7.16}$$

Inserting numbers, this yields $\tilde{A}_2^z = \tilde{A}_2^y \simeq -0.3\,\mu e$V and $\tilde{A}_2^x \simeq 0.6\,\mu e$V. Note that in our notation the $x$-direction is perpendicular to the graphene plane.

Surprisingly, these numbers are not much different from those estimated for $A_2^j$ in Sec. 7.3.1. Naively, one might have expected a weaker hyperfine interaction in graphene (as compared to CNTs) due to its flatness and the vanishing contact interaction (7.4). As it turns out, however, even for small CNTs the contact interaction is only a small correction to the anisotropic hyperfine interaction (7.5), so that the latter is the main hyperfine contribution for both CNTs and flat graphene.

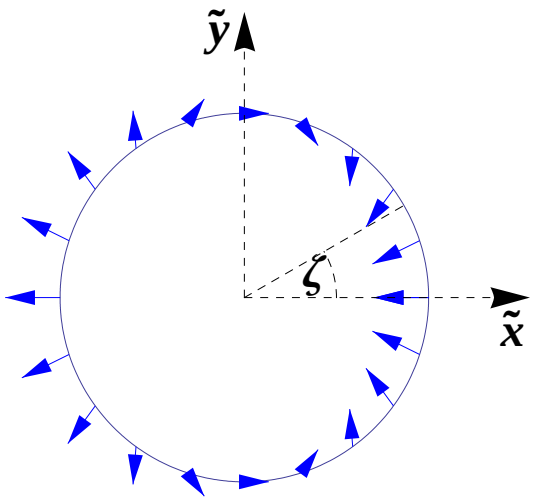


Figure 7.3: Alignment of the nuclear spins (in the ground state) due to the anisotropic Knight shift. The electron is assumed to be prepared in the eigenstate of $S^{\tilde{x}}$ with eigenvalue $+1/2$, see Eq. (7.19), and points along $\tilde{x}$ at each nuclear-spin site.

## 7.4 Hyperfine-induced anisotropic Knight shift

In Secs. 7.2 and 7.3, we have formulated the hyperfine problem in terms of a local coordinate system at each nucleus. In this section, we want to look at the Knight shift of the $^{13}$C nuclear spins due to hyperfine interaction with the conduction electron. The isotropic Knight shift due to interaction with both the *sp*-hybridized conduction-band electron and the 1*s* core electron has been studied by Yazyev and Helm (2005). Electron-spin resonance spectra of $^{13}$C in $\pi$-electron radicals have been analyzed by Karplus and Fraenkel (1961).

From our considerations in Sec. 7.3.1 it is clear that the Knight shift induced by the anisotropic hyperfine interaction ($\sim A_2^j/N$) exceeds the isotropic Knight shift ($\sim A_1/N$) by roughly one order of magnitude ($N$ is the number of nuclei in the dot). The Knight shift in CNTs (and graphene) is therefore highly anisotropic.

We introduce the following global coordinate system: $\tilde{x} = x\cos\zeta - y\sin\zeta$, $\tilde{y} = x\sin\zeta + y\cos\zeta$, $\tilde{z} = z$, such that the $\tilde{x}\tilde{y}$-plane cuts out a cross section of the CNT and $\zeta$ is the coordinate describing the position on this cross section (see Fig. 7.3).

The electron is assumed to be prepared in a fixed state and to be delocalized over the CNT cross section. At each lattice point occupied by a $^{13}$C nucleus, the nuclear spin will align itself in such a way that the hyperfine energy is minimized in the ground state of the nuclear spins. This ground state can only be achieved for temperatures that are small with respect to the energies associated with the Knight shift: $k_BT < (A_1 + A_2^j)/N \sim 1\,\mathrm{peV} \ldots 1\,\mathrm{neV}$, where $k_B$ is the Boltzmann constant. We write the Hamiltonian describing the hyperfine interaction of one

nucleus with the delocalized electron as

$$H'_{\rm hf} = \mathbf{S}^T \mathcal{A}\, \mathbf{I} = \tilde{\mathbf{S}}^T \tilde{\mathcal{A}}\, \tilde{\mathbf{I}}, \tag{7.17}$$

where $\mathbf{S}^T = (S^x, S^y, S^z)$, $\mathcal{A} = \mathrm{diag}(A^x, A^y, A^z)$, $\mathbf{I} = (I^x, I^y, I^z)^T$, $\tilde{\mathbf{S}}^T = \mathbf{S}^T R^\dagger$, $\tilde{\mathcal{A}} = R\mathcal{A}R^\dagger$, and $\tilde{\mathbf{I}} = R\,\mathbf{I}$, with the rotation $R$ given by

$$R = \begin{pmatrix} \cos\zeta & -\sin\zeta & 0 \\ \sin\zeta & \cos\zeta & 0 \\ 0 & 0 & 1 \end{pmatrix}. \tag{7.18}$$

The operators carrying a tilde hence describe the interaction in the global coordinate system $(\tilde{x}, \tilde{y}, \tilde{z})$, and the coupling tensor is given by

$$\tilde{\mathcal{A}} = \begin{pmatrix} A_x \cos^2\zeta + A_y \sin^2\zeta & (A_x - A_y)\sin\zeta\,\cos\zeta & 0 \\ (A_x - A_y)\sin\zeta\,\cos\zeta & A_x \cos^2\zeta + A_y \sin^2\zeta & 0 \\ 0 & 0 & A_z \end{pmatrix}.$$

Here, $A_j = A_1 + A_2^j$ is the sum of isotropic and anisotropic hyperfine couplings along the (local) $j$-direction ($j = x, y, z$), see Eqs. (7.9) and (7.12). Recall that $A_x > 0$ and $A_y, A_z < 0$ for CNTs (see Sec. 7.3.1). For an electron spin in an eigenstate of $S^{\tilde{x}}$, the interaction reads

$$H_{\rm hf}^{\tilde{x}} = (A_{\tilde{x}\tilde{x}} I^{\tilde{x}} + A_{\tilde{x}\tilde{y}} I^{\tilde{y}}) S^{\tilde{x}} \tag{7.19}$$

with $A_{\tilde{x}\tilde{x}} = A_x \cos^2\zeta + A_y \sin^2\zeta$ and $A_{\tilde{x}\tilde{y}} = (A_x - A_y)\sin\zeta\,\cos\zeta$.

In Fig. 7.3 we show the alignment of the nuclear spins (assuming the nuclear spins to be in their ground state) due to the anisotropic Knight shift induced by the hyperfine interaction with a conduction electron whose spin is prepared in the eigenstate of $S^{\tilde{x}}$ with eigenvalue $+1/2$, i.e., pointing along the $\tilde{x}$-direction at each nuclear site. We have assumed that the electron is evenly distributed around the CNT cross section, which can be seen to be justified from the envelope functions calculated by Bulaev et al. (2008) for semiconducting CNTs subject to a rectangular confinement potential. We observe an interesting interplay between ferro- and antiferromagnetic coupling along the two spatial directions, which is a direct consequence of the CNT geometry and the strong anisotropy of the hyperfine interaction. In particular, the hyperfine interaction does not vanish when we average over the CNT circumference. This could lead to other interesting effects. For instance, it has been shown by Braunecker et al. (2009a,b) that in a Luttinger liquid, a non-vanishing average hyperfine field can lead to a transition into a helically ordered phase (along the tube axis) of the nuclear spins below some critical temperature.

## 7.5 Electron-spin decoherence

### 7.5.1 Carbon nanotubes

Based on our analysis in Sec. 7.3, the electron-spin dynamics in a CNT are described by the following hyperfine Hamiltonian:

$$H_{\rm hf} = \mathbf{h} \cdot \mathbf{S}, \quad h_j = \sum_k A_k^j I_k^j, \tag{7.20}$$

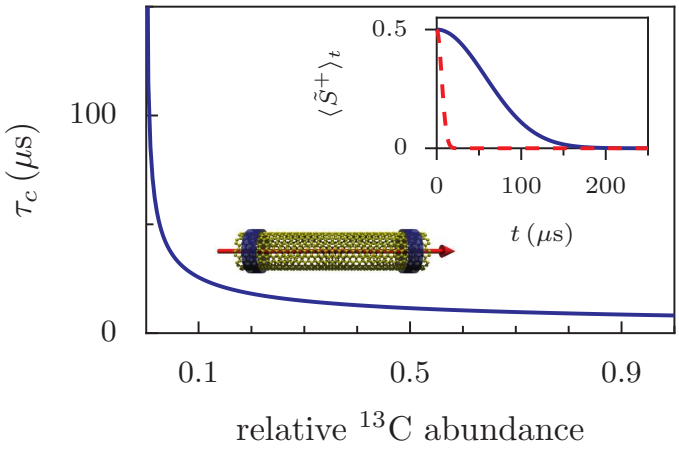


Figure 7.4: Electron-spin decoherence time $\tau_c$ in a (20,0) CNT as a function of the relative $^{13}$C abundance $N_{13}/N$, under the condition of a magnetic field $B_z \gtrsim 5\,\mathrm{mT}$ along the symmetry axis of the CNT. We have chosen a completely unpolarized nuclear system ($p = 0$) and $N = 6 \times 10^5$, see text below Eq. (7.23). Inset: Electron-spin dynamics in CNTs with $^{13}$C abundances of 1% (solid blue curve) and 99% (dashed red curve), in the frame rotating with $\omega + pN_{13}$, see Eq. (7.22).

where $A_k^j = A_j v_0 |\Phi(\mathbf{r}_k)|^2$ and $A_j = A_1 + A_2^j$, see Eqs. (7.9) and (7.12).

We assume that an external magnetic field $B_z$ has been applied along the symmetry axis of the CNT (see Fig. 7.1 (b)), and that the induced Zeeman splitting between the spin states is larger than the hyperfine coupling strength: $b = g\mu_B B_z > A_j$. Assuming $g \simeq 2$, this corresponds to very moderate fields of $B_z \gtrsim 5\,\mathrm{mT}$. Within this limit, relaxation-induced decoherence is suppressed by the small parameter $A_j/b$, and the main source of decoherence is pure dephasing due to nuclear-field fluctuations along the CNT symmetry axis. The relevant Hamiltonian is given by the $z$-part of Eq. (7.20) and the Zeeman term:

$$H = (b + h_z) S^z. \tag{7.21}$$

Assuming that all nuclei carry non-zero spin, the dynamics of the transverse spin is then given by a Gaussian decay with timescale given by $\sqrt{N}/A_z$, where $N$ is the total number of nuclear spins in the quantum dot (Coish and Loss, 2004).

One advantage of carbon-based nanostructures is the low natural abundance of the spin-carrying isotope $^{13}$C. In order to investigate this advantage, we allow for arbitrary $^{13}$C abundances: we denote the total number of nuclei in the quantum dot (defined via the envelope function, see below) by $N$, and by $N_{12}$ and $N_{13}$ the number of $^{12}$C and $^{13}$C nuclei, respectively, such that $N = N_{12} + N_{13}$. This generalization has two relevant effects: (i) Summing over all $N$ nuclei, we get $\sum_k A_k^z = \eta A_z$, i.e., the total hyperfine coupling is weakened by the ratio $\eta = N_{13}/N$. (ii) The polarization $p$ of the nuclear-spin system ($0 \le p \le 1$) is determined only by the distribution of spin-up and spin-down $^{13}$C nuclei, while being unaffected by the $^{12}$C nuclei.

For $N_{13} \gg 1$ we can use the central limit theorem (compare with Coish and Loss (2004)) which yields the following Gaussian dynamics for the transverse electron spin (written in the frame rotating with frequency $(\omega + p\eta A_z/2)/\hbar$, where $\omega = b - b_N$ with the nuclear Zeeman energy $b_N = g_N \mu_N B_z$):

$$\langle S^+ \rangle_t = \langle S^+ \rangle_0 \, e^{-t^2/\tau_c^2}. \tag{7.22}$$

Here, $S^+ = S^x + iS^y$, with the electron-spin operators $S^j = \sigma_j/2$ and the Pauli operators $\sigma_j$. The characteristic timescale for the decay is given by (Coish and Loss, 2004)

$$\tau_c = \frac{2\hbar}{\sqrt{1-p^2}} \frac{N}{\sqrt{N_{13}} A_z}. \tag{7.23}$$

We can see from Eq. (7.23) that the decoherence time $\tau_c$ has an interesting non-linear dependence on the abundance of $^{13}$C nuclei.

The total number $N$ of nuclei in the quantum dot is determined by the quantum-dot confinement. Assuming a rectangular confinement along the symmetry axis (Bulaev et al., 2008) and a (20,0) CNT of length 300 nm, we estimate $N \simeq 6 \times 10^5$. We show the electron-spin decoherence time $\tau_c$ as a function of the relative $^{13}$C abundance in Fig. 7.4 for a completely unpolarized nuclear bath ($p = 0$). We see that decoherence times of several tens of microseconds can be expected for higher $^{13}$C abundances. For the natural $^{13}$C abundance of about 1%, we estimate $\tau_c \gtrsim 200\,\mu$s from Eq. (7.23). The inset of Fig. 7.4 shows the Gaussian decay of the spin coherence (Eq. 7.22) for CNTs containing 1% (solid line) and 99% (dashed line) $^{13}$C nuclei. We note that further increase of the decoherence time $\tau_c$, say by a factor of $x$, would require isotopic purification and the reduction of the natural $^{13}$C abundance by about a factor of $x^2$. The decoherence law in Eqs. (7.22) and (7.23) of course breaks down at the point when only a few nuclear spins are present in the dot.

### 7.5.2 Graphene

For an electron confined to a graphene quantum dot, the contact interaction vanishes identically ($\tilde{A}_1 = 0$, see Eq. (7.16)), and only the anisotropic hyperfine interaction contributes to spin decoherence. We assume an externally applied magnetic field $B_x$ perpendicular to the graphene plane (see Fig. 7.1 (a)), giving rise to a Zeeman splitting $\tilde{b} = g_\perp \mu_B B_x$, where $g_\perp \simeq 2$ is the electron g-factor in the out-of-plane direction. If the Zeeman splitting is much larger than the energy associated with the transverse hyperfine terms, $\tilde{b} \gg \tilde{A}_2^z, \tilde{A}_2^y$, the electron-spin dynamics are governed by a Gaussian decay similar to the CNT case (7.22), but with a characteristic timescale given by

$$\tilde{\tau}_c = \frac{2\hbar}{\sqrt{1-p^2}} \frac{N}{\sqrt{N_{13}} \tilde{A}_2^x}. \tag{7.24}$$

For a quantum dot with width $W = 30$ nm and length $L = 30$ nm, we estimate the total number of nuclei to be $N \simeq 4 \times 10^5$. We show $\tilde{\tau}_c$ as a function of the relative $^{13}$C abundance in Fig. 7.5: for higher $^{13}$C abundances, decoherence times $\tilde{\tau}_c \gtrsim 1\mu$s can be expected, while for the natural $^{13}$C abundance of 1%, we estimate $\tilde{\tau}_c \gtrsim 80\mu$s.

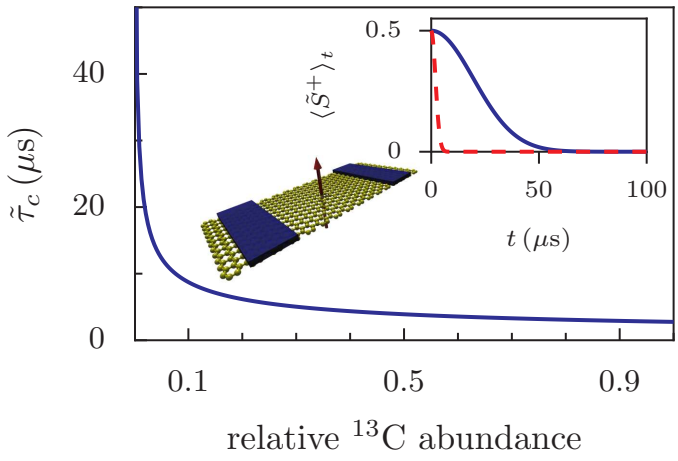


Figure 7.5: Electron-spin decoherence time $\tau_c$ in graphene as a function of the relative $^{13}$C abundance $N_{13}/N$, under the condition of a magnetic field $B_x \gtrsim 5\,\mathrm{mT}$ perpendicular to the graphene plane. We have chosen $p = 0$ and $N = 4 \times 10^5$ (see text in Sec. 7.5.2). Inset: Electron-spin dynamics in graphene with $^{13}$C abundances of 1% (solid blue curve) and 99% (dashed red curve), in the rotating frame.

### 7.5.3 Comparison and discussion

It is interesting to note that the electron-spin decoherence times in graphene are shorter than in CNTs. Naively, one would assume that the CNT curvature and the associated hybridization would lead to an enhancement of the nuclear-spin interactions due to the contact interaction (7.4). As it turns out, however, the contact interaction in a CNT has a competing sign as compared to the anisotropic hyperfine interaction along the CNT symmetry axis and, hence, effectively reduces the total hyperfine coupling strength along the direction of the external magnetic field. For ultra-small CNTs it might happen that the total hyperfine coupling along the symmetry axis approaches zero [1]. This, however, is beyond the validity of our theory.

For typical CNTs, the dominant contribution to the nuclear-spin interactions in CNTs comes from the anisotropic hyperfine interaction. This is because the amount of $s$-orbital admixture in the hybridized wavefunction of a conduction-band electron is rather small: on the order of a few percent.

In our considerations throughout this section, we have neglected the hyperfine terms which are transverse to the externally applied magnetic field, i.e., radial and circumferential in the case of a CNT, and in-plane in the case of graphene. This gives a good first approximation of the decoherence time, as long as the external magnetic field is large enough to suppress spin flips induced by the hyperfine terms transverse to the external field. For both CNTs and graphene, magnetic fields of order $B \gtrsim 5\,\mathrm{mT}$ are sufficiently strong to achieve this.

[1] We emphasize that this result is different from the ones given by Yazyev and Helm (2005) and Semenov et al. (2007), where only the isotropic hyperfine interactions of the nuclear spins with the 1$s$ and 2$s$ electrons have been considered.

| | $A_1$ [$\mu e$V] | $A_2^x$ [$\mu e$V] | $A_2^{y,z}$ [$\mu e$V] |
|---|---|---|---|
| our values (CNT) | 0.05 | 0.6 | $-0.3$ |
| our values (Graphene) | 0 | 0.6 | $-0.3$ |
| Yazyev (2008) (Graphene flakes) | $-0.2$ | 0.6 | $-0.3$ |
| Pennington and Stenger (1996) ($C_{60}$) | 0.1 | 0.9 | $-0.5$ |
| Goze-Bac et al. (2002) (CNT) | 0.04 | 0.9 | $-0.5$ |

Table 7.2: Comparison of our hyperfine coupling strengths with the values from previous publications for comparable systems. We give our values for a (20,0) zigzag nanotube and for graphene. See Sec. 7.6 for a detailed discussion.

## 7.6 Comparison with previous work

In Table 7.2 we compare our results for the hyperfine interaction in graphene and CNTs with those given in earlier publications for comparable systems. The values given by Yazyev (2008) for the hyperfine interactions in small graphene flakes were derived from DFT calculations including the $\sigma$-bands. The values for the anisotropic hyperfine interaction are similar to our results but a non-vanishing (and even negative) value for the isotropic hyperfine interaction is reported, which is, however, associated with the coupling between the nuclear spins and the $1s$ core electrons, which is irrelevant for the dephasing of the conduction electron. Pennington and Stenger (1996) give estimates for the hyperfine interaction in fullerenes and report coupling constants which are slightly larger than our values. The relatively large value for the isotropic hyperfine interaction can be explained by the stronger curvature in $C_{60}$ molecules, leading to stronger *sp*-hybridization of the electron states, as compared to CNTs. Goze-Bac et al. (2002) have estimated the hyperfine interaction in CNTs based on measurements of the chemical shift of $^{13}$C.

Churchill et al. (2009a) have estimated the hyperfine interaction in carbon nanotubes from transport measurements in double quantum dots, but do not comment on the anisotropy of the interaction. A hyperfine coupling strength of $\sim 100\,\mu e$V for pure $^{13}$C CNTs is reported in their work, in clear contrast to our results. Currently, this discrepancy is not understood. One possible explanation (Trauzettel and Loss, 2009) for this might be that the theory developed by Jouravlev and Nazarov (2006) for standard GaAs quantum dots and used by Churchill et al. (2009a) to deduce the hyperfine coupling strength gets modified by the valley degeneracy occurring in CNT and thus this could lead to different conclusions. Another possible explanation raised by Churchill et al. (2009a) could be that the effective electron-nuclear interaction gets greatly enhanced by electron-electron interactions and the one-dimensional character of the system. A similar renormalization was recently noticed in the context of nuclear magnetic ordering in CNT by Braunecker et al. (2009a,b). Clearly, this is an interesting open problem, which, however, requires separate study.

## 7.7 Conclusions

We have calculated the nuclear-spin interactions and the resulting spin dynamics of an electron confined to a CNT or graphene quantum dot. In graphene, only the anisotropic hyperfine interaction couples the electron to the nuclear spins, due to the purely $p$-type electron wavefunction. In a CNT, curvature induces an $sp$-hybridization of the electron orbital, opening a new channel of spin decoherence via the Fermi contact interaction. However, for typical CNTs, the Fermi contact interaction is only a small correction to the anisotropic hyperfine interaction, the latter being the main source of nuclear-spin-induced decoherence of the electron spin. We found the total hyperfine coupling strength of an electron with the $^{13}$C nuclei to be less than $1\,\mu e$V for both graphene and CNTs quantum dots – about two orders of magnitude smaller than the hyperfine interaction of an electron in a GaAs or InAs quantum dot.

We have used a simple model for the $sp$-hybridization in CNTs, from which we have derived the hyperfine interaction. We have checked, however, that a numerical tight-binding band structure calculation yields hybridization on the same order of magnitude as the geometrical approach used in this work (Schmidt, 2009). Nevertheless, a more rigorous band structure calculation including also the influence of the CNT $\sigma$-bands would be desirable in the future.

For CNTs, we have found an interesting interplay of hyperfine couplings along different spatial directions, leading to a highly anisotropic Knight shift and an alignment of the $^{13}$C nuclear spins around the CNT in the ground state of the nuclear spins. This result is particularly interesting when viewed in context of the hyperfine-induced nuclear phase transition predicted by Braunecker et al. (2009a,b) for a Luttinger liquid, which requires a non-vanishing mean value of the hyperfine field. The strong anisotropy of the hyperfine field that we have found in our work thus gives further evidence that such phase transitions could occur in CNTs. We emphasize that this anisotropy is present in CNTs of any chirality, in particular also in metallic CNTs. The results presented here have been used very recently in the context of transport though CNT quantum dots (Pályi and Burkard, 2009), taking also into account the valley degrees of freedom.

Furthermore, we have estimated typical electron-spin decoherence times in CNT and graphene quantum dots. We have shown that relaxation-induced decoherence due to nuclear spins can be suppressed by applying a magnetic field of order 5 mT to the system, leaving only pure dephasing due to fluctuations of the nuclear magnetic field. We have estimated that for a (20,0) zigzag CNT quantum dot containing $N \simeq 6 \times 10^5$ nuclei, and for a magnetic field applied along the CNT symmetry axis, the associated decoherence time is of order $\tau_c \gtrsim 1\,\mu$s, depending on the relative $^{13}$C abundance. We emphasize that our analytical treatment of the hyperfine problem applies to CNTs of any chirality. For a graphene quantum dot containing $N = 4 \times 10^5$ nuclei, and for a magnetic field applied perpendicular to the graphene plane, the decoherence time is of order $\tilde{\tau}_c \gtrsim 0.5\,\mu$s, again depending on the relative $^{13}$C abundance.

The hyperfine interaction in the systems we have considered here is rather weak. Therefore, it could, in principle, be that other mechanisms, such as spin-orbit interactions, limit the lifetime of spin-state superpositions on timescales comparable to those we have estimated here (see Bulaev et al. (2008) for details).

The decoherence times we have estimated throughout this work are among the longest

reported so far. This makes quantum dots based on carbon materials attractive spin-qubit candidates. In particular, the tunability of the average hyperfine coupling strength via the abundance of spin-carrying $^{13}$C nuclei could be used to achieve an optimal balance between a long electron-spin decoherence time and a sufficiently strong coupling to control the electron-spin state by manipulating the nuclear-spin system.

Chapter 8

# Conclusions and Outlook

In this last chapter we will take a step back and have a look at how the results presented in this thesis can been seen from a more general perspective. Our starting point in Chapter 1 had been the question whether or not it might be possible to build a (spin-based) quantum computer one day. We have discussed the problem of short decoherence times in detail throughout this thesis – one of the main obstacles towards viable quantum computation – and we have also discussed several strategies to circumvent this problem, each having certain practical advantages and disadvantages.

Electron-spin quantum dots in III-V semiconductors, in particular GaAs quantum dots, are by now understood very well, both theoretically and experimentally, and an enormous experimental progress has been observed over the last years. By now it is not only possible to initialize and readout single-spin states in such systems, but also to manipulate single spins coherently and to couple and decouple two qubits on demand. Thus, in principle, all basic prerequisites for using confined electron spins in III-V semiconductors as viable qubits are fulfilled. One essential remaining problem is to couple an array of many electron-spin qubits in such a way that individual spins can be addressed and that two-qubit operations can be carried out coherently on any pair of electron spins of the array. There has been a lot of progress in this direction, but the larger the array of qubits gets, the more challenging it becomes to construct and operate gates to carry out the desired qubit operations.

Another problem to work on would be to initialize the nuclear spin bath in a perfectly narrowed state. So far, a narrowing of the broad nuclear-spin frequency distribution to a couple of narrow peaks has been achieved, but it would be very desirable to go down to one single delta-peak. In this case, it would be experimentally possible to observe the well-defined exponential decoherence we have described in Chapters 3 and 4. On the other hand, quantum error-correction schemes relying on such an exponential decay, should be generalized to be able to handle also other types of decay, such as super-exponential or power-laws.

The idea to use confined hole spins as qubits is very recent and, thus, theoretical and experimental progress is not as advanced as compared to electrons. However, as we have described in Chapter 5, holes couple to nuclear spins in such a way that decoherence can be suppressed very effectively, even without preparing the nuclear spin bath in a narrowed state. However, there are several theoretical and experimental challenges. For instance, as we have discussed,

strain can lead to an enhancement in the off-diagonal nuclear-spin coupling and thus to shorter decoherence times. It would be therefore desirable to fabricate strain-free hole-spin quantum dots by gating a two-dimensional hole gas (2DHG) just like in the electron case. It turns out, however, that this is experimentally slightly more challenging than in the electron case, and it was so far not possible to operate a gated quantum dot in the single-hole regime. A promising alternative might be nanowires which are grown in alternating layers of a donor and an acceptor material in such a way that they consist of a stack of quasi-two-dimensional discs which could then be gated to define either electron or hole quantum dots. On the theoretical side, it would be important to identify the main sources that lead to hybridization of the heavy-hole band with the neighboring bands and to be able to quantify the amount of mixing in terms of the relevant physical parameters. Since the strain in self-assembled quantum dots is typically neither uniform nor linear (i.e., it cannot be described by a linear strain tensor), this problem is technically very challenging.

Once it has been made possible to fabricate strain-free single-hole quantum dots and to initialize and readout its spin states, it would be necessary to implement schemes for single-qubit and two-qubit operations (such as $\pi/2$ rotations and $\sqrt{\text{SWAP}}$ operations) with inspiration from the electron case. This would open up the possibility of, e.g., applying hole-spin-echo pulse sequences. Nuclear state narrowing should be possible just as in the electron case, allowing for the possibility to study the weak off-diagonal hole-nuclear-spin coupling in detail and to explore its dependence on, e.g., strain or the quantum-dot geometry.

Carbon nanostructures offer the big advantage of a low abundance of spin-carrying nuclear isotopes, as we have seen in Chapter 7 for the case of graphene and carbon nanotube quantum dots. Graphene has been realized experimentally only a couple of years ago, and so far no experimental studies on electron-spin decoherence in graphene quantum dots have been carried out. One problem is that it is hard to fabricate graphene ribbons with well-defined boundaries (e.g., zig-zag or armchair), and it would be a major experimental step to find ways to change this. Although spin blockade measurements have been carried out in both graphene and carbon nanotube systems, it has not yet been possible to confine a single electron in these systems, which would be a prerequisite for exploring their single-spin physics. Another open question is the role of the valley degrees of freedom in carbon systems. There are some indications that this additional pseudospin might also couple to the nuclear spins, potentially leading to faster spin decoherence. An interesting topic to study theoretically would be the question how the anisotropy of the hyperfine interaction affects the spin decoherence in both graphene and CNTs. Furthermore, a more rigorous derivation of the *sp*-hybridized electron wavefunctions in CNTs, e.g., based on $\mathbf{k} \cdot \mathbf{p}$ calculations, would be desirable.

Whether or not a quantum computer will exist one day is unclear from today's point of view. What can be said is that there is a long way to go still, and a lot of fundamental research will still be needed.

Appendix A

# Additional details on 'Electrons in III-V semiconductors'

## A.1 Effective-Hamiltonian approach: Continuum limit

In this section, we describe how the dimensionality $d$ and envelope wave function shape parameter $q$ are defined. For further details on the definition of these quantities, see Coish and Loss (2004). For a homonuclear spin system, the hyperfine coupling constants are given by

$$A_k = A v_0 \left|\psi(\mathbf{r}_k)\right|^2, \tag{A.1}$$

where $A$ is the total hyperfine coupling constant, $v_0$ is the volume occupied by a single-nucleus unit cell, and $\psi(\mathbf{r})$ is the electron envelope wave function. We assume an isotropic electron envelope:

$$\psi(r_k) = \psi(0) \exp\left\{-\frac{1}{2}\left(\frac{r_k}{a_B}\right)^q\right\}, \tag{A.2}$$

where $a_B$ is the dot Bohr radius, defined as the radial distance enclosing $N$ nuclear spins, and $r_k$ is the radial distance enclosing $k$ spins. In $d$ dimensions:

$$\frac{\mathrm{vol}(k\,\mathrm{spins})}{\mathrm{vol}(N\,\mathrm{spins})} = \frac{v_0 k}{v_0 N} = \left(\frac{r_k}{a_B}\right)^d. \tag{A.3}$$

Inserting Eqs. (A.3) and (A.2) into Eq. (A.1) yields

$$A_k = A_0 \exp\left\{-\left(\frac{k}{N}\right)^{q/d}\right\}. \tag{A.4}$$

To determine the $k = 0$ coupling $A_0$, we enforce the normalization

$$\sum_k A_k = A v_0 \sum_k \left|\psi(r_k)\right|^2 \approx A \int d^3 r \left|\psi(r)\right|^2 = A. \tag{A.5}$$

This gives

$$A = A_0 \int_0^\infty dk \exp\left\{-\left(\frac{k}{N}\right)^{q/d}\right\}. \tag{A.6}$$

Making the change of variables $u = \left(\frac{k}{N}\right)^{q/d}$, we find

$$A = A_0 \frac{d}{q} N \int_0^\infty du\, u^{\frac{d}{q}-1}\, e^{-u} = A_0 N \frac{d}{q}\, \Gamma\left(\frac{d}{q}\right), \tag{A.7}$$

which gives the final form for $A_k$:

$$A_k = \frac{A}{N \frac{d}{q}\, \Gamma\left(\frac{d}{q}\right)} \exp\left\{-\left(\frac{k}{N}\right)^{q/d}\right\}. \tag{A.8}$$

## A.2 Effective-Hamiltonian approach: Born approximation

In this section we give further detail on the Born approximation. We begin from the equation of motion for the transverse spin in the rotating frame $x_t$ after applying the Markov approximation, neglecting the correction $\epsilon(t)$ (following Eq. (3.38)):

$$\dot{x}_t = -i \int_0^\infty d\tau \tilde{\Sigma}(\tau) x_t, \tag{A.9}$$

$$\tilde{\Sigma}(t) = e^{-i(\omega_n + \Delta\omega)t} \Sigma(t), \tag{A.10}$$

$$\Sigma(t) = -i \mathrm{Tr} S_+ \mathsf{LQ} e^{-i\mathsf{LQ}t} \mathsf{LQ} \left|n\right\rangle \left\langle n\right| S_-. \tag{A.11}$$

In general, it is not simple to find the exact form of the self energy (memory kernel) $\Sigma(t)$. Fortunately, it is possible to generate a systematic expansion in the perturbation $V = XS^z \propto 1/b$, valid for sufficiently large Zeeman splitting $b > A$ (Coish and Loss, 2004):

$$\Sigma(t) = \Sigma^{(2)}(t) + \Sigma^{(4)}(t) + \cdots, \tag{A.12}$$

where $\Sigma^{(n)}(t)$ indicates a term of order $\sim \mathcal{O}(V^n) \sim \mathcal{O}\left[\left(\frac{A}{b}\right)^n\right]$. The expansion is performed most conveniently in terms of the Laplace-transformed variable

$$\Sigma(s) = \mathcal{L}\left[\Sigma(t)\right] = \int_0^\infty dt\, e^{-st}\, \Sigma(t). \tag{A.13}$$

We expand the propagator

$$\mathcal{L}\left[e^{-i\mathsf{LQ}t}\right] = \frac{1}{s + i\mathsf{LQ}} \tag{A.14}$$

by dividing the full Liouvillian into unperturbed and perturbed parts: $\mathsf{L} = \mathsf{L}_0 + \mathsf{L}_V$, where $\mathsf{L}_0$ and $\mathsf{L}_V$ are defined by their action on an arbitrary operator $O$ through $\mathsf{L}_0 O = [H_0, O]$ and $\mathsf{L}_V O = [V, O]$. To obtain an expansion in terms of the perturbation $\mathsf{L}_V$, we now iterate the Dyson identity in Laplace space:

$$\frac{1}{s + i\mathsf{LQ}} = \frac{1}{s + i\mathsf{L}_0\mathsf{Q}} - i \frac{1}{s + i\mathsf{L}_0\mathsf{Q}} \mathsf{L}_V \mathsf{Q} \frac{1}{s + i\mathsf{L}_0\mathsf{Q}} + \mathcal{O}\left(\mathsf{L}_V^2\right). \tag{A.15}$$

Inserting the iterated expression (A.15) into the Laplace-transformed version of Eq. (A.11), we find the self energy in Born approximation (to second order in $V$) is

$$\Sigma^{(2)}(s) = -i \mathrm{Tr}\left[S_+ \left(1 - i\mathsf{L}_0\mathsf{Q} \frac{1}{s + i\mathsf{L}_0}\right) \times \mathsf{L}_V \frac{1}{s + i\mathsf{L}_0} \mathsf{L}_V \left|n\right\rangle \left\langle n\right| S_-\right]. \tag{A.16}$$

We have simplified the above expression using the following identities for the projection superoperators $\mathsf{Q} = 1 - |n\rangle\langle n| \,\mathrm{Tr}_I$ and $\mathsf{P} = 1 - \mathsf{Q}$:

$$\begin{aligned} \mathsf{P}\mathsf{L}_0\mathsf{P} &= \mathsf{L}_0\mathsf{P}, & \text{(A.17)} \\ \mathsf{P}\mathsf{L}_V |n\rangle\langle n| &= 0, & \text{(A.18)} \\ \mathsf{Q}\mathsf{L}_0\mathsf{Q} &= \mathsf{Q}\mathsf{L}_0, & \text{(A.19)} \end{aligned}$$

which can be proven directly. To further reduce the above expression, we evaluate the action of $\mathsf{L}_0$ and $\mathsf{L}_V$ on the electron spin operator $S_-$:

$$\mathsf{L}_V S_- = -\frac{1}{2}\mathsf{L}_X^+ S_-, \qquad \mathsf{L}_0 S_- = \left(-\frac{1}{2}\mathsf{L}_\omega^+ + \mathsf{L}_D\right) S_-, \tag{A.20}$$

where

$$\mathsf{L}_X^+ O = [X, O]_+, \qquad L_\omega^+ O = [\omega, O]_+, \qquad L_D O = [D, O], \tag{A.21}$$

and here we denote anticommutators with a '+' subscript: $[A, B]_+ = AB + BA$. This leads to

$$\Sigma^{(2)}(s) = -\frac{i}{4}\mathrm{Tr}_I \left[\left(1 + \frac{i}{2}\mathsf{L}_\omega^+ \mathsf{Q}\frac{1}{s - \frac{i}{2}\mathsf{L}_\omega^+}\right) \times \mathsf{L}_X^+ \frac{1}{s + i\left(\mathsf{L}_D - \frac{1}{2}\mathsf{L}_\omega^+\right)} \mathsf{L}_X^+ |n\rangle\langle n|\right]. \tag{A.22}$$

Now, noting that

$$\mathsf{Q}|n\rangle\langle n| = 0, \qquad \mathsf{Q}|k\rangle\langle k| = |k\rangle\langle k| - |n\rangle\langle n|, \tag{A.23}$$

we can evaluate Eq. (A.22) directly, giving

$$\begin{aligned} \Sigma^{(2)}(s + i\omega_n) = -\frac{i}{2}\sum_k |X_{kn}|^2 &\left(\frac{s + \frac{i}{2}\delta\omega_{nk}}{s + i\delta\omega_{nk}}\right) \\ &\times \left(\frac{1}{s + i\left(\delta D_{kn} + \frac{1}{2}\delta\omega_{nk}\right)} + \frac{1}{s - i\left(\delta D_{kn} - \frac{1}{2}\delta\omega_{nk}\right)}\right), \end{aligned} \tag{A.24}$$

where $\delta D_{kn} = D_k - D_n$, $\delta\omega_{nk} = \omega_n - \omega_k$, and $\omega_k$, $D_k$ are the eigenvalues associated with eigenstate $|k\rangle$: $\omega|k\rangle = \omega_k|k\rangle$, $D|k\rangle = D_k|k\rangle$. Additionally, we have denoted $X_{kn} = \langle k|X|n\rangle$.

From Eqs. (A.9), (A.10), and (A.13), the electron-spin decoherence rate within a Born-Markov approximation will now be given by

$$\frac{1}{T_2} = -\mathrm{Im}\,\Sigma^{(2)}(s = i(\omega_n + \Delta\omega) + 0^+), \tag{A.25}$$

where $0^+$ denotes a positive infinitesimal. Our goal here is to find the leading-order dependence of $1/T_2$ on $1/b$ for large Zeeman splitting: $b > A$. We therefore set

$$\Delta\omega = -\mathrm{Re}\,\Sigma^{(2)}(s = i(\omega_n + \Delta\omega) + 0^+) \sim \mathcal{O}\left(\frac{A}{N}\left(\frac{A}{b}\right)^2\right) \approx 0, \tag{A.26}$$

since this term will lead to higher-order corrections in $1/b$ within the perturbative regime. Additionally, noting that the matrix element $X_{kn}$ induces a flip-flop for spins at two sites $k_{1,2}$, we find $|\delta D_{kn}| = |b\,(\gamma_{k_1} - \gamma_{k_2})|$ and $|\delta\omega_{kn}| = |A_{k_1} - A_{k_2}|$. In the case of a homonuclear system $\gamma_{k_1} = \gamma_{k_2}$, we can set $\delta D_{kn} = 0$ in Eq. (A.24). Otherwise, in a sufficiently large magnetic field $|b\,(\gamma_{k_1} - \gamma_{k_2})| > |A_{k_1} - A_{k_2}|$, we find a negligible contribution to the decoherence rate for terms from two different isotopic species (where $\gamma_{k_1} \neq \gamma_{k_2}$), i.e., heteronuclear flip-flops no longer conserve energy, although homonuclear flip-flops (for which $\gamma_{k_1} = \gamma_{k_2}$) will still occur. Restricting the sum to homonuclear flip-flops and setting $\delta D_{nk} = 0$ in this regime gives

$$\Sigma^{(2)}(s + i\omega_n) = -i \sum_j \sum_k \left| X^j_{kn} \right|^2 \frac{1}{s + i\delta\omega_{nk}}, \tag{A.27}$$

where $X^j_{kn} = \langle k|\, X^j\, |n\rangle$ and $X^j$ is restricted to run over flip-flops between nuclei of the common species $j$ at sites denoted by the indices $k_j$, $l_j$:

$$X^j = \frac{1}{2} \sum_{k_j \neq l_j} \frac{A^j_{k_j} A^j_{l_j}}{\omega} I^-_{k_j} I^+_{l_j}. \tag{A.28}$$

Inserting Eq. (A.27) for a homonuclear system (one isotopic species $j$) into Eq. (A.25) and inverting the Laplace transform leads directly to Eq. (3.42) of the main text.

## A.3 Effective-Hamiltonian approach: Decoherence rate

Applying Eq. (A.25) (setting $\Delta\omega \approx 0$) with Eq. (A.27) gives the rate

$$\frac{1}{T_2} = \pi \sum_j \sum_k \left| X^j_{kn} \right|^2 \delta\left(\delta\omega_{kn}\right), \tag{A.29}$$

which can be found directly from the formula

$$\frac{1}{x \pm i0^+} = \mathcal{P}\frac{1}{x} \mp i\pi\delta(x), \tag{A.30}$$

where $\mathcal{P}$ indicates that the principle value should be taken in any integral over $x$. Rewriting Eq. (A.29) using the definition of $X^j$ given in Eq. (A.28):

$$\frac{1}{T_2} = \frac{\pi}{4} \sum_j \sum_{k_j \neq l_j} \frac{c^{jk_j}_- c^{jl_j}_+}{\omega_k \omega_n} (A^j_{k_j})^2 (A^j_{l_j})^2\, \delta(A^j_{k_j} - A^j_{l_j}), \tag{A.31}$$

where $k_j$ and $l_j$ are restricted to run over sites occupied by isotopic species $j$. The coefficients $c^{jk_j}_\pm$ give the expectation value of the operator $I^\mp_{k_j} I^\pm_{k_j}$ with respect to the initial state:

$$c^{jk_j}_\pm = \langle n|\, I^\mp_{k_j} I^\pm_{k_j}\, |n\rangle = I^j(I^j + 1) - \langle n|\, I^z_{k_j}(I^z_{k_j} \pm 1)\, |n\rangle\,. \tag{A.32}$$

With small corrections of order $A/Nb \ll 1$, we can replace $\omega_k \simeq \omega_n$ in the denominator of Eq. (A.31). If the various nuclear isotopes are uniformly distributed with isotopic concentrations

$\nu_j$, we allow the sum over $k_j$, $l_j$ to extend over all sites $k, l$ at the expense of a weight factor $\nu_j$ for each index:

$$\sum_{k_j \neq l_j} \approx \nu_j^2 \sum_{k \neq l}. \tag{A.33}$$

Additionally, we assume that the system is uniformly polarized on the scale of variation of the hyperfine coupling constants so that the coefficients $c_\pm^{jk}$ can be replaced by average values $c_\pm^j = \langle\langle c_\pm^{jk} \rangle\rangle$ (double angle brackets indicate an average over all sites) and taken out of the sum. Finally, we change the sums over sites to a double integral using the prescription and coupling constants described in Appendix A.1, neglecting the small $\mathcal{O}(1/N)$ correction due to the requirement $k \neq l$:

$$\sum_{k \neq l} \to \int_0^\infty dk \int_0^\infty dl. \tag{A.34}$$

These approximations give

$$\frac{1}{T_2} = \frac{\pi}{4\omega_n^2} \sum_j \nu_j^2 c_-^j c_+^j \int_0^\infty dk \int_0^\infty dl (A_k^j)^2 (A_l^j)^2 \, \delta(A_k^j - A_l^j). \tag{A.35}$$

Inserting the coupling constants defined by Eq. (A.8) and evaluating the integrals gives

$$\frac{1}{T_2} = \frac{\pi}{4} f\left(\frac{d}{q}\right) \sum_j \nu_j^2 c_-^j c_+^j \frac{A^j}{N} \left(\frac{A^j}{\omega_n}\right)^2, \tag{A.36}$$

with the geometrical factor $f(d/q)$ given by Eq. (3.48) of the main text. Eq. (A.36) reduces to Eqs. (3.47), (3.50), and (3.52) of the main text in the special cases discussed there.

## A.4 Direct approach: Self-energy expansion

Here we give the explicit self-energy up to fourth order in $V_{\mathrm{ff}}$. The full self-energy superoperator is given by

$$\Sigma(s) = \Sigma^{(2)}(s) + \Sigma^{(4)}(s) + O(V_{\mathrm{ff}}^6), \tag{A.37}$$

where

$$\Sigma^{(2)}(s) = -i\mathrm{Tr}\left\{S_+ \mathsf{L}_V \mathsf{G}(s) \mathsf{L}_V S_- \rho_I(0)\right\}, \tag{A.38}$$

with

$$\mathsf{G}(s) = \frac{1}{s + i\mathsf{L}_0}, \qquad \mathsf{L}_0 O = [H_0, O], \qquad \mathsf{L}_V O = [V_{\mathrm{ff}}, O]. \tag{A.39}$$

The fourth-order result is

$$\Sigma^{(4)}(s) = i\mathrm{Tr}\left\{S_+ \left(1 - iL_0 Q \mathsf{G}(s)\right) L_V \mathsf{G}(s) L_V Q \mathsf{G}(s) L_V \mathsf{G}(s) L_V S_- \rho_I(0)\right\}. \tag{A.40}$$

More explicitly, using Eq. (4.5) for the initial nuclear state we find $\Sigma^{(p)}(s) = \sum_l \rho_{ll} \Sigma_l^{(p)}(s)$, where

$$\Sigma_l^{(2)}(s) = -\frac{i}{4} \sum_k \left( \frac{[h^-]_{n_l k} [h^+]_{k n_l}}{s + i\delta\omega_{kn} - i\omega^I_{k n_l}} + \frac{[h^+]_{n_l k} [h^-]_{k n_l}}{s + i\delta\omega_{kn} + i\omega^I_{k n_l}} \right), \tag{A.41}$$

$$\Sigma_l^{(4)}(s) = \frac{i}{16}\sum_{k_1k_2k_3}\Big\{[h_+]_{n_lk_1}[h_-]_{k_1k_2}[h_+]_{k_2k_3}[h_-]_{k_3n_l}[G_\uparrow]_{k_1n_l}[G_+]_{k_2n_l}[G_\uparrow]_{k_3n_l}(1-\delta_{n_lk_2})$$
$$+[h_-]_{n_lk_1}[h_+]_{k_1k_2}[h_-]_{k_2k_3}[h_+]_{k_3n_l}[G_\downarrow]_{n_lk_3}[G_+]_{n_lk_2}[G_\downarrow]_{n_lk_1}(1-\delta_{n_lk_2})$$
$$+[h_-]_{n_lk_1}[h_+]_{k_1k_2}[h_+]_{k_2k_3}[h_-]_{k_3n_l}\left(1-i\left(\left[L_0^+\right]_{k_2k_2}-\left[L_0^+\right]_{n_ln_l}\right)[G_+]_{k_2k_2}\right)$$
$$\times\Bigg[\left([G_\downarrow]_{k_2k_1}[G_+]_{k_2n_l}[G_\uparrow]_{k_3n_l}+[G_\uparrow]_{k_3k_2}[G_+]_{n_lk_2}[G_\downarrow]_{n_lk_1}\right)(1-\delta_{n_lk_2})$$
$$+\left([G_\uparrow]_{k_3k_2}+[G_\downarrow]_{k_2k_1}\right)[G_-]_{k_3k_1}\left([G_\uparrow]_{k_3n_l}+[G_\downarrow]_{n_lk_1}\right)\Bigg]\Big\}. \quad \text{(A.42)}$$

Here, we denote matrix elements $[h^\pm]_{nk} = \langle n|\, h^\pm\, |k\rangle$. Further, $\delta\omega_{nk} = \frac{1}{2}(h_n^z - h_k^z)$ and $\omega_{nk}^I = \langle n|\, \omega^I\, |n\rangle - \langle k|\, \omega^I\, |k\rangle$, where $\omega^I = b\sum_k \gamma_k I_k^z$, and we have introduced

$$[G_\alpha]_{kk'} = \frac{1}{s + i\,[L_0^\alpha]_{kk'}}, \quad \text{(A.43)}$$

with

$$L_0\,|\downarrow\rangle\langle\uparrow|\,|k\rangle\langle k'| = \left[L_0^+\right]_{kk'}|\downarrow\rangle\langle\uparrow|\,|k\rangle\langle k'|, \quad \text{(A.44)}$$
$$L_0\,|\uparrow\rangle\langle\downarrow|\,|k\rangle\langle k'| = \left[L_0^-\right]_{kk'}|\uparrow\rangle\langle\downarrow|\,|k\rangle\langle k'|, \quad \text{(A.45)}$$
$$L_0\,|\uparrow\rangle\langle\uparrow|\,|k\rangle\langle k'| = \left[L_0^\uparrow\right]_{kk'}|\uparrow\rangle\langle\uparrow|\,|k\rangle\langle k'|, \quad \text{(A.46)}$$
$$L_0\,|\downarrow\rangle\langle\downarrow|\,|k\rangle\langle k'| = \left[L_0^\downarrow\right]_{kk'}|\downarrow\rangle\langle\downarrow|\,|k\rangle\langle k'|. \quad \text{(A.47)}$$

The dominant contributions to the self-energy occur at high frequency ($s \simeq i\omega_n$) in the lab frame. For $|s - i\omega_n| \ll \omega_n$, and $\omega_n \gg \delta\omega_{nk}$, $\omega_n \gg \omega_{n_lk}^I$, we have:

$$[G_\uparrow]_{kn_l} \approx [G_\downarrow]_{kn_l} = \frac{1}{i\omega_n}\left(1 + O\left[\frac{A}{N\omega_n}\right]\right), \quad \text{(A.48)}$$

which allows us to approximate Eqs. (A.41), (A.42) by their high-frequency forms for a uniformly polarized system. We additionally go to the rotating frame; from the definition of $\tilde{\Sigma}$ in Eq. (4.14), we have

$$\Sigma(s + i\omega_n) = \tilde{\Sigma}(s - i\Delta\omega), \quad \text{(A.49)}$$

which gives

$$\tilde{\Sigma}^{(2)}(s - i\Delta\omega) \approx -\frac{1}{4\omega_n}\sum_i \nu_i\left(c_+^i + c_-^i\right)\sum_k \left(A_k^i\right)^2. \quad \text{(A.50)}$$

In the above expression, the sum over $i$ indicates a sum over different nuclear-spin isotopes with abundances $\nu_i$ and hyperfine coupling constants $A_k^i$. The high-frequency form of the fourth-order self-energy is then:

$$\tilde{\Sigma}^{(4)}(s - i\Delta\omega) = \frac{-i}{16\omega_n^2}\sum_{ij}\nu_i\nu_j c_-^i c_+^j \sum_{k_1k_2}(A_{k_1}^i)^2(A_{k_2}^j)^2$$
$$\times\left[\frac{1}{s + ix_{12}^{ij} - i\gamma_{ij}} + \frac{1}{s - ix_{12}^{ij} - i\gamma_{ij}} + \left(\frac{s}{s + i2\gamma_{ij}}\right)\left(\frac{2}{s + i2x_{12}^{ij}} - \frac{1}{s + ix_{12}^{ij} + i\gamma_{ij}}\right)\right.$$
$$\left. + \left(\frac{s}{s - i2\gamma_{ij}}\right)\left(\frac{2}{s + i2x_{12}^{ij}} - \frac{1}{s + ix_{12}^{ij} - i\gamma_{ij}}\right)\right], \quad \text{(A.51)}$$

where $x_{12}^{ij} = (A_{k_1}^i - A_{k_2}^j)/2$, $\gamma_{ij} = b(\gamma_i - \gamma_j)$, and the coefficients $c_\pm^i$ are:

$$c_\pm^i = I_i(I_i+1) - \langle\langle m(m\pm 1)\rangle\rangle\,, \tag{A.52}$$

With the average $\langle\langle\cdots\rangle\rangle$ defined in Eq. (4.7). For a homonuclear system, we have $\gamma_{ij} = 0$ and $x_{12}^{ij} = x_{12} = (A_{k_1} - A_{k_2})/2$, and replace $\sum_{ij}\nu_i\nu_j \to 1$. In this case, assuming a uniformly-polarized nuclear-spin system, the self-energy is given simply by

$$\tilde{\Sigma}^{(4)}(s - i\Delta\omega) = -i\frac{c_+c_-}{4\omega_n^2}\sum_{k,k'}\frac{A_k^2A_{k'}^2}{s - i(A_k - A_{k'})}. \tag{A.53}$$

This self-energy differs from that found in Chapter 3 at leading order in an effective-Hamiltonian treatment, where the Lamb shift $\Delta\omega$ is incorporated directly into the bare precession frequency $\omega_n$. In addition, we stress that the more general self-energy for a heteronuclear system (A.51) is not recovered with the effective Hamiltonian (compare with Eq. (A.24)).

Assuming a two-dimensional parabolic quantum dot (with Gaussian envelope function) leads to coupling constants $A_k = (A/N)e^{-k/N}$ (see Eq. (3.46) for $d = q = 2$). Performing the continuum limit, i.e., replacing $\sum_{k_1,k_2} \to \int dk_1dk_2$, and evaluating the resulting energy integrals, we arrive at Eq. (6.18) of the main text.

## A.5 Direct approach: Higher-order corrections

All results in Chapter 4 are valid up to fourth order in the electron-nuclear flip-flop terms $V_{\rm ff}$. As the electron Zeeman splitting is lowered from $b \gg A$, higher-order corrections to the self-energy may become relevant. In this section, we give explicit conditions under which higher-order corrections may be neglected, even for $b \sim A$. As in Section A.4, the self-energy at any order may be approximated by its high-frequency form (at $s \simeq i\omega_n$) whenever $A/Nb \ll 1$. This allows for a significant simplification in the high-order expansion in terms of $V_{\rm ff}$. With corrections to the self-energy that are smaller by factors of order $1/N \ll 1$ and $A/Nb \ll 1$, we find the high-frequency form of the self-energy to be given by

$$\Sigma(s) \simeq -i\mathrm{Tr}_I\left[\left(\mathsf{G}_+^{-1}\mathsf{Q}^{-1} + \frac{i}{2}\mathsf{L}_\omega^+\right)\sigma\frac{1}{1+\sigma}\rho_I(0)\right], \tag{A.54}$$

where we have introduced

$$\mathsf{G}_+ = \frac{1}{s - \frac{i}{2}\mathsf{L}_\omega^+}, \qquad \sigma = -\frac{i\mathsf{Q}}{4\omega_n}\mathsf{G}_+\left(\mathsf{H}_L + \mathsf{H}_R\right), \tag{A.55}$$

defined in terms of the superoperators (which act on an arbitrary operator $\mathcal{O}$):

$$\mathsf{H}_L\mathcal{O} = h_+h_-\mathcal{O}, \qquad \mathsf{H}_R\mathcal{O} = \mathcal{O}h_-h_+, \qquad \mathsf{L}_\omega^+\mathcal{O} = \{\omega, \mathcal{O}\}\,, \tag{A.56}$$

where $\{,\}$ indicates an anticommutator.

The high-frequency form of the self-energy can now be found directly from Eq. (A.54) with a more moderate constraint on the electron Zeeman splitting ($A/Nb \ll 1$). A direct evaluation

of Eq. (A.54) at arbitrary order and resummation is non-trivial, but we can generate arbitrary higher-order terms with the geometric series:

$$\frac{1}{1+\sigma} = 1 - \sigma + \sigma^2 - \cdots . \tag{A.57}$$

Every factor of $\sigma$ is associated with a nuclear-spin pair flip, giving rise to a factor of $c_+$ or $c_-$, which depend on the nuclear polarization, and a factor of the small parameter $A/\omega_n$. The term at $(2k)^{\text{th}}$ order in $V_{\text{ff}}$ contains $k$ factors of $\sigma$, and consequently $k$ powers of $A/\omega_n$. This suggests that the sixth-order self-energy can in general give corrections of order $\sim (A/\omega_n)^3$, which may modify the sub-leading corrections of this size given by the Markovian decay formula (4.47). However, by direct calculation using the above expansion, we find the leading contributions to the Markovian decay rate at sixth order to be

$$-\mathrm{Im}\Sigma^{(6)}(s = i\omega_n + 0^+) = \mathcal{O}\left[\left(\frac{A}{\omega_n}\right)^4\right]. \tag{A.58}$$

Furthermore, we find that the $\Sigma^{(6)}$ corrections do not lead to a broadening of the continuum band. The first non-vanishing corrections to the Markovian decay rate which do lead to a broadening of the continuum band contain two nuclear-spin pair-flip excitations. These terms occur first at eighth order in $V_{\text{ff}}$ and are suppressed by the factor $(c_+c_-)^2$, which is smaller than the fourth-order corrections by a factor $c_+c_-$ for a polarized nuclear-spin system (e.g., $c_+c_- \propto (1-p^2)$ for nuclear spin $I = 1/2$). This result demonstrates that the qualitative decrease in the decoherence rate at low electron Zeeman splitting shown in Figs. 4.5, 4.6, and 4.7 will not be significantly modified by higher-order corrections, at least in the case of a large polarization, where perturbation theory still applies at a smaller value of the electron Zeeman splitting.

## A.6 Direct approach: Interaction time

Here we clarify the time scale at which various terms in the generalized master equation can become relevant. In particular, we intend to quantify the time scale over which the Lamb shift attains its full value (the "interaction time" indicated in Sec. 4.4.3). Our starting point is Eq. (4.9) for the transverse components of the electron spin in the lab frame. After expanding the self-energy: $\Sigma(t) = \sum_n \Sigma^{(n)}(t)$, this becomes

$$\frac{d}{dt}\langle S_+\rangle_t = i\omega_n \langle S_+\rangle_t - i\int_0^t dt' \Sigma^{(2)}(t-t')\langle S_+\rangle_{t'} - i\int_0^t dt' \Sigma^{(4)}(t-t')\langle S_+\rangle_{t'} + \cdots . \tag{A.59}$$

The first term on the right-hand side gives rise to a rapid precession of $\langle S_+\rangle_t$ at the frequency $\omega_n$. Going to a rotating frame at this frequency, i.e.,

$$\langle \tilde{S}_+\rangle_t = e^{-i\omega_n t}\langle S_+\rangle_t, \qquad \tilde{K}(t) = e^{-i\omega_n t}\Sigma^{(2)}(t), \tag{A.60}$$

and neglecting the higher-order corrections $\sim \Sigma^{(4)}$, etc., we find

$$\frac{d}{dt}\langle \tilde{S}_+\rangle_t \simeq -i\int_0^t dt' K(t-t')\langle \tilde{S}_+\rangle_{t'}. \tag{A.61}$$

At short times $t \ll 1/\Delta\omega$, where $\Delta\omega$ gives the typical amplitude of the right-hand side of Eq. (A.61), we can approximate the spin expectation value by a constant in the integrand: $\langle\tilde{S}_+\rangle_{t'} \simeq \langle\tilde{S}_+\rangle_0$. Within the range of validity of this approximation, integrating the equation of motion gives

$$\langle\tilde{S}_+\rangle_t \simeq e^{-i\phi(t)}\langle\tilde{S}_+\rangle_0, \qquad \phi(t) = \int_0^t dt' \int_0^{t'} dt'' \tilde{K}(t''). \tag{A.62}$$

At times shorter than the self-energy correlation time $t \ll \tau_c \sim N/A$, and for $\omega_n \gg A/N$, the memory kernel can be well-approximated by $\tilde{K}(t) \simeq -i\omega_n \Delta\omega^{(2)} e^{i\omega_n t}$ with second-order Lamb shift $\Delta\omega^{(2)} = -\mathrm{Re}\int_0^\infty dt K(t)$. Inserting this approximation for $\tilde{K}(t)$ and performing the remaining integrals gives

$$\phi(t) \simeq -i\Delta\omega^{(2)} \left( \frac{1 - e^{i\omega_n t}}{\omega_n} + it \right). \tag{A.63}$$

After a very short time scale ($t \gg 1/\omega_n$), the $t$-linear term dominates, giving a purely real phase:

$$\phi(t) \simeq \Delta\omega^{(2)} t, \quad t \gg 1/\omega_n. \tag{A.64}$$

The long-time limit $t \gg 1/\omega_n$ is consistent with the earlier assumed short-time approximations $t \ll \Delta\omega \simeq \Delta\omega^{(2)}$ and $t \ll N/A$, whenever $A/N, \Delta\omega \ll \omega_n$.

From the above analysis, the Lamb shift attains its full value on a very short time scale $\sim 1/\omega_n$ provided $\omega_n \gg \Delta\omega$. Within the sudden approximation, the interaction time is therefore determined by $t \gtrsim 1/\omega_n$.

Appendix **B**

# Additional details on 'Holes in III-V semiconductors'

## B.1 Heavy-hole states

In this section we give details on our derivation of an approximate basis of heavy-hole (HH) eigenstates in a quantum dot. We will approximate the ground-state quantum-dot envelope function in the HH sub-band by

$$\phi(\mathbf{r}) = \phi_z(z)\,\phi_\rho(\rho), \tag{B.1}$$

$$\phi_\rho(\rho) = \frac{1}{\sqrt{\pi}l}\exp\left(-\frac{\rho^2}{2l^2}\right), \tag{B.2}$$

$$\phi_z(z) = \sqrt{\frac{2}{a_z}}\sin\left(\frac{\pi z}{a_z}\right), \quad z = [0\ldots a_z], \tag{B.3}$$

where $a_z$ is the width of the confinement potential along the growth direction (for definition of the other symbols see Eq. (5.9)). We will then estimate the size of the splitting $\Delta_{\mathrm{LH}}$ between the HH and the light-hole (LH) band and the degree of hybridization with the conduction band (CB), LH and split-off (SO) sub-bands.

We start from the $8\times 8$ Kane Hamiltonian given in Chapter 2.3 for bulk zinc-blende-type crystals, which is written in terms of the exact eigenstates (near $\mathbf{k}=\mathbf{0}$) of an electron in the CB, HH, LH and SO band, usually denoted by $|1/2;\pm 1/2\rangle_c$, $|3/2;\pm 3/2\rangle_v$, $|3/2;\pm 1/2\rangle_v$, and $|1/2;\pm 1/2\rangle_v$, respectively. We neglect terms that are more than two orders of magnitude smaller than the fundamental band-gap energy $E_g$ [1] and perform the quasi-two-dimensional limit by assuming that a confinement potential has been applied along the growth direction. If the confinement potential is sufficiently strong (i.e., if the quantum well is sufficiently narrow), the energy-level spacing will be large and the electron will be in the ground state at low temperatures. Any operator acting on the $z$-component of the electron envelope function can

[1] In terms of the notation used by Winkler (2003), these are the terms proportional to $C$, $B_{7v}$, and $B_{8v}^{\pm}$. These terms will not lead to considerable corrections for our purposes. However, the terms $Ck_{\pm}$ could become relevant when considering higher-order effects in the spin-orbit interaction, such as the cubic Dresselhaus terms which were derived by Bulaev and Loss (2005).

then be replaced by its expectation value with respect to the $z$-component of the ground-state envelope function. For the Kane Hamiltonian this means that we can replace powers of the $z$-component $\hbar k_z$ of the crystal momentum $\hbar\mathbf{k}$ by expectation values. Assuming an infinite square-well potential of width $a_z$ confining the electron along the growth direction, the ground state is given by Eq. (B.3). Calculating the expectation value of $k_z$ and $k_z^2$ with respect to the ground state, we find $\langle k_z\rangle = 0$ and $\langle k_z^2\rangle = \pi^2/a_z^2$. This allows us to write the Kane Hamiltonian in the following form:

$$H_K = \begin{pmatrix} H_{\mathrm{CB}} & V_1 & V_2 & V_3 \\ V_1^\dagger & H_{\mathrm{HH}} & V_4 & V_5 \\ V_2^\dagger & V_4^\dagger & H_{\mathrm{LH}} & V_6 \\ V_3^\dagger & V_5^\dagger & V_6^\dagger & H_{\mathrm{SO}} \end{pmatrix}, \tag{B.4}$$

where

$$\begin{aligned} H_{\mathrm{CB}} &= \begin{pmatrix} A & 0 \\ 0 & A \end{pmatrix}, & H_{\mathrm{HH}} &= \begin{pmatrix} B & 0 \\ 0 & B \end{pmatrix}, \\ H_{\mathrm{LH}} &= \begin{pmatrix} C & 0 \\ 0 & C \end{pmatrix}, & H_{\mathrm{SO}} &= \begin{pmatrix} D & 0 \\ 0 & D \end{pmatrix}, \\ V_1 &= \tfrac{1}{\sqrt{2}} \begin{pmatrix} -E & 0 \\ 0 & E^* \end{pmatrix}, & V_2 &= \tfrac{1}{\sqrt{6}} \begin{pmatrix} 0 & E^* \\ -E & 0 \end{pmatrix}, \\ V_3 &= \tfrac{1}{\sqrt{3}} \begin{pmatrix} 0 & -E^* \\ -E & 0 \end{pmatrix}, & V_4 &= \sqrt{3} \begin{pmatrix} 0 & F \\ F^* & 0 \end{pmatrix}, \\ V_5 &= \sqrt{6} \begin{pmatrix} 0 & -F \\ F^* & 0 \end{pmatrix}, & V_6 &= \sqrt{2} \begin{pmatrix} -G & 0 \\ 0 & G \end{pmatrix}, \end{aligned}$$

and

$$\begin{aligned} A &= E_g + \hbar^2(k_x^2 + k_y^2 + \langle k_z^2\rangle)/2m', \\ B &= -\epsilon[(\gamma_1' + \gamma_2')(k_x^2 + k_y^2) + (\gamma_1' - 2\gamma_2')\langle k_z^2\rangle], \\ C &= -\epsilon[(\gamma_1' - \gamma_2')(k_x^2 + k_y^2) + (\gamma_1' + 2\gamma_2')\langle k_z^2\rangle], \\ D &= -\epsilon\gamma_1'(k_x^2 + k_y^2 + \langle k_z^2\rangle) - \Delta_{\mathrm{SO}}, \\ E &= Pk_+, \\ F &= \epsilon[\gamma_2'(k_x^2 - k_y^2) - 2i\gamma_3' k_x k_y], \\ G &= \epsilon\gamma_2'(k_x^2 + k_y^2 - 2\langle k_z^2\rangle). \end{aligned}$$

Here, $\epsilon = \hbar^2/2m_0$ and $m_0$ is the free-electron mass, whereas $m'$ is the effective mass of a CB electron. Furthermore, $k_\pm = k_x \pm ik_y$, $\gamma_j'$ denote the Luttinger parameters, $P$ is the inter-band momentum, and $\Delta_{\mathrm{SO}}$ is the spin-orbit gap between the LH and the SO bands. Experimental values for these parameters can be found in Table B.1.

We assume a circular-symmetric parabolic confinement potential with frequency $\omega_0$ in the $xy$-plane defining a quantum dot. Including a magnetic field along the growth direction, the ground state is approximately described by the Gaussian given in Eq. (B.2). The envelope function of the quantum dot is then the product of the in-plane and out-of-plane components, as given in Eq. (B.1).

In the quasi-two-dimensional limit, a gap

$$\Delta_{\mathrm{LH}} = \langle B - C \rangle = -\frac{\hbar^2 \gamma_2'}{m_0}\Big(\langle k_x^2 \rangle + \langle k_y^2 \rangle - 2\langle k_z^2 \rangle\Big) \tag{B.5}$$

develops between the HH and LH sub-bands, lifting the HH-LH degeneracy (see Fig. 2.3). Here, $\langle \cdots \rangle$ denotes the expectation value with respect to (B.1). The in-plane level spacing scales like $\sim 1/l^2$, where $l$ is the dot Bohr radius. The in-plane level spacing is much smaller than the level spacing along the growth direction since, for typical dots, $a_z^2 \ll l^2$. Neglecting $\langle k_x^2 \rangle$ and $\langle k_y^2 \rangle$ compared to $\langle k_z^2 \rangle$ in Eq. (B.5) and inserting $\langle k_z^2 \rangle = \pi^2/a_z^2$ for a square-well potential, we estimate

$$\Delta_{\mathrm{LH}} \simeq \frac{2\pi^2 \gamma_2' \hbar^2}{a_z^2 m_0} \simeq 100\,\mathrm{m}e\mathrm{V} \tag{B.6}$$

for $a_z \simeq 5\,\mathrm{nm}$, using $\gamma_2' \simeq 2.06$ for GaAs (see Table B.1). The HH-LH splitting is thus much larger than the typical energy scale associated with the hyperfine interaction ($A_e \simeq 90\,\mu e\mathrm{V}$ for CB electrons in GaAs).

To derive the approximate electron eigenfunctions in the HH sub-band of the quantum well, we start from the Kane Hamiltonian (B.4). We use quasi-degenerate perturbation theory up to first order in $1/\mathcal{E}$ (where $\mathcal{E}$ stands for $E_g$, $\Delta_{\mathrm{LH}}$, or $\Delta_{\mathrm{LH}} + \Delta_{\mathrm{SO}}$), taking $H_{\mathrm{HH}}$ as the unperturbed Hamiltonian (Winkler, 2003). This leads to a band-hybridized state of the form

$$|\Psi^{\sigma}_{\mathrm{HH,hyb}}\rangle = \mathcal{N}_\sigma \sum_n \lambda_n^\sigma |\phi_{n\sigma}; u_{n\mathbf{0}\sigma}\rangle. \tag{B.7}$$

Here, $\sigma = \pm$, $\langle \mathbf{r}|\phi_{n\sigma}; u_{n\mathbf{0}\sigma}\rangle = \sqrt{v_0}\phi_{n\sigma}(\mathbf{r})\, u_{n\mathbf{0}\sigma}(\mathbf{r})$ is the product of envelope function and $\mathbf{k} = \mathbf{0}$ Bloch amplitude in band $n$ (CB, HH, LH or SO), the prefactors $\lambda_n^\sigma$ describe the degree of band hybridization, and $\mathcal{N}_\sigma$ enforces proper normalization.

In first order quasi-degenerate perturbation theory, the hybridization with the CB and the LH and SO sub-bands is described by the interaction terms $V_1$, $V_4$, and $V_5$ in Eq. (B.4), respectively. We estimate the degree of hybridization by applying these operators to a two-spinor containing the in-plane ground-state envelope function (B.2) of the HH sub-band. For the hybridization with the conduction band, we find (for $\mathbf{B} = \mathbf{0}$)

$$-\frac{1}{E_g} V_1 \begin{pmatrix} \phi_\rho(\rho) \\ \phi_\rho(\rho) \end{pmatrix} = \begin{pmatrix} \lambda_{\mathrm{CB}}^{+}\, \phi_{\mathrm{CB}\rho+}(\rho) \\ \lambda_{\mathrm{CB}}^{-}\, \phi_{\mathrm{CB}\rho-}(\rho) \end{pmatrix}, \tag{B.8}$$

where

$$\phi_{\mathrm{CB}\rho\pm}(\rho) = \frac{i}{\sqrt{2}}(\psi_{10}(\rho) \pm i\psi_{01}(\rho)). \tag{B.9}$$

Here, $\psi_{nm}(\rho) = \psi_n(x)\,\psi_m(y)$ and $\psi_n(x)$ is the $n^{\mathrm{th}}$ harmonic-oscillator eigenstate. The envelope function of the admixed CB state is a superposition of *excited* harmonic-oscillator eigenfunctions. The prefactor

$$\lambda_{\mathrm{CB}}^{\pm} = \pm\frac{P}{\sqrt{2}E_g l_0} \tag{B.10}$$

determines the degree of *sp*-hybridization. Using values from Table B.1 and assuming a quantum dot with dot Bohr radius $l_0 \simeq 30\,\mathrm{nm}$ ($\mathbf{B} = \mathbf{0}$), we estimate $\lambda_{\mathrm{CB}}^{\pm} \simeq 10^{-2}$. Similarly, we

| | | | |
|---|---|---|---|
| $P\,(e\text{V\AA})$ | $10.5^\star$ | $\gamma_1'$ | $6.98^\dagger$ |
| $E_g\,(e\text{V})$ | $1.52^\star$ | $\gamma_2'$ | $2.06^\dagger$ |
| $\Delta_{\text{SO}}\,(e\text{V})$ | $0.34^\star$ | $\gamma_3'$ | $2.93^\dagger$ |

Table B.1: Values of band parameters used in this section; $^\star$ taken from Winkler (2003); $^\dagger$ taken from Vurgaftman et al. (2001).

estimate $\lambda_{\text{LH}}^{\pm} \simeq \lambda_{\text{SO}}^{\pm} \simeq 10^{-3}$, assuming a dot height $a_z \simeq 5\,\text{nm}$. The admixture of CB, LH and SO states to the HH state is thus on the order of 1% and has therefore been neglected in our considerations.

We emphasize that *sp*-hybridization will lead to a coupling of the HH to the nuclear spins via the Fermi contact interaction (5.2). Since the Fermi contact interaction is of Heisenberg-type, *sp*-hybridization will directly lead to non-Ising corrections to the effective Hamiltonian given in Eq. (5.1). The size of these corrections is determined by the degree of *sp*-hybridization which is on the order of 1% (see above).

## B.2 Estimate of the Fermi contact interaction

In Eq. (5.15), we have approximated the HH $\mathbf{k} = \mathbf{0}$ Bloch amplitudes within a Wigner-Seitz cell by a linear combination of atomic orbitals. Similarly, we approximate the $\mathbf{k} = \mathbf{0}$ Bloch amplitude in the CB by

$$u_{\text{CB}\mathbf{0}\sigma}(\mathbf{r})\Big|_{\mathbf{r}\in\text{WS}} = N_{\alpha_c}\Big(\alpha_c \Psi_{400}^{\text{Ga}}(\mathbf{r}+\mathbf{d}/2) - \sqrt{1-\alpha_c^2}\,\Psi_{400}^{\text{As}}(\mathbf{r}-\mathbf{d}/2)\Big), \tag{B.11}$$

independent of $\sigma$. Here, $\Psi_{400}(\mathbf{r}) = R_{40}(r)Y_0^0(\theta,\varphi)$, $\alpha_c$ describes the relative electron sharing between the Ga and As atom in the Wigner-Seitz cell chosen to be centered halfway along the Ga-As bond, and $N_{\alpha_c}$ normalizes the Bloch amplitude to two atoms in a primitive unit cell. The radial wavefunction depends implicitly on the effective nuclear charges $Z_{\text{eff}}(\kappa, 4s)$, where $\kappa = \text{Ga}, \text{As}$.

We will estimate the relative electron sharing in the CB by calculating the electron densities at the sites of the nuclei from Eq. (B.11) and comparing to accepted values taken from Paget et al. (1977). We will then estimate the Fermi contact interaction of a CB electron using free-atom effective nuclear charges taken from Clementi and Raimondi (1963) ($Z_{\text{eff}}(\text{Ga}, 4s) \simeq 7.1$, $Z_{\text{eff}}(\text{Ga}, 4p) \simeq 6.2$, $Z_{\text{eff}}(\text{As}, 4s) \simeq 8.9$, and $Z_{\text{eff}}(\text{As}, 4p) \simeq 7.4$) and normalizing the Bloch amplitude over a Wigner-Seitz cell.

We approximate the electron densities at the Ga and As sites within a primitive unit cell from Eq. (B.11):

$$d_{\text{Ga}} = |u_{\text{CB}\mathbf{0}\sigma}(-\mathbf{d}/2)|^2 \simeq N_{\alpha_c}^2 \alpha_c^2 |\Psi_{400}^{\text{Ga}}(\mathbf{0})|^2, \tag{B.12}$$

$$d_{\text{As}} = |u_{\text{CB}\mathbf{0}\sigma}(+\mathbf{d}/2)|^2 \simeq N_{\alpha_c}^2 (1-\alpha_c^2) |\Psi_{400}^{\text{As}}(\mathbf{0})|^2. \tag{B.13}$$

We estimate the corrections to the right-hand sides to be on the order of 1% due to overlap terms. We take the ratio $d_{\text{Ga}}/d_{\text{As}}$ and equate this with the ratio of the values from Paget et al.

(1977), $d'_{\mathrm{Ga}} = 5.8 \times 10^{-31}\ \mathrm{m}^{-3}$ and $d'_{\mathrm{As}} = 9.8 \times 10^{-31}\ \mathrm{m}^{-3}$. This allows us to write $\alpha_c$ as a function of the two effective nuclear charges:

$$\alpha_c = \left[1 + \frac{d'_{\mathrm{As}}}{d'_{\mathrm{Ga}}} \left( \frac{Z_{\mathrm{eff}}(\mathrm{Ga}, 4s)}{Z_{\mathrm{eff}}(\mathrm{As}, 4s)} \right)^3 \right]^{-1/2}. \tag{B.14}$$

Recalling that $N_{\alpha_c}$ normalizes the Bloch amplitude to two atoms over a Wigner-Seitz cell, we write

$$N_{\alpha_c} = \left[ \frac{1}{2} \int_{\mathrm{WS}} d^3 r \left| \alpha_c \Psi^{\mathrm{Ga}}_{400}(\mathbf{r} + \mathbf{d}/2) - \sqrt{1 - \alpha_c^2} \Psi^{\mathrm{As}}_{400}(\mathbf{r} - \mathbf{d}/2) \right|^2 \right]^{-1/2}. \tag{B.15}$$

For all numerical integrations, we approximate the Wigner-Seitz cell by a sphere centered halfway along the Ga-As bond with radius equal to half the Ga-Ga nearest-neighbor distance. Inserting (B.14) and (B.15) into (B.12) and (B.13), we solve the two coupled equations

$$d_{\mathrm{Ga}}(Z_{\mathrm{eff}}(\mathrm{Ga}), Z_{\mathrm{eff}}(\mathrm{As})) - d'_{\mathrm{Ga}} = 0, \tag{B.16}$$

$$d_{\mathrm{As}}(Z_{\mathrm{eff}}(\mathrm{Ga}), Z_{\mathrm{eff}}(\mathrm{As})) - d'_{\mathrm{As}} = 0, \tag{B.17}$$

for the two effective nuclear charges. This yields $Z_{\mathrm{eff}}(\mathrm{Ga}) \simeq 9.8$ and $Z_{\mathrm{eff}}(\mathrm{As}) \simeq 11.0$. Inserting these values back into Eq. (B.14), we estimate the electron sharing within the primitive unit cell to be

$$\alpha_c^2 \simeq 0.46. \tag{B.18}$$

For comparison, inserting free-atom effective nuclear charges into Eq. (B.14) yields a similar value: $\alpha_c'^2 \simeq 0.54$.

Now we estimate the Fermi contact interaction of a CB electron starting from the free-atom effective nuclear charges $Z_{\mathrm{eff}}(\kappa, 4s)$ obtained from Clementi and Raimondi (1963). We use $\alpha_c \simeq 1/\sqrt{2}$ and normalize the $\mathbf{k} = \mathbf{0}$ Bloch amplitude to two atoms over a Wigner-Seitz cell, following Eq. (B.15). From the normalized Bloch amplitudes we estimate the Fermi contact hyperfine interaction by evaluating

$$A_e^j = \frac{2\mu_0}{3} \gamma_S \gamma_j |u_{\mathrm{CB}\mathbf{0}\sigma}(\mathbf{R}_j)|^2. \tag{B.19}$$

Here, $\mathbf{R}_j = \mp \mathbf{d}/2$ for Ga and As, respectively ($j$ indexes the nuclear isotope). Evaluating for the isotopes in GaAs, this gives the values shown in column (iii) of Table 5.1.

Replacing the Wigner-Seitz cell by a sphere with radius $R_s$ equal to half the Ga-Ga nearest-neighbor distance in our numerical integrations overestimates the expectation value of $[r_k^3(1 + d/r_k)]^{-1}$ in Eq. (5.10). To estimate the error, we perform an integration over a sphere with radius $R'_s = (R_s + R_{\mathrm{max}})/2$, where $R_{\mathrm{max}}$ denotes the radius of the smallest sphere that fully contains the Wigner-Seitz cell. From this, we estimate the relative error to be less than 30%.

## B.3 Estimate of the long-ranged interactions

In this section, we estimate the corrections to the HH coupling strength in Eq. (5.10) due to long-ranged dipole-dipole interactions and long-ranged $\mathbf{L} \cdot \mathbf{I}$ interactions. To this end, we

consider a single nucleus interacting with a HH that is delocalized over the lattice sites in the quantum dot. We start from the Hamiltonians given in Eqs. (5.3) and (5.4). We define effective radii $a_{\rm eff}(\kappa, 4p) = a_0/Z_{\rm eff}(\kappa, 4p)$, where $a_0 \simeq 5.3 \times 10^{-11}\,$m is the Bohr radius. The effective radii define an approximate length scale for the spread of the site-localized functions $\Psi^{\kappa}_{41\sigma}(\mathbf{r})$ and are much smaller than the GaAs lattice constant $a_L \simeq 5.7 \times 10^{-10}\,$m. The nucleus thus effectively 'sees' sharp-peaked electron densities centered around the more distant lattice sites. We choose the nucleus to be at site $\mathbf{R}_k$ and estimate the interaction with the electron density at more distant atomic sites by approximating the electron densities by $\delta$-functions. Adding up contributions from $h_2^k$ and $h_3^k$, we arrive at an effective Hamiltonian describing the long-ranged interactions: $H_{\rm lr}^k = A_{\rm lr}^k s_z I_k^z$, where $A_{\rm lr}^k = \sum_{l;l\neq k} A_{\rm lr}^{kl}$ is the associated coupling strength and $A_{\rm lr}^{kl} = v_0|\phi(\mathbf{R}_l)|^2 \int d^3r_k \{\delta(\mathbf{r}_k - \mathbf{R}_{kl})(h_2^k + h_3^k)\}$ describes the coupling of the electron density at site $\mathbf{R}_l$ to the nucleus at site $\mathbf{R}_k$ ($\mathbf{R}_{kl} = \mathbf{R}_l - \mathbf{R}_k$). In order to estimate the size of the long-ranged interactions relative to the on-site interactions, we take into account nearest-neighbor couplings for the long-ranged part, i.e., we replace $\sum_{l;l\neq k} \to \sum_{l=\text{n.n.}}$. The interaction with electron density located around more distant nuclei is suppressed by $\sim 1/R_{kl}^3$. Assuming that the quantum-dot envelope function varies slowly over the nearest-neighbor distance ($\phi(\mathbf{R}_l) \simeq \phi(\mathbf{R}_k)$ for $l$ nearest neighbor of $k$), we estimate the ratio of long-ranged and on-site interactions (Table 5.1, column (i)) to be

$$\frac{A_{\rm lr}}{A_h} \simeq 7 \times 10^{-3}, \tag{B.20}$$

on the order of 1%, where $A_{\rm lr}^k = A_{\rm lr} v_0 |\phi(\mathbf{R}_k)|^2$.

We remark that, in principle, the electron g-factor can deviate from the free-electron g-factor due to spin-orbit interaction. According to Yafet (1961), this renormalization is negligible for the on-site interaction, but could become relevant for the long-ranged interaction. However, for the estimate in Eq. (B.20), we have taken the free-electron g-factor.

## B.4 Variance of the nuclear field

Here we calculate the nuclear-field variance for a HH interacting with nuclei in a quantum dot. In particular, we evaluate

$$\sigma^2 = \left\langle h_z^2 \right\rangle, \tag{B.21}$$

where $\langle \cdots \rangle = \mathrm{Tr}_I\,(\bar{\rho}_I \cdots)$ indicates the expectation value with respect to the infinite-temperature thermal equilibrium density matrix $\bar{\rho}_I$ and we recall $h_z = \sum_k A_k^h I_k^z$. For an uncorrelated and unpolarized nuclear state, we have $\left\langle I_k^z I_{k'}^z \right\rangle = \left\langle I_k^z \right\rangle \left\langle I_{k'}^z \right\rangle = 0,\ k \neq k'$, which gives

$$\sigma^2 = \sum_k \left(A_k^h\right)^2 \langle (I_k^z)^2 \rangle. \tag{B.22}$$

Using $\langle (I_k^z)^2 \rangle = I^{j_k}\left(I^{j_k}+1\right)/3$ for an infinite-temperature state, $A_k^h = A_h^{j_k} v_0 |\phi(\mathbf{R}_k)|^2$, and assuming that the nuclear isotopic species with abundances $\nu_j$ are distributed uniformly throughout the dot gives

$$\sigma^2 = \frac{1}{3} I_0 \sum_j \nu_j I^j (I^j+1)(A_h^j)^2, \tag{B.23}$$

where

$$I_0 = v_0^2 \sum_k |\phi(\mathbf{R}_k)|^4. \tag{B.24}$$

Assuming that the envelope function $\phi(\mathbf{r})$ varies slowly on the scale of the lattice, we replace the sum in Eq. (B.24) by an integral:

$$v_0 \sum_k |\phi(\mathbf{R}_k)|^4 \to \int d^3r |\phi(\mathbf{r})|^4. \tag{B.25}$$

Inserting the envelope functions (B.2) and (B.3) for a quantum dot with height $a_z$ and radius $l$ and evaluating the integral in Eq. (B.25), we find

$$I_0 = \frac{3}{4}\frac{1}{N}. \tag{B.26}$$

Here, $N$ is the number of nuclear spins within the quantum dot, given explicitly by

$$N = \frac{\pi l^2 a_z}{v_0}. \tag{B.27}$$

Inserting Eq. (B.26) into Eq. (B.23) directly gives Eq. (5.12).

## B.5 Band hybridization

In this section, we show how to derive the hybridized heavy-hole states from the $8 \times 8$ Kane Hamiltonian. In Appendix B.1, we have written the Kane Hamiltonian in the two-dimensional limit by replacing powers of the crystal momentum $k_z$ by expectation values. This is a good assumption as long as one is only interested in an order-of-magnitude estimate of the degree of hybridization (such as in Chapter 5). In order to capture the correct parameter dependence of the degree of band hybridization, however, it is necessary to start from the bulk version of the Kane Hamiltonian, which reads (Winkler, 2003)

$$H_K = \begin{pmatrix} H_{\mathrm{CB}} & V_1 & V_2 & V_3 \\ V_1^\dagger & H_{\mathrm{HH}} & V_4 & V_5 \\ V_2^\dagger & V_4^\dagger & H_{\mathrm{LH}} & V_6 \\ V_3^\dagger & V_5^\dagger & V_6^\dagger & H_{\mathrm{SO}} \end{pmatrix}, \tag{B.28}$$

where the relevant blocks are given by

$$H_{\mathrm{HH}} = \begin{pmatrix} B & 0 \\ 0 & B \end{pmatrix}, \qquad V_1 = \tfrac{1}{\sqrt{2}} \begin{pmatrix} -E & 0 \\ 0 & E^* \end{pmatrix},$$
$$V_4 = \begin{pmatrix} 2\sqrt{3}\,J & \sqrt{3}\,F \\ \sqrt{3}\,F^* & -2\sqrt{3}\,J^* \end{pmatrix}, \quad V_5 = \begin{pmatrix} -\sqrt{6}\,J & -\sqrt{6}\,F \\ \sqrt{6}\,F^* & -\sqrt{6}\,J^* \end{pmatrix},$$

with

$$\begin{aligned} B &= -\epsilon[(\gamma_1 + \gamma_2)(k_x^2 + k_y^2) + (\gamma_1 - 2\gamma_2)k_z^2], \\ E &= Pk_+, \\ F &= \epsilon[\gamma_2(k_x^2 - k_y^2) - 2i\gamma_3 k_x k_y], \\ J &= \epsilon\gamma_3 k_- k_z. \end{aligned}$$

Here, $\epsilon = \hbar^2/2m_0$, $m_0$ is the free-electron mass, $k_\pm = k_x \pm ik_y$, $\gamma_j$ denote the Luttinger parameters, and $P$ is the inter-band momentum.

We choose a parabolic confinement potential

$$V_{\rm dot} = V_z(z)V_{xy}(x,y), \qquad V_z(z) = \frac{m_\perp \omega_\perp}{2} z^2, \quad V_{xy}(x,y) = \frac{m_\parallel \omega_\parallel}{2}(x^2+y^2), \tag{B.29}$$

where $\omega_\perp = \hbar/(m_\perp a_z^2)$ and $\omega_\parallel = \hbar/(m_\parallel L^2)$ with HH effective masses $m_\perp = m_0/(\gamma_1 - 2\gamma_2)$ and $m_\parallel = m_0/(\gamma_1+\gamma_2)$ along the growth direction and in the plane of the dot, respectively, and $a_z$ and $L$ denote the accordant confinement lengths.

In order to calculate the hybridized HH states perturbatively, we take the eigenfunction of $H_{\rm HH} + V_{\rm dot}$ as the unperturbed envelope function, whose position representation is given by

$$\langle \mathbf{r} | \phi^{00}_{\rm HH} \rangle = \phi^0_{\rm HH}(z)\phi^0_{\rm HH}(x,y), \tag{B.30}$$

with harmonic-oscillator eigenfunctions

$$\phi^0_{\rm HH}(z) = \frac{1}{\sqrt{\sqrt{\pi} a_z}} \exp\left\{-\frac{1}{2}\frac{z^2}{a_z^2}\right\}, \qquad \phi^0_{\rm HH}(x,y) = \frac{1}{\sqrt{\pi}L} \exp\left\{-\frac{1}{2}\frac{x^2+y^2}{L^2}\right\}. \tag{B.31}$$

The hybridized HH states can now be evaluated by a perturbation expansion as follows: defining a two-spinor $|\Psi_0\rangle = (|\phi^{00}_{\rm HH}\rangle, |\phi^{00}_{\rm HH}\rangle)^t$, the hybridized HH spin states are the components of

$$|\Psi_{\rm hyb}\rangle = \sum_n \left( -\frac{1}{E_g} |\Psi^n_{\rm CB}\rangle\langle\Psi^n_{\rm CB}| V_1 + \frac{1}{\Delta_{\rm LH}} |\Psi^n_{\rm LH}\rangle\langle\Psi^n_{\rm LH}| V_4^\dagger + \frac{1}{\Delta_{\rm LH}+\Delta_{\rm SO}} |\Psi^n_{\rm SO}\rangle\langle\Psi^n_{\rm SO}| V_5^\dagger \right) |\Psi_0\rangle. \tag{B.32}$$

The summation runs, in principle, over all states in the accordant band. However, due to the cylindrical symmetry of the dot, only one matrix element per band yields a non-vanishing contribution to the sum. For instance, $\langle \phi^{00}_{\rm CB} | k_\pm | \phi^{00}_{\rm HH}\rangle = 0$ due to the vanishing angular integral, but $\langle \phi^{0\pm}_{\rm CB} | k_\pm | \phi^{00}_{\rm HH}\rangle \neq 0$. From the overlap integrals, we obtain the factors $\beta_{\rm CB}$ and $\beta_{\rm LH}$ (for the CB and LH contributions) given in Eq. (6.3) of the main text.

The HH-LH splitting $\Delta_{\rm LH}$ is given by the difference in ground-state energies in the HH and LH bands: $\Delta_{\rm LH} = E_{\rm HH} - E_{\rm LH}$, where

$$E_{\rm HH} = -\frac{\hbar^2}{2}\left(2\frac{\gamma_1+\gamma_2}{m_0 L^2} + \frac{\gamma_1 - 2\gamma_2}{m_0 a_z^2}\right), \qquad E_{\rm LH} = -\frac{\hbar^2}{2}\left(2\frac{\gamma_1-\gamma_2}{m_0 L^2} + \frac{\gamma_1+2\gamma_2}{m_0 a_z^2}\right). \tag{B.33}$$

This leads to a HH-LH splitting of

$$\Delta_{\rm LH} = \frac{2\hbar^2\gamma_2}{m_0}\frac{L^2 - a_z^2}{L^2 a_z^2}. \tag{B.34}$$

Carrying out the perturbation expansion following Eq. (B.32) and inserting the quantities given above, we arrive at the hybridized states given in Eq. (6.1) of the main text.

## B.6 Continuum limit

Here we show in detail how to calculate the decoherence rate $\Gamma = 1/T_2$ from the fourth-order self-energy in the continuum limit. We start from Eq. (6.18),

$$\Sigma^{(4)}(s + i\omega_n) \simeq -i\frac{c_+c_-}{4\omega_n^2} \sum_{k_1,k_2} \frac{|A_{k_1}^{\pm}|^2 |A_{k_2}^{\pm}|^2}{s + i(A_{k_1}^z - A_{k_2}^z)} \tag{B.35}$$

We now replace sums by integrals according to $v_0 \sum_k \to \int d^3r$, where $v_0$ is the volume occupied by one nucleus and the integration is carried out over all space. Averaging over the $z$-dependence of the coupling constants, $A(x,y) = \int_{-\infty}^{\infty} dz\, A(x,y,z)$ we write $\Sigma^{(4)}$ in terms of a four-dimensional spatial integral:

$$\Sigma^{(4)}(s + i\omega_n) \simeq -i\frac{c_+c_-}{4\pi^2 N} \frac{A_\perp^4}{\omega_n^2 A_z} \times \int_0^\infty dr_1 r_1 \int_0^\infty dr_2 r_2 \int_0^{2\pi} d\theta_1 \int_0^{2\pi} d\theta_2 \, \frac{r_1^4 r_2^4 e^{-2r_1^2} e^{-2r_2^2}}{\mathsf{s} + i(e^{-r_1^2} - e^{-2r_2^2})}, \tag{B.36}$$

where we have introduced spherical coordinates $x_i = r_i \cos\theta_i$, $y_i = r_i \sin\theta_i$, and where $\mathsf{s} = sN/A_z$. We have also rewritten $Nv_0 = \pi a_z L^2$ (the volume of the QD). The angular integrals simply contribute a prefactor of $4\pi^2$. The radial integrals can be solved by introducing new variables $x = e^{-r_1^2}$, $y = e^{-r_2^2}$, such that

$$\Sigma^{(4)}(s + i\omega_n) \simeq -i\frac{c_+c_-}{4N} \frac{A_\perp^4}{\omega_n^2 A_z} \int_0^1 dx \int_0^1 dy \, \frac{x(\log x)^2 \, y(\log y)^2}{\mathsf{s} + i(x - y)}. \tag{B.37}$$

From our considerations in Chapters 3 and 4, we know that the right-hand side of the equation of motion in Laplace space,

$$S^+(s + i\omega_n) = \frac{\langle S^+ \rangle_0}{s + i\Sigma(s + i\omega_n)} \tag{B.38}$$

features a pole at $s = i\Delta\omega - \Gamma$, where $\Gamma = -\mathrm{Im}\Sigma^{(4)}(i\omega_n + i\Delta\omega - 0^+)$ and where $0^+$ denotes a positive infinitesimal. Evaluating $\Sigma^{(4)}$ at $s = i\omega_n + i\Delta\omega - 0^+$ and using

$$\lim_{\eta\to 0} \frac{1}{\xi \pm i\eta} = \mathcal{P}\frac{1}{\xi} \mp i\pi\delta(\xi), \tag{B.39}$$

where $\mathcal{P}$ denotes that the principle value should be taken in any integration involving the above expression, we arrive at an integral of the form

$$I = \int_0^1 dx \int_0^1 dy \, f(x,y) \left( \mathcal{P}\frac{1}{x - y + \Delta\omega} - i\pi\delta(x - y + \Delta\omega) \right), \tag{B.40}$$

Taking the imaginary part according to $\Gamma = -\mathrm{Im}\Sigma^{(4)}(i\omega_n + i\Delta\omega - 0^+)$ leads directly to Eq. (6.21) of the main text.

# Curriculum Vitae

## Jan Fischer

Date of birth: August 5, 1980

Place of birth: Freiburg i. Br., Germany

Citizenship: German

## Education

2006-2010 Ph.D. in Theoretical Physics, University of Basel, Switzerland
Advisor: Prof. Daniel Loss
Thesis: *Spin Decoherence of Electrons and Holes in Semiconductor Quantum Dots*

2000-2006 Diploma in Physics, Albert-Ludwigs-Universität Freiburg, Germany
Advisor: Prof. Heinz-Peter Breuer
Thesis: *Projektionsoperatormethoden in der Analyse der Dynamik von Spinbädern*

1999-2000 Civil Service (Gaggenau, Germany)

1990-1999 Abitur at the Markgraf-Ludwig-Gymnasium (Baden-Baden, Germany)

# List of Publications

*(∗) Publication covered in this thesis*

(∗) J. Fischer and D. Loss. *Hybridization and spin decoherence in heavy-hole quantum dots*. arXiv:1009.5195v1 [cond-mat.mes-hall].

(∗) W. A. Coish, J. Fischer, and D. Loss. *Free-induction decay and envelope modulations in a narrowed nuclear spin bath*. Phys. Rev. B **81**, 165315 (2010).

(∗) J. Fischer, B. Trauzettel, and D. Loss. *Hyperfine interaction and electron-spin decoherence in graphene and carbon nanotube quantum dots*. Phys. Rev. B **80**, 155401 (2009).

(∗) J. Fischer and D. Loss. *Dealing with Decoherence*. Science **324**, 1277 (2009).

J. Fischer, M. Trif, W. A. Coish, and D. Loss. *Spin interactions, relaxation and decoherence in quantum dots*. Solid State Communications **149**, 1443 (2009).

(∗) J. Fischer, W. A. Coish, D. V. Bulaev, and D. Loss. *Spin decoherence of a heavy hole coupled to nuclear spins in a quantum dot*. Phys. Rev. B **78**, 155329 (2008).

(∗) W. A. Coish, J. Fischer, and D. Loss. *Exponential decay in a spin bath*. Phys. Rev. B **77**, 125329 (2008).

J. Fischer and H.-P. Breuer. *Correlated projection operator approach to non-Markovian dynamics in spin baths*. Phys. Rev. A **76**, 052119 (2007).

# Acknowledgments

*See print version.*

# Bibliography


E. Abe, K. M. Itoh, J. Isoya, and S. Yamasaki. Electron-spin phase relaxation of phosphorus donors in nuclear-spin-enriched silicon. *Phys. Rev. B*, 70:033204, 2004.

A. Abragam. *The Principles of Nuclear Magnetism.* Oxford University Press, 1961. Section VI.II.

K. A. Al-Hassanieh, V. V. Dobrovitski, E. Dagotto, and B. N. Harmon. Numerical modeling of the central spin problem using the spin-coherent-state p representation. *Phys. Rev. Lett.*, 97:37204, 2006.

S. Amasha, K. MacLean, Iuliana P. Radu, D. M. Zumbuhl, M. A. Kastner, M. P. Hanson, and A. C. Gossard. Electrical control of spin relaxation in a quantum dot. *Phys. Rev. Lett.*, 100: 046803, 2008.

A. Ardavan, O. Rival, J. J. L. Morton, S. J. Blundell, A. M. Tyryshkin, G. A. Timco, and R. E. P. Winpenny. Will spin-relaxation times in molecular magnets permit quantum information processing? *Phys. Rev. Lett.*, 98:057201, 2007.

M. J. Biercuk, S. Garaj, N. Mason, J. M. Chow, and C. M. Marcus. Gate-defined quantum dots on carbon nanotubes. *Nano Lett.*, 5:1267, 2005.

M. Bockrath, D. H. Cobden, P. L. McEuen, N. G. Chopra, A. Zettl, A. Thess, and R. E. Smalley. Single-electron transport in ropes of carbon nanotubes. *Science*, 275:1922, 1997.

A. S. Bracker, E. A. Stinaff, D. Gammon, M. E. Ware, J. G. Tischler, A. Shabaev, Al. L. Efros, D. Park, D. Gershoni, V. L. Korenev, and I. A. Merkulov. Optical pumping of the electronic and nuclear spin of single charge-tunable quantum dots. *Phys. Rev. Lett.*, 94:047402, 2005.

B. Braunecker, P. Simon, and D. Loss. Nuclear magnetism and electronic order in $^{13}$C nanotubes. *Phys. Rev. Lett.*, 102:116403, 2009a.

B. Braunecker, P. Simon, and D. Loss. Nuclear magnetism and electron order in interacting one-dimensional conductors. *Phys. Rev. B*, 80:165119, 2009b.

H.-P. Breuer. Non-Markovian generalization of the Lindblad theory of open quantum systems. *Phys. Rev. A*, 75:022103, 2007.

H.-P. Breuer and F. Petruccione. *The Theory of Open Quantum Systems*. Oxford University Press, Oxford, UK, 2002.

H.-P. Breuer, D. Burgarth, and F. Petruccione. Non-Markovian dynamics in a spin star system: exact solution and approximation techniques. *Phys. Rev. B*, 70:045323, 2004.

H.-P Breuer, J. Gemmer, and M. Michel. Non-Markovian quantum dynamics: correlated projection superoperators and Hilbert space averaging. *Phys. Rev. E*, 73:016139, 2006.

D. Brunner, B. D. Gerardot, P. A. Dalgarno, G. Wüst, K. Karrai, N. G. Stoltz, P. M. Petroff, and R. J. Warburton. A coherent single-hole spin in a semiconductor. *Science*, 325:5936, 2009.

D. V. Bulaev and D. Loss. Spin relaxation and decoherence of holes in quantum dots. *Phys. Rev. Lett.*, 95:076805, 2005.

D. V. Bulaev and D. Loss. Electric dipole spin resonance for heavy holes in quantum dots. *Phys. Rev. Lett.*, 98:097202, 2007.

D. V. Bulaev, B. Trauzettel, and D. Loss. Spin-orbit interaction and anomalous spin relaxation in carbon nanotube quantum dots. *Phys. Rev. B*, 77:235301, 2008.

Guido Burkard. Positively spin coherent. *Nature Materials*, 7:100, 2008.

J. Cao, Q. Wang, and H. Dai. Electron transport in very clean, as-grown suspended carbon nanotubes. *Nature Materials*, 4:745, 2005.

V. Cerletti, W. A. Coish, O. Gywat, and D. Loss. Recipes for spin-based quantum computing. *Nanotechnology*, 16:R27, 2005.

G. Chen, D. L. Bergman, and L. Balents. Semiclassical dynamics and long time asymptotics of the central-spin problem in a quantum dot. *Phys. Rev. B*, 76:045312, 2007.

L. Childress, M. V. Gurudev Dutt, J. M. Taylor, A. S. Zibrov, F. Jelezko, J. Wrachtrup, P. R. Hemmer, and M. D. Lukin. Coherent dynamics of coupled electron and nuclear spin qubits in diamond. *Science*, 314:281, 2006.

H. O. H. Churchill, A. J. Bestwick, J. W. Harlow, F. Kuemmeth, D. Marcos, C. H. Stwertka, S. K. Watson, and C. M. Marcus. Electron-nuclear interaction in $^{13}$C nanotube double quantum dots. *Nature Physics*, 5:321, 2009a.

H. O. H. Churchill, F. Kuemmeth, J. W. Harlow, A. J. Bestwick, E. I. Rashba, K. Flensberg, C. H. Stwertka, T. Taychatanapat, S. K. Watson, and C. M. Marcus. Relaxation and dephasing in a two-electron $^{13}$C nanotube double quantum dot. *Phys. Rev. Lett.*, 102:166802, 2009b.

E. Clementi and D. L. Raimondi. Atomic screening constants from SCF functions. *J. Chem. Phys.*, 38:2686, 1963.

W. A. Coish and J. Baugh. Nuclear spins in nanostructures. *physica status solidi (b)*, 246: 2203, 2009.

W. A. Coish and Daniel Loss. Hyperfine interaction in a quantum dot: Non-Markovian electron spin dynamics. *Phys. Rev. B*, 70:195340, 2004.

W. A. Coish, J. Fischer, and D. Loss. Exponential decay in a spin bath. *Phys. Rev. B*, 77: 125329, 2008.

W. A. Coish, Jan Fischer, and Daniel Loss. Free-induction decay and envelope modulations in a narrowed nuclear spin bath. *Phys. Rev. B*, 81:165315, 2010.

Ł. Cywiński, W. M. Witzel, and S. Das Sarma. Electron spin dephasing due to hyperfine interactions with a nuclear spin bath. *Phys. Rev. Lett.*, 102:057601, 2009a.

Ł. Cywiński, W. M. Witzel, and S. Das Sarma. Pure quantum dephasing of a solid-state electron spin qubit in a large nuclear spin bath coupled by long-range hyperfine-mediated interactions. *Phys. Rev. B*, 79:245314, 2009b.

R. de Sousa and S. Das Sarma. Theory of nuclear-induced spectral diffusion: Spin decoherence of phosphorus donors in Si and GaAs quantum dots. *Phys. Rev. B*, 68:115322, 2003.

C. Deng and X. Hu. Analytical solution of electron spin decoherence through hyperfine interaction in a quantum dot. *Phys. Rev. B*, 73:241303, 2006.

C. Deng and X. Hu. Electron-spin dephasing via hyperfine interaction in a quantum dot: An equation-of-motion calculation of electron-spin correlation functions. *Phys. Rev. B*, 78: 245301, 2008.

D. P. DiVincenzo and D. Loss. Rigorous Born approximation and beyond for the spin-boson model. *Phys. Rev. B*, 71:035318, 2005.

M. S. Dresselhaus, G. Dresselhaus, and A. Jorio. *Group Theory: Application to the Physics of Condensed Matter*. Springer-Verlag, 2008.

B. Eble, C. Testelin, P. Desfonds, F. Bernardot, A. Balocchi, T. Amand, A. Miard, A. Lemaître, X. Marie, and M. Chamarro. Hole–nuclear spin interaction in quantum dots. *Phys. Rev. Lett.*, 102:146601, 2009.

S. I. Erlingsson and Y. V. Nazarov. Evolution of localized electron spin in a nuclear spin environment. *Phys. Rev. B*, 70:205327, 2004.

E. Ferraro, H.-P. Breuer, A. Napoli, M. A. Jivulescu, and A. Messina. Non-Markovian dynamics of a single electron spin coupled to a nuclear spin bath. *Phys. Rev. B*, 78:064309, 2008.

E. Fick and G. Sauermann. *The Quantum Statistics of Dynamic Processes*. Springer-Verlag, Berlin, 1990.

J. Fischer and H.-P. Breuer. Correlated projection operator approach to non-Markovian dynamics in spin baths. *Phys. Rev. A*, 76:052119, 2007.

J. Fischer, W. A. Coish, D. V. Bulaev, and D. Loss. Spin decoherence of a heavy hole coupled to nuclear spins in a quantum dot. *Phys. Rev. B*, 78:155329, 2008.

J. Fischer, B. Trauzettel, and D. Loss. Hyperfine interaction and electron-spin decoherence in graphene and carbon nanotube quantum dots. *Phys. Rev. B*, 80:155401, 2009.

T. Flissikowski, I. A. Akimov, A. Hundt, and F. Henneberger. Single-hole spin relaxation in a quantum dot. *Phys. Rev. B*, 68:161309, 2003.

B. D. Gerardot, D. Brunner, P. A. Dalgarno, P. Öhberg, S. Seidl, M. Kroner, K. Karrai, N. G. Stoltz, P. M. Petroff, and R. J. Warburton. Optical pumping of a single hole spin in a quantum dot. *Nature*, 451:441, 2008.

G. Giedke, J. M. Taylor, D. D'Alessandro, M. D. Lukin, and A. Imamoğlu. Quantum measurement of a mesoscopic spin ensemble. *Phys. Rev. A*, 74:032316, 2006.

C. Goze-Bac, S. Latil, P. Lauginie, V. Jourdain, J. Conard, L. Duclaux, A. Rubio, and P. Bernier. Magnetic interactions in carbon nanostructures. *Carbon*, 40:1825, 2002.

M. R. Gräber, W. A. Coish, C. Hoffmann, M. Weiss, J. Furer, S. Oberholzer, D. Loss, and C. Schönenberger. Molecular states in carbon nanotube double quantum dots. *Phys. Rev. B*, 74:075427, 2006.

A. Greilich, D. R. Yakovlev, A. Shabaev, Al. L. Efros, I. A. Yugova, R. Oulton, V. Stavarache, D. Reuter, A. Wieck, and M. Bayer. Mode locking of electron spin coherences in singly charged quantum dots. *Science*, 313:5785, 2006.

A. Greilich, A. Shabaev, D. R. Yakovlev, Al. L. Efros, I. A. Yugova, D. Reuter, A. D. Wieck, and M. Bayer. Nuclei-induced frequency focusing of electron spin coherence. *Science*, 317: 1896, 2007.

A. Greilich, S. E. Economou, S. Spatzek, D. R. Yakovlev, D. Reuter, A. D. Wieck, T. L. Reinecke, and M. Bayer. Ultrafast optical rotations of electron spins in quantum dots. *Nature Phys.*, 5:262, 2009.

L. K. Grover. Quantum mechanics helps in searching for a needle in a haystack. *Phys. Rev. Lett.*, 79:325, 1997.

M. Gueron. Density of the conduction electrons at the nuclei in indium antimonide. *Phys. Rev.*, 135:A200, 1964.

R. Hanson, F. M. Mendoza, R. J. Epstein, and D. D. Awschalom. Polarization and readout of coupled single spins in diamond. *Phys. Rev. Lett.*, 97:87601, 2006.

R. Hanson, L. P. Kouwenhoven, J. R. Petta, S. Tarucha, and L. M. K. Vandersypen. Spins in few-electron quantum dots. *Rev. Mod. Phys.*, 79:1217, 2007.

R. Hanson, V. V. Dobrovitski, A. E. Feiguin, O. Gywat, and D. D. Awschalom. Coherent dynamics of a single spin interacting with an adjustable spin bath. *Science*, 320:352, 2008.

D. Heiss, S. Schaeck, H. Huebl, M. Bichler, G. Abstreiter, J. J. Finley, D. V. Bulaev, and Daniel Loss. Observation of extremely slow hole spin relaxation in self-assembled quantum dots. *Phys. Rev. B*, 76:241306, 2007.

X. L. Huang and X. X. Yi. Non-Markovian effects on the geometric phase. *Europhys. Lett.*, 82:50001, 2008.

P. Jarillo-Herrero, S. Sapmaz, C. Dekker, L. P. Kouwenhoven, and H. S. J. van der Zant. Electron-hole symmetry in a semiconducting carbon nanotube quantum dot. *Nature*, 429: 389, 2004.

F. Jelezko, T. Gaebel, I. Popa, A. Gruber, and J. Wrachtrup. Observation of coherent oscillations in a single electron spin. *Phys. Rev. Lett.*, 92:076401, 2004.

H. I. Jørgensen, K. Grove-Rasmussen, J. R. Hauptmann, and P. E. Lindelof. Single wall carbon nanotube double quantum dot. *Appl. Phys. Lett.*, 89:232113, 2006.

O. N. Jouravlev and Y. V. Nazarov. Electron transport in a double quantum dot governed by a nuclear magnetic field. *Phys. Rev. Lett.*, 96:176804, 2006.

M. Karplus and G. K. Fraenkel. Theoretical interpretation of carbon-13 hyperfine interactions in electron spin resonance spectra. *J. Chem. Phys.*, 35:1312, 1961.

A. V. Khaetskii, D. Loss, and L. Glazman. Electron spin decoherence in quantum dots due to interaction with nuclei. *Phys. Rev. Lett.*, 88:186802, 2002.

A. V. Khaetskii, D. Loss, and L. Glazman. Electron spin evolution induced by interaction with nuclei in a quantum dot. *Phys. Rev. B*, 67:195329, 2003.

J. R. Klauder and P. W. Anderson. Spectral diffusion decay in spin resonance experiments. *Phys. Rev.*, 125:912, 1962.

D. Klauser, W. A. Coish, and D. Loss. Nuclear spin state narrowing via gate-controlled Rabi oscillations in a double quantum dot. *Phys. Rev. B*, 73:205302, 2006.

D. Klauser, W. A. Coish, and Daniel Loss. Nuclear spin dynamics and Zeno effect in quantum dots and defect centers. *Phys. Rev. B*, 78:205301, 2008.

A. Kleiner and S. Eggert. Curvature, hybridization, and STM images of carbon nanotubes. *Phys. Rev. B*, 64:113402, 2001.

Y. Komijani, M. Csontos, T. Ihn, K. Ensslin, D. Reuter, and A. D. Wieck. Observation of excited states in a p-type GaAs quantum dot. *Europhys. Lett.*, 84:57004, 2008.

J. Kong, C. Zhou, E. Yenilmez, and H. Dai. Alkaline metal-doped n-type semiconducting nanotubes as quantum dots. *Appl. Phys. Lett.*, 77:3977, 2000.

F. H. L. Koppens, C. Buizert, K. J. Tielrooij, I. T. Vink, K. C. Nowack, T. Meunier, L. P. Kouwenhoven, and L. M. K. Vandersypen. Driven coherent oscillations of a single electron spin in a quantum dot. *Nature*, 442:766, 2006.

F. H. L. Koppens, D. Klauser, W. A. Coish, K. C. Nowack, L. P. Kouwenhoven, D. Loss, and L. M. K. Vandersypen. Universal phase shift and nonexponential decay of driven single-spin oscillations. *Phys. Rev. Lett.*, 99:106803, 2007. see especially the associated auxiliary material (EPAPS Document No. E-PRLTAO-99-027736).

F. H. L. Koppens, K. C. Nowack, and L. M. K. Vandersypen. Spin echo of a single electron spin in a quantum dot. *Phys. Rev. Lett*, 100:236802, 2008.

F. Kuemmeth, S. Ilani, D. C. Ralph, and P. L. McEuen. Coupling of spin and orbital motion of electrons in carbon nanotubes. *Nature*, 452:448, 2008.

S. Latil, L. Henrard, C. Goze Bac, P. Bernier, and A. Rubio. C13 NMR chemical shift of single-wall carbon nanotubes. *Phys. Rev. Lett.*, 86:3160, 2001.

C. Latta, A. Högele, Y. Zhao, A. N. Vamivakas, P. Maletinsky, M. Kroner, J. Dreiser, I. Carusotto, A. Badolato, D. Schuh, W. Wegscheider, M. Atature, and A. Imamoglu. Confluence of resonant laser excitation and bidirectional quantum-dot nuclear-spin polarization. *Nature Physics*, 5:758, 2009.

S. Laurent, B. Eble, O. Krebs, A. Lemaitre, B. Urbaszek, X. Marie, T. Amand, and P. Voisin. Electrical control of hole spin relaxation in charge tunable InAs/GaAs quantum dots. *Phys. Rev. Lett.*, 94:147401, 2005.

M. N. Leuenberger and D. Loss. Quantum computing in molecular magnets. *Nature*, 410:789, 2001.

Ren-Bao Liu, Wang Yao, and L. J. Sham. Control of electron spin decoherence caused by electron-nuclear spin dynamics in a quantum dot. *New J. Phys.*, 9:226, 2007.

D. Loss and D. P. DiVincenzo. Quantum computation with quantum dots. *Phys. Rev. A*, 57: 120, 1998.

P. Maletinsky, M. Kroner, and A. Imamoglu. Breakdown of the nuclear-spin-temperature approach in quantum-dot demagnetization experiments. *Nature Phys.*, 5:407, 2009.

X. Marie, T. Amand, P. Le Jeune, M. Paillard, P. Renucci, L. E. Golub, V. D. Dymnikov, and E. L. Ivchenko. Hole spin quantum beats in quantum-well structures. *Phys. Rev. B*, 60:5811, 1999.

N. Mason, M. J. Biercuk, and C. M. Marcus. Local gate control of a carbon nanotube double quantum dot. *Science*, 303:655, 2004.

I. A. Merkulov, Al. L. Efros, and M. Rosen. Electron spin relaxation by nuclei in semiconductor quantum dots. *Phys. Rev. B*, 65:205309, 2002.

C. Meyer, J. M. Elzerman, and L. P. Kouwenhoven. Photon-assisted tunneling in a carbon nanotube quantum dot. *Nano Lett.*, 7:295, 2007.

W. B. Mims. Envelope modulation in spin-echo experiments. *Phys. Rev. B*, 5:2409, 1972.

E. D. Minot, Yuval Yaish, Vera Sazonova, and Paul L. McEuen. Determination of electron orbital magnetic moments in carbon nanotubes. *Nature*, 428:536, 2004.

E. Onac, F. Balestro, B. Trauzettel, C. F. J. Lodewijk, and L. P. Kouwenhoven. Shot-noise detection in a carbon nanotube quantum dot. *Phys. Rev. Lett.*, 96:026803, 2006.

K. Ono and S. Tarucha. Nuclear-spin-induced oscillatory current in spin-blockaded quantum dots. *Phys. Rev. Lett.*, 92:256803, 2004.

D. Paget, G. Lampel, B. Sapoval, and V. I. Safarov. Low field electron-nuclear spin coupling in gallium arsenide under optical pumping conditions. *Phys. Rev. B*, 15:5780, 1977.

A. Pályi and G. Burkard. Hyperfine-induced valley mixing and the spin-valley blockade in carbon-based quantum dots. *arXiv:0908.1054*, 2009.

C. H. Pennington and V. A. Stenger. Nuclear magnetic resonance of $C_{60}$ and fulleride superconductors. *Rev. Mod. Phys.*, 68:855, 1996.

J. R. Petta, A. C. Johnson, J. M. Taylor, E. A. Laird, A. Yacoby, M. D. Lukin, C. M. Marcus, M. P. Hanson, and A. C. Gossard. Coherent manipulation of coupled electron spins in semiconductor quantum dots. *Science*, 309:2180–2184, 2005.

L. A. Ponomarenko, F. Schedin, M. I. Katsnelson, R. Yang, E. W. Hill, K. S. Novoselov, and A. K. Geim. Chaotic Dirac billiard in graphene quantum dots. *Science*, 320:356, 2008.

C. Ramanathan. Dynamic nuclear polarization and spin diffusion in nonconducting solids. *Appl. Magn. Reson.*, 34:409, 2008.

G. Ramon and X. Hu. Dynamical nuclear spin polarization and the Zamboni effect in gated double quantum dots. *Phys. Rev. B*, 75:161301, 2007.

A. J. Ramsay, S. J. Boyle, R. S. Kolodka, J. B. B. Oliveira, J. Skiba-Szymanska, H. Y. Liu, M. Hopkinson, A. M. Fox, and M. S. Skolnick. Fast optical preparation, control, and readout of a single quantum dot spin. *Phys. Rev. Lett.*, 100:197401, 2008.

D. J. Reilly, J. M. Taylor, J. R. Petta, C. M. Marcus, M. P. Hanson, and A. C. Gossard. Suppressing spin qubit dephasing by nuclear state preparation. *Science*, 321:817, 2008.

L. G. Rowan, E. L. Hahn, and W. B. Mims. Electron-spin-echo envelope modulation. *Phys. Rev.*, 137:A61, 1965.

R. Saito, G. Dresselhaus, and M. S. Dresselhaus. *Physical Properties of Carbon Nanotubes*. Imperial College Press, London, 1998.

S. Sapmaz, C. Meyer, P. Beliczynski, P. Jarillo-Herrero, and L. P. Kouwenhoven. Excited state spectroscopy in carbon nanotube double quantum dots. *Nano Lett.*, 6:1350, 2006.

J. Schliemann, A. V. Khaetskii, and D. Loss. Spin decay and quantum parallelism. *Phys. Rev. B*, 66:245303, 2002.

J. Schliemann, A. V. Khaetskii, and D. Loss. Electron spin dynamics in quantum dots and related nanostructures due to hyperfine interaction with nuclei. *Journal of Physics: Condensed Matter*, 15:R1809, 2003.

M. J. Schmidt. private communication. 2009.

S. Schnez, F. Molitor, C. Stampfer, J. Guettinger, I. Shorubalko, T. Ihn, and K. Ensslin. Quantum confinement in graphene quantum dots. *Appl. Phys. Lett.*, 94:012107, 2009.

Y. G. Semenov, K. W. Kim, and G. J. Iafrate. Electron spin relaxation in semiconducting carbon nanotubes: The role of hyperfine interaction. *Phys. Rev. B*, 75:045429, 2007.

Y. A. Serebrennikov. The quadrupole mechanism of hole spin relaxation. *Phys. Lett. A*, 372: 3307, 2008.

A. Shabaev, Al. L. Efros, D. Gammon, and I. A. Merkulov. Optical readout and initialization of an electron spin in a single quantum dot. *Phys. Rev. B*, 68:201305, 2003.

P. W. Shor. Polynomial-time algorithms for prime factorization and discrete logarithms on a quantum computer. *SIAM Journal on Computing*, 26:1484–1509, 1997.

G. A. Steele, G. Gotz, and L. P. Kouwenhoven. Tunable few-electron double quantum dots and Klein tunnelling in ultraclean carbon nanotubes. *Nature Nanotechnology*, 4:363, 2009.

D. Stepanenko, G. Burkard, G. Giedke, and A. Imamoglu. Enhancement of electron spin coherence by optical preparation of nuclear spins. *Phys. Rev. Lett.*, 96:136401, 2006.

A. M. Stoneham. *Theory of Defects in Solids*. Oxford University Press, 1972. Chapter 13.

M. Syperek, D. R. Yakovlev, A. Greilich, J. Misiewicz, M. Bayer, D. Reuter, and A. D. Wieck. Spin coherence of holes in GaAs/(Al,Ga)As quantum wells. *Phys. Rev. Lett.*, 99:187401, 2007.

S. J. Tans, M. H. Devoret, H. Dai, A. Thess, R. E. Smalley, L. J. Geerligs, and C. Dekker. Individual single-wall carbon nanotubes as quantum wires. *Nature*, 386:474, 1997.

B. M. Terhal and G. Burkard. Fault-tolerant quantum computation for local non-Markovian noise. *Phys. Rev. A*, 71:012336, 2005.

B. Trauzettel and D. Loss. Carbon surprises again. *Nature Physics*, 5:317, 2009.

B. Trauzettel, D. V. Bulaev, D. Loss, and G. Burkard. Spin qubits in graphene quantum dots. *Nature Physics*, 3:192, 2007.

I. T. Vink, K. C. Nowack, F. H. L. Koppens, J. Danon, Y. V. Nazarov, and L. M. K. Vandersypen. Locking electron spins into magnetic resonance by electron-nuclear feedback. *Nature Physics*, 5:764, 2009.

R. Vrijen, E. Yablonovitch, K. Wang, H. W. Jiang, A. Balandin, V. Roychowdhury, T. Mor, and D. Divincenzo. Electron-spin-resonance transistors for quantum computing in silicon-germanium heterostructures. *Phys. Rev. A*, 62:012306, 2000.

I. Vurgaftman, J. R. Meyer, and L. R. Ram-Mohan. Band parameters for III–V compound semiconductors and their alloys. *J. Appl. Phys.*, 89:5815–5875, 2001.

R. Winkler. *Spin-Orbit Coupling Effects in Two-Dimensional Electron and Hole Systems*, volume 191 of *Springer Tracts in Modern Physics*. Springer-Verlag, Berlin, 2003.

W. M. Witzel and S. Das Sarma. Multiple-pulse coherence enhancement of solid state spin qubits. *Phys. Rev. Lett.*, 98:77601, 2007.

W. M. Witzel and S. Das Sarma. Quantum theory for electron spin decoherence induced by nuclear spin dynamics in semiconductor quantum computer architectures: Spectral diffusion of localized electron spins in the nuclear solid-state environment. *Phys. Rev. B*, 74:035322, 2006.

W. M. Witzel, Xuedong Hu, and S. Das Sarma. Decoherence induced by anisotropic hyperfine interaction in Si spin qubits. *Phys. Rev. B*, 76:035212, 2007.

L. M. Woods, T. L. Reinecke, and R. Kotlyar. Hole spin relaxation in quantum dots. *Phys. Rev. B*, 69:125330, 2004.

X. Xu, W. Yao, B. Sun, D. G. Steel, A. S. Bracker, D. Gammon, and L. J. Sham. Optically controlled locking of the nuclear field via coherent dark-state spectroscopy. *Nature*, 459: 1105, 2009.

Y. Yafet. Hyperfine interaction due to orbital magnetic moment of electrons with large g factors. *J. Phys. Chem. Solids*, 21:99, 1961.

W. Yao, R.-B. Liu, and L. J. Sham. Theory of electron spin decoherence by interacting nuclear spins in a quantum dot. *Phys. Rev. B*, 74:195301, 2006.

W. Yao, R. B. Liu, and L. J. Sham. Restoring coherence lost to a slow interacting mesoscopic spin bath. *Phys. Rev. Lett.*, 98:77602, 2007.

O. V. Yazyev. Hyperfine interactions in graphene and related carbon nanostructures. *Nano Lett.*, 8:1011, 2008.

O. V. Yazyev and L. Helm. Isotropic Knight shift of metallic carbon nanotubes. *Phys. Rev. B*, 72:245416, 2005.

P. Y. Yu and M. Cardona. *Fundamentals of Semiconductors*. Springer-Verlag Berlin Heidelberg, 2005. Section 2.6.

G. Yusa, K. Muraki, K. Takashina, K. Hashimoto, and Y. Hirayama. Controlled multiple quantum coherences of nuclear spins in a nanometre-scale device. *Nature*, 434:1001, 2005.

E. A. Yuzbashyan, B. L. Altshuler, V. B. Kuznetsov, and V. Z. Enolskii. Solution for the dynamics of the BCS and central spin problems. *J. Phys. A: Math. Gen.*, 38:7831, 2005.